Review

International Journal of Modern Physics A
Vol. 29, No. 24 (2014) 1430044 (120 pages)

DOI: 10.1142/S0217751X14300440

World Scientific
www.worldscientific.com

Performance of the ALICE experiment at the CERN LHC

The ALICE Collaboration*

Received 26 June 2014
Accepted 3 July 2014
Published 29 September 2014

ALICE is the heavy-ion experiment at the CERN Large Hadron Collider. The experiment continuously took data during the first physics campaign of the machine from fall 2009 until early 2013, using proton and lead-ion beams. In this paper we describe the running environment and the data handling procedures, and discuss the performance of the ALICE detectors and analysis methods for various physics observables.

Keywords: LHC; ALICE; heavy-ion collisions; particle detectors.

PACS numbers: 25.75.−q, 29.40.−n, 29.85.−c, 07.05.−t

Contents

1. ALICE Apparatus . . . 3
2. Beam Conditions . . . 7
   2.1. Beam parameters . . . 7
   2.2. Machine induced background . . . 8
      2.2.1. Background sources . . . 8
      2.2.2. Background rejection in ALICE . . . 12
   2.3. Luminosity determination . . . 14
      2.3.1. Introduction . . . 14
      2.3.2. van der Meer scanning technique . . . 15
      2.3.3. van der Meer scan analysis and results . . . 15
      2.3.4. Application of the vdM scan results in luminosity and cross-section measurements . . . 18
3. Data Taking . . . 19
   3.1. Running periods . . . 19
   3.2. Trigger . . . 22
   3.3. Readout . . . 25
   3.4. Online data compression . . . 28

*See Appendix A.

4. Calibration Strategy . . . 28
4.1. Condition data and online calibration . . . 28
4.2. Offline calibration . . . 31
4.3. Detector alignment . . . 31
5. Event Characterization . . . 32
5.1. Centrality . . . 32
5.2. Event plane . . . 35
5.2.1. Event plane from elliptic flow . . . 37
5.2.2. Event plane from higher harmonics . . . 38
5.2.3. Event plane from spectator deflection . . . 38
6. Central Barrel Tracking . . . 39
6.1. Preliminary determination of the interaction vertex . . . 40
6.2. Track reconstruction . . . 40
6.3. Final determination of the interaction vertex . . . 46
6.4. Secondary vertices . . . 47
7. Hadron Identification . . . 51
7.1. Particle identification in the ITS . . . 52
7.2. Particle identification in the TPC . . . 53
7.3. Particle identification in TOF . . . 55
7.4. Particle identification in the HMPID . . . 58
7.5. Overview of separation powers and combined PID . . . 61
7.6. Particle identification using weak decay topology . . . 63
7.7. Particle identification in physics analysis . . . 64
7.7.1. ϕ meson . . . 64
7.7.2. D meson . . . 65
7.7.3. Light nuclei . . . 66
8. Electron Identification . . . 66
8.1. Electron identification in the EMCal . . . 67
8.2. Electron identification in the TRD . . . 69
8.3. Electron identification in physics analysis . . . 73
9. Photons . . . 76
9.1. Photon reconstruction with calorimeters . . . 76
9.1.1. Cluster finder in PHOS . . . 77
9.1.2. Cluster finder in EMCal . . . 77
9.1.3. Cluster parameters . . . 77
9.1.4. Photon identification in calorimeters . . . 78
9.2. Photon conversion method . . . 80
9.3. π^0 and η reconstruction . . . 81
10. Jets . . . 84
10.1. EMCal jet trigger . . . 86
10.2. Jets in pp collisions . . . 88
10.2.1. Undetected hadronic energy . . . 88
10.2.2. Charged particle energy deposition in EMCal . . . 89
10.2.3. Other corrections . . . 90
10.2.4. Jet structure . . . 91
10.2.5. Jet energy resolution . . . 92
10.3. Jets in heavy-ion collisions . . . 92
11. Muons . . . 96
11.1. Reconstruction efficiency . . . 97
11.2. Trigger efficiency . . . 98

11.3. Invariant-mass resolution 99
12. Conclusion and Outlook 103
Acknowledgments 105
Appendix A. The ALICE Collaboration 106
References 115

1. ALICE Apparatus

ALICE[1–3] (A Large Ion Collider Experiment) is a major experiment at the Large Hadron Collider (LHC), Geneva, which is optimized for the study of QCD matter created in high-energy collisions between lead nuclei. Analysis based on QCD (quantum chromodynamics) lead to a prediction of the existence of a state of deconfined quarks and gluons at energy densities above 1 GeV/fm^3. The transition to this state is accompanied by chiral symmetry restoration, in which the quarks assume their current masses. This state of matter occurred in the early universe after the electroweak phase transition, i.e. at the age of 10^{-12}–10^{-5} s (for a recent review see Ref. 4.) High-energy nuclear collisions allow such energy densities to be reached, albeit in a small volume and for a limited duration. Assessing the properties of the created matter requires a sound understanding of the underlying collision dynamics. For this, the heavy-ion (AA) collision studies in the new energy regime accessible at the LHC have to be complemented by proton–proton (*pp*) and proton–nucleus (pA) collision experiments. These control measurements, besides being interesting in themselves, are needed to separate the genuine QCD-matter signals from the cold-matter initial- and final-state effects. The physics goals of ALICE are described in detail in Refs. 1 and 2; the results obtained to date are accessible at Ref. 5.

The ALICE apparatus (Fig. 1) has overall dimensions of $16 \times 16 \times 26$ m^3 and a total weight of $\sim 10\,000$ t. It was designed to cope with the particle densities expected in central Pb–Pb collisions at the LHC. The experiment has a high detector granularity, a low transverse momentum threshold $p_{\mathrm{T}}^{\mathrm{min}} \approx 0.15$ GeV/c, and good particle identification capabilities up to 20 GeV/c. The seventeen ALICE detector systems, listed in Table 1, fall into three categories: central-barrel detectors, forward detectors, and the MUON spectrometer. In this section, a brief outline of their features is given. Specifications and a more detailed description can be found in Ref. 3.

The central-barrel detectors — Inner Tracking System (ITS), Time Projection Chamber (TPC), Transition Radiation Detector (TRD), Time Of Flight (TOF), Photon Spectrometer (PHOS), Electromagnetic Calorimeter (EMCal), and High Momentum Particle Identification Detector (HMPID) — are embedded in the L3 solenoid magnet which has $B = 0.5$ T. The first four cover the full azimuth, with a segmentation of 20°, at midrapidity ($|\eta| \lesssim 0.9$). The ITS and the TPC are the main charged-particle tracking detectors of ALICE. The ITS is composed of six tracking layers, two Silicon Pixel Detectors (SPD), two Silicon Drift Detectors (SDD), and two Silicon Strip Detectors (SSD). The TPC has a 90 m^3 drift volume filled with Ne–CO_2 and is divided into two parts by the central cathode, which is kept

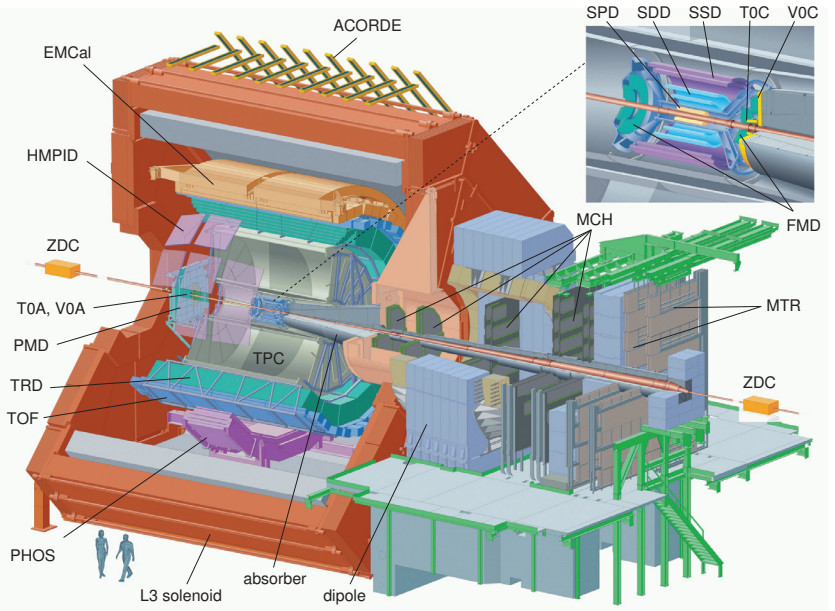

Fig. 1. The ALICE experiment at the CERN LHC. The central-barrel detectors (ITS, TPC, TRD, TOF, PHOS, EMCal, and HMPID) are embedded in a solenoid with magnetic field $B = 0.5$ T and address particle production at midrapidity. The cosmic-ray trigger detector ACORDE is positioned on top of the magnet. Forward detectors (PMD, FMD, V0, T0, and ZDC) are used for triggering, event characterization, and multiplicity studies. The MUON spectrometer covers $-4.0 < \eta < -2.5$, $\eta = -\ln\tan(\theta/2)$.

at -100 kV. The end plates are equipped with multiwire proportional chambers (MWPC). In addition to tracking, SDD and TPC provide charged-particle identification via measurement of the specific ionization energy loss $\mathrm{d}E/\mathrm{d}x$. The TRD detector consists of six layers of Xe–CO_2-filled MWPCs, with a fiber/foam radiator in front of each chamber. It is used for charged-particle tracking and for electron identification via transition radiation and $\mathrm{d}E/\mathrm{d}x$. The TOF detector, which is based on Multigap Resistive Plate Chamber (MRPC) technology, is used for particle identification at intermediate momenta. Finally, the cylindrical volume outside TOF is shared by two electromagnetic calorimeters with thicknesses of $\sim 20\ X_0$ (radiation lengths) and $\sim 1\ \lambda_{\mathrm{int}}$ (nuclear interaction length), the high-resolution PHOS and the large-acceptance EMCal, along with the ring-imaging Cherenkov detector HMPID, which has a liquid C_6F_{14} radiator and a CsI photo-cathode for charged-hadron identification at intermediate momenta.

The central barrel detectors have an 18-fold segmentation in azimuth. The ITS, TPC, and TOF cover the entire azimuthal range, which is of significant advantage for measurements of angular distributions and correlations. Modules of TRD, PHOS, and EMCal were successively added during the first years of running. The installation history of these detectors is given in Table 2.

Table 1. The ALICE detectors. The transverse (for HMPID, radial) and longitudinal coordinates r, z are measured with respect to the ALICE interaction point (IP2). The z axis points along the anticlockwise LHC beam. The detectors marked with an asterisk (*) are used for triggering. As of 2013, 13/18 of the TRD modules and 3/5 of the PHOS modules have been installed. The ZDCs were moved from $|z| \approx 114.0$ m to $|z| \approx 112.5$ m during the winter shutdown 2011/2012. The η and ϕ ranges specified for the proton ZDC are purely geometrical and do not take into account how charged particles are transported through the magnetic elements of the beam line.

	Acceptance				
Detector	Polar	Azimuthal	Position	Technology	Main purpose
SPD*	$\|\eta\| < 2.0$	full	$r = 3.9$ cm	Si pixel	tracking, vertex
	$\|\eta\| < 1.4$	full	$r = 7.6$ cm	Si pixel	tracking, vertex
SDD	$\|\eta\| < 0.9$	full	$r = 15.0$ cm	Si drift	tracking, PID
	$\|\eta\| < 0.9$	full	$r = 23.9$ cm	Si drift	tracking, PID
SSD	$\|\eta\| < 1.0$	full	$r = 38$ cm	Si strip	tracking, PID
	$\|\eta\| < 1.0$	full	$r = 43$ cm	Si strip	tracking, PID
TPC	$\|\eta\| < 0.9$	full	$85 < r/\text{cm} < 247$	Ne drift+MWPC	tracking, PID
TRD*	$\|\eta\| < 0.8$	full	$290 < r/\text{cm} < 368$	TR+Xe drift+MWPC	tracking, $e^{\pm}$ id
TOF*	$\|\eta\| < 0.9$	full	$370 < r/\text{cm} < 399$	MRPC	PID
PHOS*	$\|\eta\| < 0.12$	$220^\circ < \phi < 320^\circ$	$460 < r/\text{cm} < 478$	$PbWO_4$	photons
EMCal*	$\|\eta\| < 0.7$	$80^\circ < \phi < 187^\circ$	$430 < r/\text{cm} < 455$	Pb+scint.	photons and jets
HMPID	$\|\eta\| < 0.6$	$1^\circ < \phi < 59^\circ$	$r = 490$ cm	C_6F_{14} RICH+MWPC	PID
ACORDE*	$\|\eta\| < 1.3$	$30^\circ < \phi < 150^\circ$	$r = 850$ cm	scint.	cosmics
PMD	$2.3 < \eta < 3.9$	full	$z = 367$ cm	Pb+PC	photons
FMD	$3.6 < \eta < 5.0$	full	$z = 320$ cm	Si strip	charged particles
	$1.7 < \eta < 3.7$	full	$z = 80$ cm	Si strip	charged particles
	$-3.4 < \eta < -1.7$	full	$z = -70$ cm	Si strip	charged particles
V0*	$2.8 < \eta < 5.1$	full	$z = 329$ cm	scint.	charged particles
	$-3.7 < \eta < -1.7$	full	$z = -88$ cm	scint.	charged particles
T0*	$4.6 < \eta < 4.9$	full	$z = 370$ cm	quartz	time, vertex
	$-3.3 < \eta < -3.0$	full	$z = -70$ cm	quartz	time, vertex
ZDC*	$\|\eta\| > 8.8$	full	$z = \pm 113$ m	W+quartz	forward neutrons
	$6.5 < \|\eta\| < 7.5$	$\|\phi\| < 10^\circ$	$z = \pm 113$ m	brass+quartz	forward protons
	$4.8 < \eta < 5.7$	$\|2\phi\| < 32^\circ$	$z = 7.3$ m	Pb+quartz	photons
MCH	$-4.0 < \eta < -2.5$	full	$-14.2 < z/\text{m} < -5.4$	MWPC	muon tracking
MTR*	$-4.0 < \eta < -2.5$	full	$-17.1 < z/\text{m} < -16.1$	RPC	muon trigger

Table 2. Number of sectors (20° in azimuth each) of the central barrel covered by TRD, PHOS, and EMCal in the first years of ALICE running.

	TRD $\lvert\eta\rvert < 0.8$	PHOS $\lvert\eta\rvert < 0.12$	EMCal $\lvert\eta\rvert < 0.7$
2008	4	1	0
2009	7	3	2
2010	7	3	2
2011	10	3	5
2012	13	3	$5\frac{1}{3}$
2013	13	3	$5\frac{1}{3}$
goal	18	5	$5\frac{1}{3}$

The ALICE forward detectors include the preshower/gas-counter Photon Multiplicity Detector (PMD) and the silicon Forward Multiplicity Detector (FMD), which are dedicated to the measurement of photons and charged particles around $|\eta| \approx 3$, respectively. The quartz Cherenkov detector T0 delivers the time and the longitudinal position of the interaction. The plastic scintillator detector V0[a] measures charged particles at $-3.7 < \eta < -1.7$ and $2.8 < \eta < 5.1$, and is mainly used for triggering and for the determination of centrality and event plane angle in Pb–Pb collisions.[6] The centrality can also be measured with the Zero Degree Calorimeter (ZDC). The ZDC consists of two tungsten-quartz neutron (ZN) and two brass-quartz proton (ZP) calorimeters, placed symmetrically on both sides of the Interaction Point and used to count spectator nucleons. The ambiguity between the most central (few spectator nucleons) and the most peripheral (spectator nucleons bound in nuclear fragments) collisions is resolved by using an electromagnetic calorimeter (ZEM), which consists of two modules placed symmetrically on both sides of the beam pipe at $4.8 < \eta < 5.7$.

The MUON spectrometer, with a hadron absorber of $\sim 10\ \lambda_{\rm int}$, a dipole magnet of 3 Tm, and five tracking stations with two pad chambers each (Muon Chambers, MCH), is used to measure quarkonium and light vector meson production in a region of $-4.0 < y < -2.5$. The measurement of high-$p_{\rm T}$ muons, which predominantly come from the decay of charm and beauty, also falls within the scope of the spectrometer. Single-muon and muon-pair triggers with an adjustable transverse-momentum threshold are provided by two further stations (Muon Trigger, MTR) placed behind an additional $7\lambda_{\rm int}$ absorber.

The physics goals and a detailed description of the detectors and their expected performance can be found in Refs. 1–3. In this paper we report the actual performance achieved in the LHC data taking campaign 2009–2013 (LHC Run 1). The

[a]In ALICE physics papers an alternative notation, VZERO, is used to avoid conflict with V^0, the neutral particle decaying into two charged tracks (see Subsec. 6.4). In this article we follow the original notation from Refs. 1–3.

collision systems and energies inspected by ALICE are summarized in Table 6 in Sec. 3. In the following, we start from a description of the running conditions, data taking and calibration, and then review the performance of the experiment in terms of various physics observables.

The ALICE Coordinate System, used in Table 1 and throughout the paper, is a right-handed orthogonal Cartesian system defined as follows.[7] The origin is at the LHC Interaction Point 2 (IP2). The z axis is parallel to the mean beam direction at IP2 and points along the LHC Beam 2 (i.e. LHC anticlockwise). The x axis is horizontal and points approximately towards the center of the LHC. The y axis, consequently, is approximately vertical and points upwards.

2. Beam Conditions

2.1. *Beam parameters*

ALICE is situated at the interaction point IP2 of the LHC, close to the Beam 1 Transfer Line TI 2 injection region. The ALICE design, optimized for nuclear collisions,[2] requires a reduced luminosity in pp interactions at IP2. After three years of operation at the LHC, experience has shown that the maximum pp interaction rate at which all ALICE detectors can be safely operated is around 700 kHz (including the contribution of both beam–beam and beam–gas collisions). Typical target luminosity values for the ALICE pp data taking range from $\mathcal{L} \simeq 10^{29}$ s^{-1}cm^{-2} (during minimum bias data taking) to $\mathcal{L} \simeq 10^{31}$ s^{-1}cm^{-2} (when accumulating rare triggers). The average number of interactions per bunch crossing (μ) varies from 0.05 to 0.3.

During LHC Run 1, the instantaneous luminosity delivered to ALICE in pp collisions was adjusted by the machine to the required level by optimizing the following parameters: number of interacting bunches; value of the amplitude function at the interaction point[b] β^* and crossing angles; and separation of colliding beams (in the plane orthogonal to the crossing plane). Typically, the beams had to be separated at IP2 by 1.5–3.5 times the RMS of the transverse beam profile, depending on the values of β^*, bunch intensity, and emittance. In 2012, the machine was operated at the highest beam intensities so far (up to $\simeq 2 \times 10^{14}$ protons/beam). In order to ensure the necessary levelling of $\mathcal{L}$ and μ at IP2, a "main–satellite" bunch collision scheme was adopted: ALICE took data by triggering on the encounters of the main bunches of one beam with the satellite bunches of the other beam, sitting 10 RF buckets (25 ns) away from the nearest main bunch. The intensity of the satellite bunches is typically 0.1% of that of the main bunches ($\sim 1.6 \times 10^{11}$ p), therefore the luminosity per colliding bunch pair was reduced by the same factor. The very low μ was balanced by the large (> 2000) number of main–satellite encounters per LHC

[b]In accelerator physics, the amplitude function $\beta(z)$ describes the single-particle motion and determines the variation of the beam envelope as a function of the coordinate along the beam orbit, z (see e.g. Ref. 8). The parameter β^* denotes the value of $\beta(z)$ at the interaction point.

orbit, thus allowing the required $\mathcal{L}$ to be achieved with collisions quite uniformly distributed along the LHC orbit, with low pileup.

The rate of Pb–Pb collisions in 2010 and 2011 was well below the ALICE limits and ALICE was able to take data at the highest achievable luminosity, on the order of 10^{25} s^{-1}cm^{-2} in 2010 and 10^{26} s^{-1}cm^{-2} in 2011, with the corresponding hadronic μ being on the order of 10^{-5}–10^{-4} and 10^{-4}–10^{-3}, respectively. The maximum manageable interaction rate for p–Pb collisions was 200 kHz, roughly corresponding to a luminosity of 1×10^{29} s^{-1}cm^{-2}, only slightly below the LHC peak luminosity in 2013. The hadronic interaction probability in such conditions is about 0.06.

The β^* parameter at IP2 was 3.5 m for most of 2010, including the Pb–Pb run. In 2011 it was 10 m for the pp runs and 1 m for the Pb–Pb run. Finally, a value of 3 m was used in 2012, and it was reduced to 0.8 m for the p–Pb run at the beginning of 2013. The corresponding beam RMS widths for typical emittance values range from 15 to 150 μm. The longitudinal size of the luminous region depends mainly on the bunch length. Its typical RMS value is about 6 cm. The size of the luminous region was determined from ALICE data, via the distribution of interaction vertices (see Sec. 6) and was monitored online.

Due to the muon spectrometer dipole magnet and its respective compensator magnet, there is an intrinsic (internal) vertical crossing angle at IP2, which varies with the energy per nucleon (E), charge (Z), and mass number (A) of the beam particles as

$$\alpha_{\text{int}} = \frac{Z}{A}\,\frac{E_0}{E}\,\alpha_0\,, \tag{1}$$

with $E_0 = 3.5$ TeV/nucleon and $\alpha_0 = 280$ μrad. In addition, an external vertical crossing angle α_{ext} can be applied by means of a suitable magnet current setup dependent on E and β^* in order to control long range beam–beam effects and to prevent parasitic collisions in the vicinity of the IP. During Pb–Pb runs the external crossing angle is combined with the internal crossing angle in a way that minimizes the net crossing angle, in order to prevent acceptance losses in the ZDCs due to shadowing of the spectator neutron spot by the LHC tertiary collimators.[9]

The main beam parameters at IP2 during Run 1 are summarized in Table 3.

2.2. *Machine induced background*

2.2.1. *Background sources*

The operation and performance of detectors at the LHC can be affected by machine-induced background (MIB), a particle flux originating from the beams interacting with matter in the machine. This background scales with beam intensity and depends mainly on the residual gas pressure in the beam pipe and on the cleaning efficiency of collimator systems. The most relevant component of beam background at IP2 is produced close to the experimental region by inelastic beam–gas (BG)

Table 3. Summary of beam parameters for ALICE during the first four years of LHC operation.

Year	Mode	$\sqrt{s_{\mathrm{NN}}}$ (TeV)	β^* (m)	α_{int} (μrad)	α_{ext} (μrad)	Colliding bunches
2009	pp	0.9	10	2180	0	≤ 2
2009	pp	2.36	10	830	0	≤ 2
2010	pp	7	2; 3.5	280	0; 220	≤ 16
2010	Pb–Pb	2.76	3.5	280	-280	≤ 130
2011	pp	2.76	10	710	0	≤ 64
2011	pp	7	10	280	160	≤ 39
2011	Pb–Pb	2.76	1	280	-160	≤ 336
2012	pp	8	3	245 (-245)	-180 ($+290$)	0 (main–main); ≤ 2500 (main–sat.)
2012	p–Pb	5.02	10	-245	-290	≤ 8
2013	p–Pb	5.02	0.8	-245	125	≤ 338
2013	pp	2.76	10	710	170	≤ 36

interactions in the first 40 m of the so-called Long Straight Section 2 (LSS2), 270 m on either side of IP2.

Given the requirement of a reduced luminosity, in pp running the background rate in ALICE can be of the same order of magnitude as the interaction rate. Since ALICE has been designed to perform tracking for up to 1000 times the pp multiplicity, the tracking performance is not affected by such a background level. However, MIB affects the operation of gaseous detectors, leading to HV trips due to large charge deposits. Such trips were observed during the highest-intensity pp running periods in 2011 and 2012 and concerned mainly the TPC and MCH detectors. Furthermore, MIB can cause cumulative radiation damage from high integral doses and neutron fluence,[10] thus accelerating the ageing of detectors. For these reasons, in the high beam intensity pp running ALICE was switching on its detectors only after the background interaction rate dropped to an acceptable level (up to several hours after the beginning of the fill).

Large background from BG interactions was observed in 2011 and 2012 during the pp runs, increasing faster than linearly with the number of circulating bunches and bunch intensity. Vacuum deterioration inside the beam pipe can be caused by synchrotron radiation-induced desorption, beam-induced RF heating, and electron cloud formation in various sections of the accelerator.[11–13] In particular, a large pressure increase was observed with circulating beams inside the TDI (beam absorber for injection protection) and the large recombination chamber located in LSS2.[14–16]

A detailed study has been performed to characterize the dependence of the observed background rate[c] on vacuum conditions and beam charge. A linear correlation was found between the background rate and the product of the beam

[c]The background from BG interactions is measured via the V0 detector timing information, as will be described in Subsec. 2.2.2.

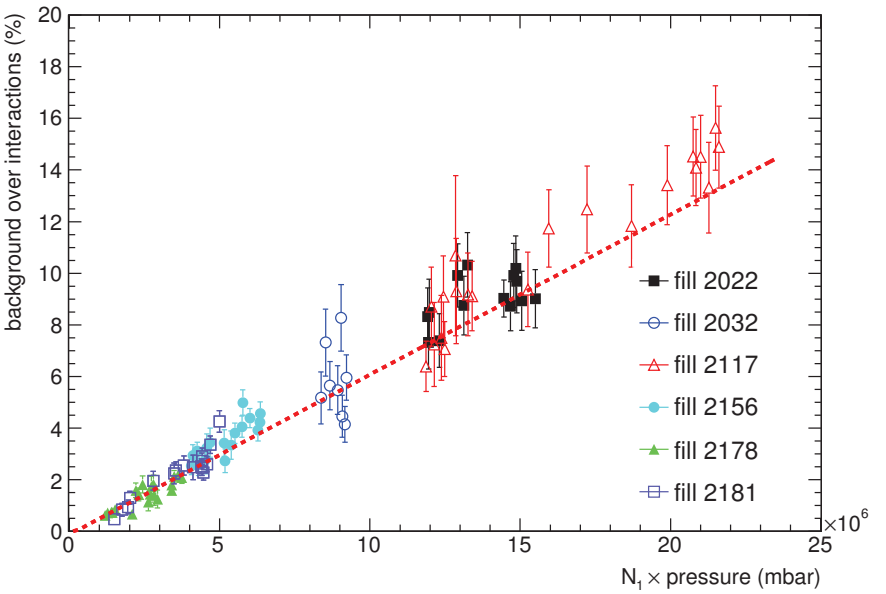

Fig. 2. Background rate observed during several fills as a function of the product of the intensity of Beam 1, N_1, and the sum of the measured pressures from three vacuum gauges on the left LSS2.

charge and the sum of the pressures measured by the vacuum gauges along the LSS2, on both sides of IP2 (Fig. 2). Figure 3 shows a comparison between the measured background rate for a given LHC fill[d] and that estimated using the linear dependence described in Fig. 2, confirming the validity of the model.

The residual gas pressure is always nominal in the Pb–Pb physics mode, since the total beam charge is about two orders of magnitude smaller than in pp. Thus, all processes which degrade the vacuum in the proton physics mode, in particular TDI heating and electron cloud formation, are suppressed. Minimum bias and centrality triggers are not affected by any beam background; however, some of the trigger inputs, such as the ZDC and muon triggers, showed large rate fluctuations (Fig. 4). A detailed analysis of all fills has shown that the observed fluctuations are always correlated with Beam 1 losses on the tertiary collimator (TCTH) located a few meters upstream of one of the ZDCs (ZDC-A). A clear correlation was observed between the ZDC-A trigger rate (which is sensitive to both beam–beam and beam–gas collisions) and the losses recorded by Beam 1 BLM (Beam Loss Monitor) located on the TCTH. Generally, an increase towards the end of the fill has been observed, which could be explained by a degradation of the beam quality and interactions with the collimation system.

[d]A fill is a period during which beams are circulating in the LHC: it starts with the injection and ends with the beam dump.

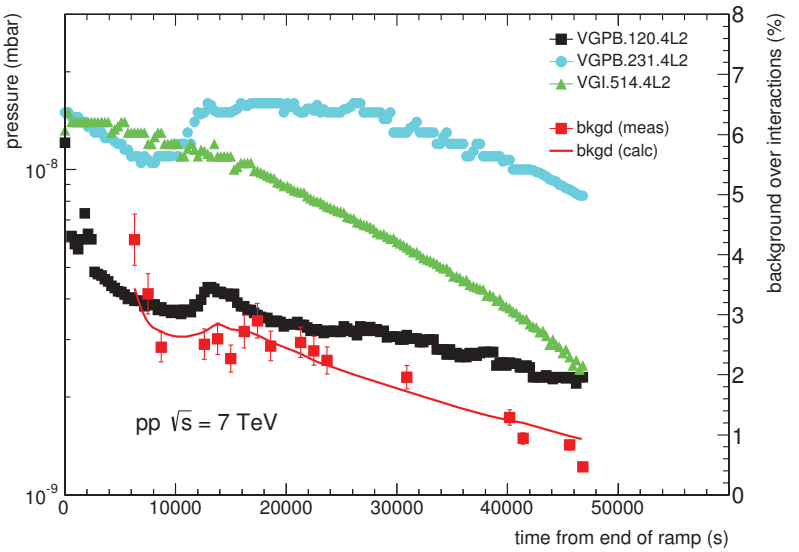

Fig. 3. Beam pipe pressure and background rate in fill 2181. The expected background rate has been estimated using the linear parametrization shown in Fig. 2. VGPB.120.4L2, VGPB.231.4L2, and VGI.514.4L2 are the pressure gauges located in front of the Inner triplet (at 69.7 m from IP2), on the TDI beam stopper (at 80 m from IP2), and on the large recombination chamber (at 109 m from IP2), respectively.

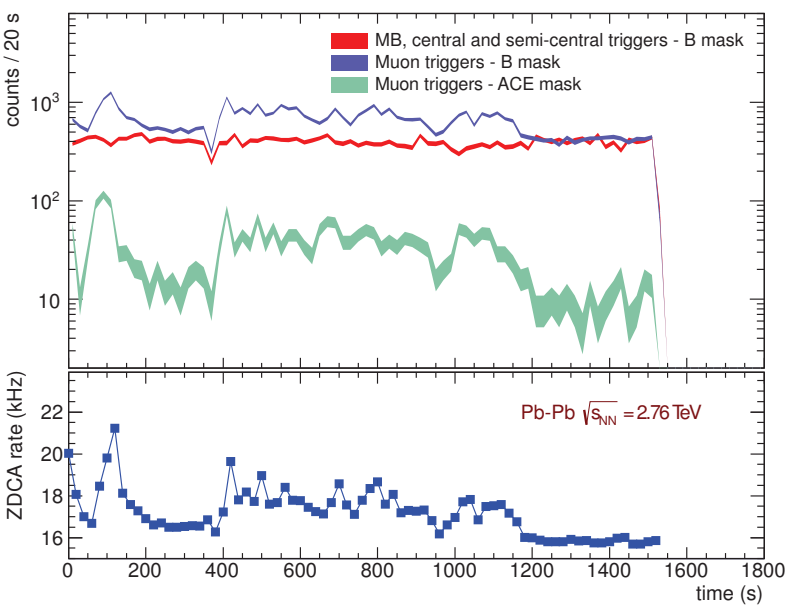

Fig. 4. Top: minimum bias, centrality, and muon triggers as a function of time during Pb–Pb data taking (run 169721). The B mask selects the LHC bunch slots where collisions between bunches of Beam 1 and Beam 2 are expected at IP2, while the ACE mask selects slots where no beam–beam collision is expected. Bottom: ZDC-A trigger rate as a function of time in the same run.

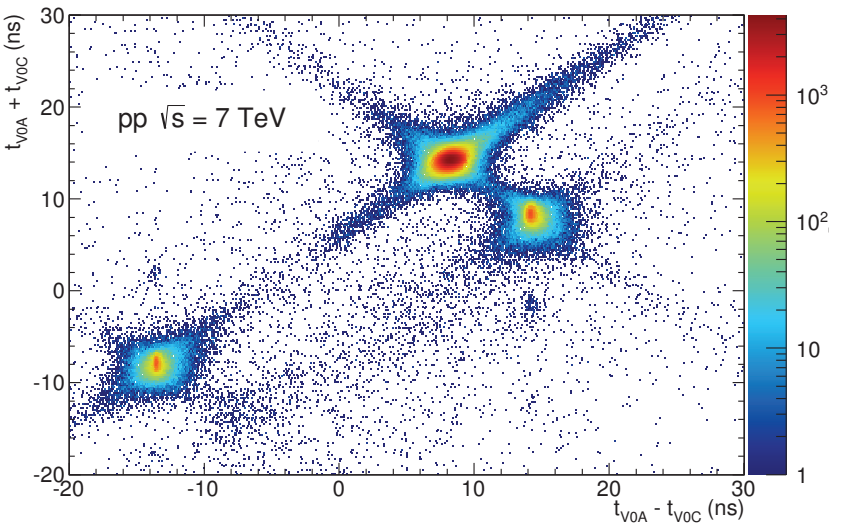

Fig. 5. Correlation between the sum and difference of signal times in V0A and V0C. Three classes of events — collisions at (8.3 ns, 14.3 ns), background from Beam 1 at (−14.3 ns, −8.3 ns), and background from Beam 2 at (14.3 ns, 8.3 ns) — can be clearly distinguished.

2.2.2. *Background rejection in ALICE*

Background estimation for pp running is performed with the V0 detector, a small-angle detector consisting of two circular arrays of 32 scintillator counters each, called V0A and V0C, which are installed on either side of the ALICE interaction point.[6] As described in Sec. 1, the V0A detector is located 329 cm from IP2 on the side opposite to the muon spectrometer, whereas V0C is fixed to the front face of the hadronic absorber, 88 cm from IP2. The signal arrival time in the two V0 modules is exploited in order to discriminate collision events from background events related to the passage of LHC Beam 1 or Beam 2. The background caused by one of the beams is produced upstream of the V0 on the side from which the beam arrives. It thus produces an "early" signal when compared with the time corresponding to a collision in the nominal interaction point. The difference between the expected beam and background signals is about 22.6 ns in the A side and 6 ns in the C side. As shown in Fig. 5, background events accumulate mainly in two peaks in the time sum-difference plane, well separated from the main (collision) peak. With the experience gained during the first years of data taking, in 2012 the V0 time gates used to set the trigger conditions on collision or background events have been refined and the MIB contamination has been reduced to $\sim 10\%$, depending on vacuum conditions and luminosity.

The collected events are further selected offline to validate the online trigger condition and to remove any residual contamination from MIB and satellite collisions. As a first step, the online trigger logic is validated using offline quantities. The V0 arrival time is computed using a weighted average of all detector elements.

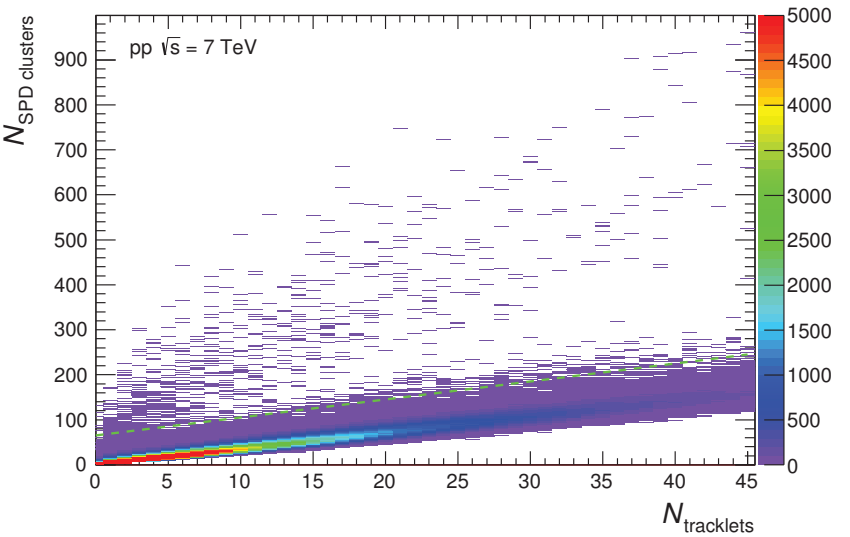

Fig. 6. (Color online) Correlation between reconstructed SPD clusters and tracklets. Two bands corresponding to the collisions and MIB are visible. The dashed cyan line represents the cut used in the offline selection: events lying in the region above the line are tagged as BG and rejected.

Then, MIB events are rejected using the timing information measured in the V0 complemented, in pp physics mode, by a cut on the correlation between clusters and tracklets reconstructed in the SPD. Background particles usually cross the pixel layers in a direction parallel to the beam axis. Therefore, only random combinations of BG hits can build a reconstructed track pointing to the vertex. Hence, one needs a large number of clusters to have a significant probability for this to happen (Fig. 6). This cut requires a large multiplicity in order to be effective and rejects a negligible number of events beyond those already rejected by the V0. Only a very small fraction of background events survive the above-mentioned cuts in Pb–Pb collisions. The overall contamination can be determined by an analysis of control data taken with only one of the beams crossing the ALICE interaction point and is found to be smaller than 0.02%. In pp collisions, the amount of background surviving the cuts is strongly dependent on the running conditions and on the specific trigger configuration under study. While the fraction of background events in the physics-selected minimum bias triggers amounts to about 0.3% in the data taken during the 2010 run, it can reach values above 10% at the beginning of a fill in the 2011 and 2012 runs. Whenever relevant for the normalization of the results, the residual background was subtracted in the physics analyses, based on the information obtained from the control triggers.

The parasitic collision of main bunches with satellite bunches located a few RF buckets away from a main bunch are also a source of background in the standard analyses. The background from main-satellite collisions is non-negligible in the Pb–Pb running mode where the satellite population is larger than in pp.

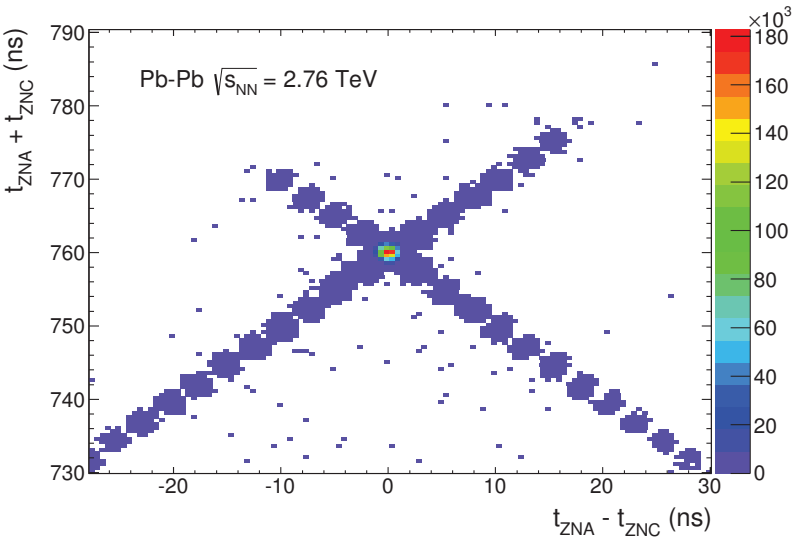

Fig. 7. Correlation between the sum and the difference of times recorded by the neutron ZDCs on either side (ZNA and ZNC) in Pb–Pb collisions. The large cluster in the middle corresponds to collisions between ions in the nominal RF bucket on both sides, while the small clusters along the diagonals (spaced by 2.5 ns in the time difference) correspond to collisions in which one of the ions is displaced by one or more RF buckets.

Main-satellite collisions occur at positions displaced by multiples of 2.5 ns/2 $\cdot$ c = 37.5 cm, with respect to the nominal interaction point. This is well outside the standard fiducial vertex region $|V_z| \lesssim 10$ cm. Satellite events are rejected using the correlation between the sum and the difference of times measured in the ZDC, as shown in Fig. 7.

2.3. *Luminosity determination*

2.3.1. *Introduction*

Cross-section measurements in pp collisions are essential for the ALICE physics program because particle production in nucleus–nucleus (A–A) collisions is often compared with the extrapolation from elementary pp collisions via binary nucleon–nucleon collision scaling (nuclear modification factor, R_{AA}). The precision of R_{AA} measurements needed to quantify the importance of nuclear effects is typically $\simeq 10\%$. Thus, a precision on the order of 5% or better on the pp cross section (including luminosity normalization) is desired.

Although it is not crucial for R_{AA},[e] the determination of the absolute luminosity in Pb–Pb collisions is needed for cross section studies in electromagnetic and ultraperipheral interactions.

[e]As is shown in Subsec. 5.1, a centrality-dependent normalization factor can be obtained via the Glauber model.

2.3.2. *van der Meer scanning technique*

The measurement of the cross section $\sigma_{\rm R}$ for a chosen reference process is a prerequisite for luminosity normalization. Reference (or visible) cross sections can be measured in van der Meer (vdM) scans,[17] where the two beams are moved across each other in the transverse direction. Measurement of the rate R of a given process as a function of the beam separation Δx, Δy allows one to determine the head-on luminosity $\mathcal{L}$ for a pair of colliding bunches with particle intensities N_1 and N_2 as:

$$\mathcal{L} = \frac{N_1 N_2 f_{\rm rev}}{h_x h_y}\,, \tag{2}$$

where $f_{\rm rev}$ is the accelerator revolution frequency and h_x and h_y are the effective beam widths in the x and y directions: they are measured as the area below the $R(\Delta x, 0)$ and $R(0, \Delta y)$ curve, respectively, when divided by the head-on rate $R(0, 0)$. Under the assumption that the beam profiles are Gaussian, the effective width can simply be obtained as the Gaussian standard deviation parameter (obtained from a fit to the curve) multiplied by $\sqrt{2\pi}$. However, the Gaussian assumption is not necessary for the validity of the method; thus, other functional forms can be used, as well as numerical integration of the curve. The cross section $\sigma_{\rm R}$ for the chosen reference process can be obtained as $\sigma_{\rm R} = R(0, 0)/\mathcal{L}$.

2.3.3. *van der Meer scan analysis and results*

In this section, results from five scans carried out at the LHC are summarized. Two scans were performed in 2010 for pp collisions at $\sqrt{s} = 7$ TeV. Another pp scan was done in 2011 at $\sqrt{s} = 2.76$ TeV. Furthermore, two Pb–Pb scans were performed at $\sqrt{s_{\rm NN}} = 2.76$ TeV in 2010 and 2011. More details on these measurements can be found in Ref. 18.

The conditions, results, and systematic uncertainties of the three pp scans are specified in Table 4. The chosen reference process (MBand) for all of these scans is the coincidence of hits in the V0 detectors on the A and C sides. The MBand rate was measured as a function of the beam separation (upper panels of Fig. 8). The scan areas were obtained via numerical integration. In the March 2011 scan, the cross section was measured separately for the 48 colliding bunch pairs (as shown in the bottom panel of Fig. 8) and then averaged. The resulting spread among different bunches is less than 0.5% (RMS). A set of corrections must be applied throughout the data analysis procedure, namely: pileup correction (up to 40%); length scale calibration, needed for a precise determination of the beam separation and performed by displacing the beams in the same direction and measuring the primary vertex displacement with the pixel detector (SPD); satellite (displaced) collisions of protons captured in non-nominal RF slots, detected via the arrival time difference in the two V0 arrays;[19] background from beam–gas interactions; and variation of the luminosity during the scan due to intensity losses and emittance

Table 4. Details of the colliding systems and measured MBand cross sections and uncertainties for the three pp vdM scans performed at the LHC IP2.

Scan	May 2010	October 2010	March 2011
$\sqrt{s}$ (TeV)	7	7	2.76
β^* (m)	2	3.5	10
Net crossing angle (μrad)	280	500	710
Colliding bunch pairs in ALICE	1	1	48
σ_{MBand} (mb)	54.2 ± 2.9	54.3 ± 1.9	47.7 ± 0.9
Uncertainties			
Bunch intensity	4.4%	3.2%	0.6%
Length scale	2.8%	1.4%	1.4%
Luminosity decay	1%	negligible	0.5%
V0 afterpulses	negligible	negligible	0.2%
Background subtraction	negligible	negligible	0.3%
Same fill reproducibility	negligible	0.4%	0.4%
x–y displacement coupling	negligible	negligible	0.6%
β^* variation during the scan	negligible	negligible	0.4%
Total	5.4%	3.5%	1.9%

growth. In October 2010, two scans were performed in the same fill, in order to check the reproducibility of the measurement. The two results agree within 0.4%: they have been averaged and the difference included in the systematic uncertainties. The beam intensity is measured separately for each circulating bunch by the LHC beam current transformers, and provided to the experiments after detailed analysis.[19–23] In the March 2011 scan, the uncertainty on the bunch intensity was much lower compared with the 2010 scans,[21,22] so certain additional sources of uncertainty were also investigated. These were: coupling between horizontal and vertical displacements; variation of β^* during the scan resulting from beam–beam effects; and afterpulses in the V0 photomultipliers arising from ionization of the residual gas inside the photomultiplier tube. For the 2010 scans, these additional sources are negligible when compared with the uncertainty on the beam current.

The ALICE luminosity determination in pp collisions has been compared with the other LHC experiments via the cross section for a candle process, defined as a pp interaction with at least one charged particle produced with $p_{\mathrm{T}} > 0.5$ GeV/c and $|\eta| < 0.8$. This was determined as $\sigma_{\mathrm{candle}} = f_{\mathrm{candle}}\, \sigma_{\mathrm{MBand}}$, where the scaling factor $f_{\mathrm{candle}} = (0.817 \pm 0.004)$ was determined from data with a small ($\simeq 3\%$) Monte Carlo efficiency correction. The obtained result (from the May 2010 scan) is $\sigma_{\mathrm{candle}} = 44.3 \pm 2.1$ mb, in good agreement with the ATLAS (42.3 ± 2.1 mb) and CMS (44.0 ± 2.0 mb) results.[24] The quoted uncertainties represent the statistical and systematic errors combined in quadrature; part of the uncertainty of the beam intensity determination, that is common to all experiments,[20] is not included.

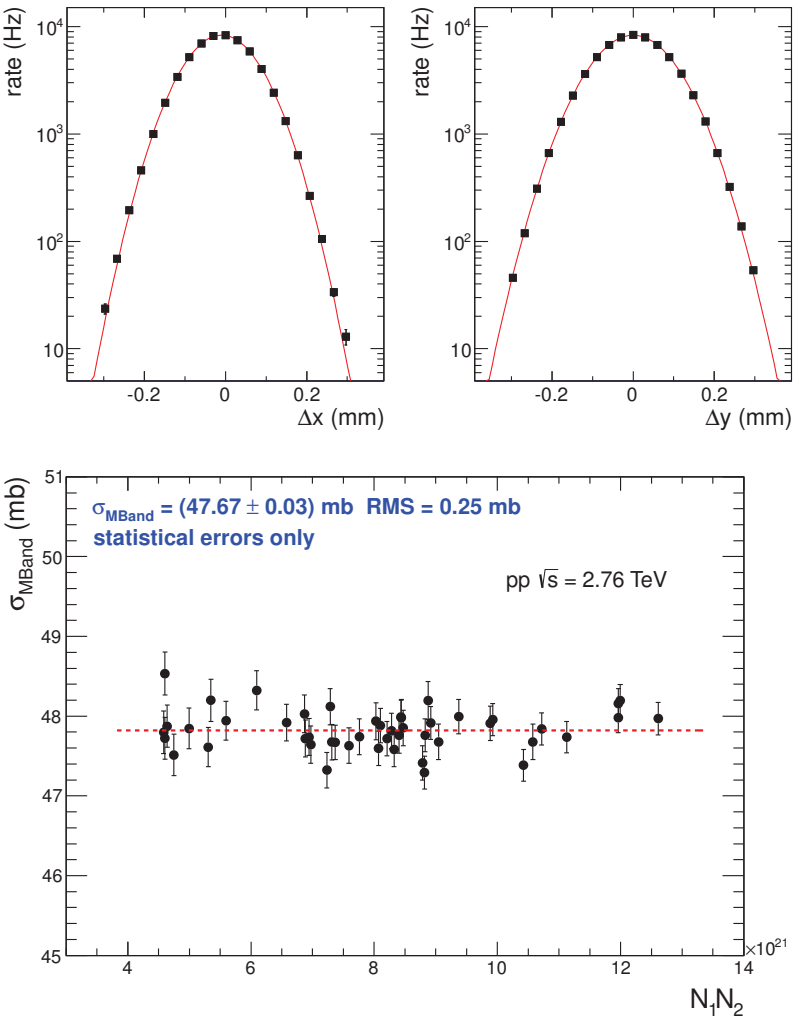

Fig. 8. Top: MBand trigger rate versus beam separation in x and y obtained during the May 2010 van der Meer scan. Double Gaussian fits to the data are shown as lines. Bottom: Measured MBand cross section for 48 colliding bunch pairs in the March 2011 scan, as a function of the product of colliding bunch intensities N_1N_2.

The main parameters for the two Pb–Pb scans are reported in Table 5. Given the low hadronic interaction rate in 2010, the scan was based on the detection of neutrons from electromagnetic Pb–Pb interactions by the ZDC.[25] The chosen reference process is the logical OR of hits in either of the two neutron calorimeters (ZNor). The scanned process in 2011 was a semicentral (SC) trigger based on the coincidence of V0A and V0C, with signal amplitude thresholds chosen in such a way that the trigger efficiency is 100% for events belonging to the 0–50% centrality percentile, and drops rapidly for more peripheral events.

Table 5. Details of the colliding systems and measured cross sections and uncertainties for two Pb–Pb vdM scans performed at the LHC IP2.

Scan	November 2010	December 2011
$\sqrt{s_{\rm NN}}$ (TeV)	2.76	2.76
β^* (m)	3.5	1
Crossing angle (μrad)	$\simeq 0$	120
Colliding bunch pairs in ALICE	114	324
$\sigma_{\rm ZNor}$ (b)	371^{+24}_{-19}	—
$\sigma_{\rm SC}$ (b)	—	$4.10^{+0.22}_{-0.13}$
Uncertainties		
Bunch intensity	$-3.0\% + 4.7\%$	$-1.6\% + 4.4\%$
Length scale	2.8%	1.4%
Luminosity decay	2%	2%
Unknown bunch-by-bunch profile	2%	—
Background subtraction	1%	1%
Scan-to-scan reproducibility	1%	1%
Total	$-5.2\% + 6.4\%$	$-3.1\% + 5.3\%$

The analysis technique is the same as described for the pp scans. Since the bunch-by-bunch measurement of the reference process rate was not available in 2010, the analysis of the November 2010 scan was performed for the "inclusive" rate, i.e. the sum of all bunch rates, thus measuring an "average" beam profile. The bias arising from this limitation was estimated in two ways: by simulation with realistic bunch intensities and emittances, and by computing the difference between the two methods for the 2011 scan. The second approach resulted in a larger discrepancy (2%), which was added to the systematic uncertainties.

The result and uncertainties for the Pb–Pb scans are reported in Table 5. The main source of uncertainty is the fraction of ghost charge in the measured beam current, consisting of ions circulating along the LHC rings outside of nominally filled bunch slots, which do not contribute to the luminosity.[23]

The analysis of the 2012 (pp) and 2013 (p–Pb) vdM scans is ongoing. For these scans, along with the MBand trigger, another luminosity signal is available, based on the T0 detector. The T0 provides a vertex trigger defined as the coincidence between T0A and T0C, with the additional requirement that the difference in their signal times corresponds to an interaction happening within 30 cm from IP2. The latter condition provides excellent rejection of beam-gas and satellite background. Indeed, a background contamination below 0.1% was obtained in p–Pb collisions at a luminosity of 10^{29} s^{-1}cm^{-2}.

2.3.4. *Application of the vdM scan results in luminosity and cross-section measurements*

The van der Meer scan results in pp collisions at $\sqrt{s} = 2.76$ and 7 TeV were used to measure the inelastic cross sections at the two energies.[26] A Monte Carlo simulation, tuned so as to reproduce the fractions of diffractive events observed

in data, was used to determine the efficiency of the MBand trigger for inelastic pp interactions. The MBand cross sections were then corrected for this efficiency, giving the result $\sigma_{\rm INEL} = 62.8 \pm 1.2\ ({\rm vdM})^{+2.4}_{-4.0}\ ({\rm MC})$ mb at $\sqrt{s} = 2.76$ TeV and $\sigma_{\rm INEL} = 73.2 \pm 2.6\ ({\rm vdM})^{+2.0}_{-4.6}\ ({\rm MC})$ mb at $\sqrt{s} = 7$ TeV.

In all the other ALICE analyses involving cross-section measurements,[f] the reference cross sections (MBand, ZNor, SC) measured in the van der Meer scans (Tables 4 and 5) were used for indirect determination of the integrated luminosity. In cases where the trigger condition used for the physics analysis coincided with the reference trigger (as was the case in Ref. 25), the luminosity was simply measured as the number of analyzed events divided by the trigger cross section. In all other cases, the number of triggered events was converted into an equivalent number of reference triggers via a scaling factor, computed either from data (as for example in Refs. 28 and 29) or via the ratio of the trigger rates, measured with scalers (as in Ref. 30). Depending on the analysis, this scaling procedure resulted in additional systematic uncertainties of up to 3%.

3. Data Taking

3.1. *Running periods*

ALICE took data for all the collision systems and energies offered by the LHC. The data taking started in fall 2009 with pp collisions at the LHC injection energy, $\sqrt{s} = 0.9$ TeV. In 2010, the proton beam energy was brought up to half of its nominal value, 3.5 TeV, and the luminosity was gradually increased. In this period the interaction rate was low (between a few kHz and a few tens of kHz) and ALICE mostly triggered on minimum bias (MBor[18,26]) interactions using V0 and SPD, single muon trigger (MSL), and high-multiplicity trigger (HM) (see Subsec. 3.2 for a description of the ALICE triggers). In the subsequent high-intensity pp and p–Pb running in 2011–2013, ALICE usually split its data-taking into minimum-bias (MB) and rare-trigger blocks, for which the interaction rate was reduced to $O(10)$ kHz and $O(100)$ kHz, respectively. Methods for reducing the luminosity are described in Sec. 2. The two limits correspond to the saturation of the readout with minimum-bias triggered events and to the maximum flux tolerated by the detectors, respectively. The two modes of operation are briefly discussed below.

For minimum bias runs, the pp and p–Pb interaction rates were on the level of 10 kHz, enough to reach 95% of the maximum detector readout rate while keeping the mean number of interactions per bunch crossing (μ) low, nominally below 0.05, in order to avoid significant same-bunch pileup.

In the rare-trigger running mode, the luminosity in pp and p–Pb was increased to 4–10 $\mu{\rm b}^{-1}{\rm s}^{-1}$ and 0.1 $\mu{\rm b}^{-1}{\rm s}^{-1}$, corresponding to inelastic interaction rates of 200–500 kHz and 200 kHz, respectively. The luminosity limits were determined by the stability of the TPC and muon chambers under the load caused by interactions

[f]With the exception of Ref. 27, where a theoretical reference cross section was used instead.

at IP2 and by background particles. During pp and p–Pb rare-trigger runs, the TPC event size increased by an order of magnitude due to pileup tracks within the drift time window of ~ 100 μs. The trigger dead time was kept at a level of 20–40% in order to inspect as much of the luminosity delivered by the LHC as possible.

The luminosity reduction in the pp running in 2012 was performed by colliding main bunches with satellite bunches (see Sec. 2). This resulted in a typical luminosity of ~ 7 $\mu b^{-1}s^{-1}$ (up to a maximum of 20 $\mu b^{-1}s^{-1}$) at the beginning of the fill and a rapid decay within the fill. Owing to this and to a background-interaction rate of the same order as the pp rate (see Sec. 2), ALICE only took data in the second part of each fill, starting in the rare-trigger mode with a subset of detectors, and only switching to minimum-bias mode when the luminosity dropped to about 1–4 $\mu b^{-1}s^{-1}$, a level tolerable for the V0 and the TPC. The downscaling factors for the MBand,[18,26] TJE, and SPI triggers were dynamically determined at the beginning of each run so as to keep the overall trigger live time at a level of 70–80% over the duration of the fill.

During the 2011 Pb–Pb running period, the interaction rate provided by the LHC reached 3–4 kHz. ALICE ran with the minimum bias, centrality, and rare triggers activated at the same time. With the multi-event buffering and with the minimum bias and centrality triggers downscaled, the effective trigger dead time was low (dead-time factor of 33%). The situation will be similar in the LHC Run 2 (2015–2017), for which the expected collision rate is $O(10)$ kHz, still low enough to avoid pileup.

Table 6 summarizes data taking with beams by ALICE together with the luminosity provided by the LHC, the obtained trigger statistics, and the recorded data volume. Whenever the luminosity was reduced for ALICE, its final value is quoted and marked with an asterisk. The beam duration and run duration are the integrated time with stable beams and the time during which ALICE was recording collision data, respectively. The difference between the two represents the time spent on starting/stopping of runs, the recovery time after detector trips, and, for pp runs in 2011 and 2012, the time spent waiting for the particle flux to drop to a level acceptable for the detectors. The run duration is not corrected for the trigger/acquisition dead time. The delivered luminosity is the luminosity integrated over the beam duration. The abbreviations denoting various triggers are explained in Subsec. 3.2. The recorded data volume slightly exceeds the read one because of the header data. The large differences between these two numbers, starting from pp in 2011, arise from the online compression discussed in Subsec. 3.4.

In the context of Table 6 one should note that many of the top ALICE physics goals involve measurements at low transverse momenta, where triggering cannot be used. This applies in particular to all measurements in the ALICE central barrel, where the vast majority of published papers are from minimum-bias data. Consequently, for the performance of ALICE the recorded statistics of minimum-bias events, where the data acquisition system runs with a significant dead time, is the main figure of merit. The evolution of the ALICE experiment towards Run 3

Table 6. ALICE data taking in Run 1 (2009–2013). See text for details.

Year	System, $\sqrt{s_{\rm NN}}$ (TeV)	Running mode	Peak $\mathcal{L}$ (μb^{-1}s^{-1})	Duration beam [run] (h)	Delivered $\mathcal{L}$	Recorded statistics (10^6 events)	Data read [recorded] (TB)
2009	pp 0.9	MB	5.2×10^{-4}	n.a. [26.8]	19.6 μb^{-1}	MBor: 0.5	0.41 [0.43]
	pp 2.36	MB	1.0×10^{-4}	n.a. [3.1]	0.87 μb^{-1}	MBor: 0.04	0.01 [0.01]
2010	pp 0.9	MB	1.5×10^{-2}	15.7 [13.0]	0.31 nb^{-1}	MBor: 8.5	5.74 [5.97]
	pp 7.0	MB+rare (mixed)	1.7*	847 [613]	0.5 pb^{-1}	MB: 825 HM: 26 MSL: 132	755 [773]
	Pb–Pb 2.76	MB	2.8×10^{-5}	223 [182]	9 μb^{-1}	MB: 56	810 [811]
2011	pp 2.76	rare	4.4×10^{-1}	35 [32]	46 nb^{-1}	MBor: 74 HM: 0.0015 E0: 0.78 MSL: 9.4	100 [101]
	pp 7.0	rare	9 (450 kHz)	1332 [841]	4.9 pb^{-1}	MBor: 608 MBand: 163 EJE: 27 EGA: 8 MUL: 7.6	1981 [1572]
	Pb–Pb 2.76	rare	4.6×10^{-4}	203 [159]	146 μb^{-1}	MBZ: 9 CENT: 29 SEMI: 34 MSH: 23 EJE: 11 CUP: 7.9 MUP: 3.4	3151 [908]
2012	pp 8	MB rare	0.2* (10 kHz) 20 (1 MHz)	1824 [1073]	9.7 pb^{-1} (altogether)	MBor: 38 MBand: 270 SPI: 63 MSH: 86 MUL: 12 EGA: 3.1 TJE: 21	3211 [1286]
	p–Pb 5.02	MB (pilot)	9×10^{-5} (180 Hz)	7.6 [6.6]	1.5 μb^{-1}	MBand: 2.43	5.0 [3.4]
2013	p–Pb 5.02	MB rare	5×10^{-3}* (10 kHz) 1×10^{-1} (200 kHz)	50.2 [46.8] 70.1 [50.0]	0.891 nb^{-1} 14.0 nb^{-1}	MBand: 134 ZED: 1.1 MSH: 10 MUL: 9.5 EGA: 1.3 TJE: 0.59 MUP: 0.76	406 [91] 472 [97]
	Pb–p 5.02	rare	1×10^{-1} (200 kHz)	77.1 [61.8]	17.1 nb^{-1}	MSH: 18 MUL: 24 EGA: 1.9 TJE: 1.0 MUP: 3.3	731 [151]
	pp 2.76	rare	2.2* (105 kHz)	27.4 [24.9]	129 nb^{-1}	MBand: 20 MSH: 0.89 MUL: 0.53 EGA: 0.43 TJE: 0.036	71 [16]

Table 7. Trigger capabilities of the ALICE detectors.

Detector	Function	Level
SPD	hit-multiplicity based trigger and hit-topology based trigger	L0
TRD	electron trigger, high-p_{T} particle trigger, charged-jet trigger	L1
TOF	multiplicity trigger, topological (back-to-back) trigger, cosmic-ray trigger	L0
PHOS	photon trigger	L0
EMCal	photon trigger, neutral-jet trigger	L0/L1
ACORDE	cosmic-ray trigger (single and multiple hits)	L0
V0	coincidence based minimum-bias interaction trigger, centrality trigger	L0
T0	event-vertex selection trigger, interaction trigger	L0
ZDC	minimum-bias interaction and electromagnetic-dissociation triggers in Pb–Pb	L1
MTR	single-muon trigger, dimuon trigger	L0

(see Sec. 12) is, consequently, focused on continuous read-out of 50 kHz minimum-bias Pb–Pb collisions.

In addition to the running blocks summarized in Table 6, ALICE took data with cosmic ray triggers defined using ACORDE, TOF, and TRD for cosmic-ray studies and detector calibration purposes.[31] The cosmic runs were usually performed in the absence of beams. In 2012, ALICE took $\sim 4 \times 10^6$ cosmic ray events in parallel with the collision data taking, using a high-multiplicity muon trigger (signal on at least 4 scintillator paddles) provided by ACORDE.

3.2. *Trigger*

The trigger decision is generated by the Central Trigger Processor (CTP) of ALICE[32,33] based on detector signals and information about the LHC bunch filling scheme. The detectors that provide input to the trigger decision are listed in Table 7. The CTP evaluates trigger inputs from the trigger detectors every machine clock cycle (~ 25 ns). The Level 0 trigger decision (L0) is made ~ 0.9 μs after the collision using V0, T0, EMCal, PHOS, and MTR. The events accepted at L0 are further evaluated by the Level 1 (L1) trigger algorithm in the CTP. The L1 trigger decision is made 260 LHC clock cycles (~ 6.5 μs) after L0. The latency is caused by the computation time (TRD and EMCal) and propagation times (ZDC, 113 m from IP2). The L0 and L1 decisions, delivered to the detectors with a latency of about 300 ns, trigger the buffering of the event data in the detector front-end electronics. The Level 2 (L2) decision, taken after about 100 μs corresponding to the drift time of the TPC, triggers the sending of the event data to DAQ and, in parallel, to the High Level Trigger system (HLT). During Run 1, all events with L1 were accepted by L2. In the future, in some running scenarios (e.g. when taking downscaled minimum bias events in parallel with rare triggers) L2 may be used to reject events with multiple collisions from different bunch crossings piled-up in the TPC (past–future protection). The events with L2 will subsequently be filtered in the HLT.

Information about the LHC bunch filling scheme was used by CTP to suppress the background. The bunch crossing mask (BCMask) provides the information as to whether there are bunches coming from both A-side and C-side, or one of them,

Table 8. Major ALICE triggers.

Trigger	Description	Condition
MB-type triggers		
MBor	minimum bias	signals in V0 and SPD
MBand	minimum bias	signals in V0A and V0C
MBZ	minimum bias	MB and signals in both ZDC's
SPI	multiplicity trigger	n hits in SPD
Centrality triggers		
CENT	central	V0 based centrality trigger for Pb–Pb (0–10%)
SEMI	semicentral	V0 based semicentral trigger for Pb–Pb (0–50%)
EMCal rare triggers		
E0	EMCal L0	EMCal L0 shower trigger in coincidence with MB
EJE	neutral jet	EMCal L1 jet algorithm following EMCal L0
EJE2	neutral jet	like EJE but with a lower threshold than EJE
EGA	photon/electron	EMCal L1 photon algorithm following EMCal L0
EGA2	photon/electron	like EGA but with a lower threshold than EGA
TRD rare triggers		
TJE	charged jet	n charged particles in TRD chamber in coincidence with MB
TQU	electron for quarkonia	electron with $p_{\mathrm{T}} > 2$ GeV/c in TRD in coincidence with MB
TSE	electron for open beauty	electron with $p_{\mathrm{T}} > 3$ GeV/c in TRD in coincidence with MB
MUON rare triggers		
MSL	single muon low	single muon in MTR in coincidence with MB
MSH	single muon high	like MSL but with a higher threshold
MUL	dimuon unlike sign	two muons above low threshold, unlike sign, in coincidence with MB
MLL	dimuon like sign	two muons above low threshold, same sign, in coincidence with MB
Miscellaneous triggers		
HM	high multiplicity	high multiplicity in SPD in coincidence with MB
PH	photon by PHOS	PHOS energy deposit in coincidence with MB
EE	single electron	electron signal in TRD (sector 6–8) and EMCal
DG	diffractive	charged particle in SPD and no signal in V0
CUP	barrel ultraperipheral	charged particle in SPD and no signal in V0, for Pb–Pb and p–Pb
MUP	muon ultraperipheral	(di-)muon in MTR and no signal in V0A, for Pb–Pb and p–Pb
ZED	electromagnetic dissociation	signal in any of the neutron ZDCs
COS	cosmic trigger	signal in ACORDE

or neither, at a resolution of 25 ns. The beam–gas interaction background was studied by triggering on bunches without a collision partner, and subtracted from the physics data taken with the requirement of the presence of both bunches.

Table 8 summarizes the most important trigger configurations used by ALICE. The minimum bias triggers (MBand and MBor) were used for all pp data taking,

as well as in Pb–Pb in 2010. The high-efficiency MBor trigger was used at low luminosity. Once the luminosity and the background level increased, the high-purity MBand trigger became more advantageous. In the high luminosity Pb–Pb runs in 2011, the V0-based trigger was complemented by a requirement of signals in both ZDCs (MBZ) in order to suppress the electromagnetic interactions between the lead ions. The biased "power-interaction" trigger (SPI) required a certain number of hits (usually around 10) in the SPD. With thresholds on the summed-up signals, V0 was also used to generate central 0–10% (CENT) and semicentral 0–50% (SEMI) Pb–Pb triggers. The thresholds were applied separately to the sums of the output charges of V0A and V0C, then the coincidence of the two sides was required.

The rest of the triggers in Table 8 are rare triggers. The high-multiplicity trigger (HM) was based on the hit multiplicity in the outer layer of the SPD. The multiplicity threshold was typically set to 80–100 hits, corresponding to 60–80 SPD tracklets (pairs of matching clusters in the two layers of SPD). This value was chosen in order to maximize the inspected luminosity without contaminating the sample with multiple-interaction events. The PHOS and EMCal L0 triggers (PH and E0, respectively) required a certain energy deposit within a window of 4×4 calorimeter cells. At L1, EMCal provided triggers on photons/electrons (EGA) and on jets (EJE). The EGA trigger has a higher threshold than E0 and a better handling of supermodule boundaries. The EJE trigger uses a window of 32×32 cells and is primarily sensitive to neutral energy but also includes contributions from charged particles (see Subsec. 10.2.2). The TRD trigger was introduced in the 2012 pp runs. A fraction (limited to 10 to 25 kHz) of the minimum bias triggers at L0 were subject to a TRD L1 decision. At L1, four algorithms were implemented: jet trigger (TJE), single electron trigger (TSE), quarkonium electron trigger (TQU), and TRD+EMCal electron trigger (EE). The jet trigger requires at least 3 charged particle tracks with $p_{\mathrm{T}} > 3$ GeV/c to be detected in one TRD stack. A TRD stack consists of 6 layers of chambers in radial direction and covers $\Delta\eta \approx \Delta\phi \approx 0.1$. 13 TRD supermodules, five stacks each, were installed and operational in the 2012 and 2013 runs. The electron trigger required an electron PID based on a threshold for the electron likelihood calculated from the integrated signal of each layer. The quarkonia electron trigger required a lower p_{T} threshold of 2 GeV/c with a tighter electron likelihood cut. This enables the detection of low momentum electrons from J/ψ and ψ' decays. In contrast to the TJE, TQU, and TSE triggers, the high-purity electron trigger EE was inspecting all events with EMCal Level 0 trigger (E0). The TRD trigger condition for EE was the same as for the single electron trigger; however, the acceptance was limited to the TRD sectors (supermodules 6, 7, and 8) that overlap with the acceptance of EMCal. A signal in the innermost TRD layer was required for all TRD electron triggers in order to suppress the background caused by late photon conversions.

All of the muon triggers were implemented at Level 0. There were two single-muon triggers (MSL and MSH) and two dimuon triggers (MUL and MLL), all in coincidence with MB. A low p_{T} threshold was used for MSL, MUL, and MLL, and

a high one for the MSH trigger. The low-threshold single-muon trigger MSL was downscaled when used in parallel with MSH. The unlike-sign muon-pair trigger MUL, used for measuring mesons, was complemented by the like-sign (MLL) one for the combinatorial background estimation. The low and high p_{T} thresholds were 0.5–1.0 GeV/c and 1.7–4.2 GeV/c, respectively, adjusted according to the run type.

Several additional triggers were implemented in order to enhance events related to diffractive physics in pp and ultraperipheral nuclear collisions, and to measure cosmic rays. The DG (double gap) trigger in pp required a particle at midrapidity and no particles within the intermediate pseudorapidity ranges covered by the V0 detector. The CUP (central-rapidity ultraperipheral) trigger performed a similar selection in collision systems involving ions. An analogous condition, but with a forward muon rather than a midrapidity particle, was named the MUP (muon ultraperipheral) trigger. Finally, a cosmic trigger defined by ACORDE (COS) was active during most of 2012 to collect high muon multiplicity cosmic events.

The rare triggers implemented in TRD, EMCal, and MUON are further discussed in Secs. 8, 10 and 11. Physics results based on analyses of E0-, MSL-, and MUP-triggered events were published in Refs. 28, 34 and 27, respectively.

The instantaneous rate and the total number of collected events in Run 1 are shown for selected triggers in Fig. 9. The minimum bias and rare-trigger running modes are illustrated in detail for the p–Pb data taking in 2013 in Fig. 10.

The total number of recorded events and the inspected luminosity are shown in Table 6 for selected minimum-bias and rare triggers, respectively. The values are based on raw trigger counts. The luminosities were determined for reference triggers as described in Subsec. 2.3. For rare triggers, for which no direct measurement of cross section was performed, the integrated luminosity was estimated by comparing their rates to that of a reference trigger. The resulting uncertainty is typically about 10%. Another uncertainty of up to 20% comes from the fact that this simple method does not account for the trigger purity. The actual statistics useful for physics analysis may thus fall significantly below the numbers given in the table.

3.3. *Readout*

The ALICE detectors are equipped with standardized optical fiber based data transmission devices working at a bandwidth of 200 MB/s. Some of the detectors have multiple data transmission connections. Event data are sent to DAQ and HLT where event building and data compression are performed. Trigger detectors provide low-voltage differential signals (LVDS) to the CTP inputs. The CTP makes the global ALICE trigger decision as described in Subsec. 3.2. In conjunction with the LHC clock and bunch filling scheme, this decision is propagated to all detectors, to DAQ, and to HLT via the TTC (Timing, Trigger, and Control)[35] passive optical transmission network system. The LHC clock is used to synchronize the data of all detectors with the bunch crossing.

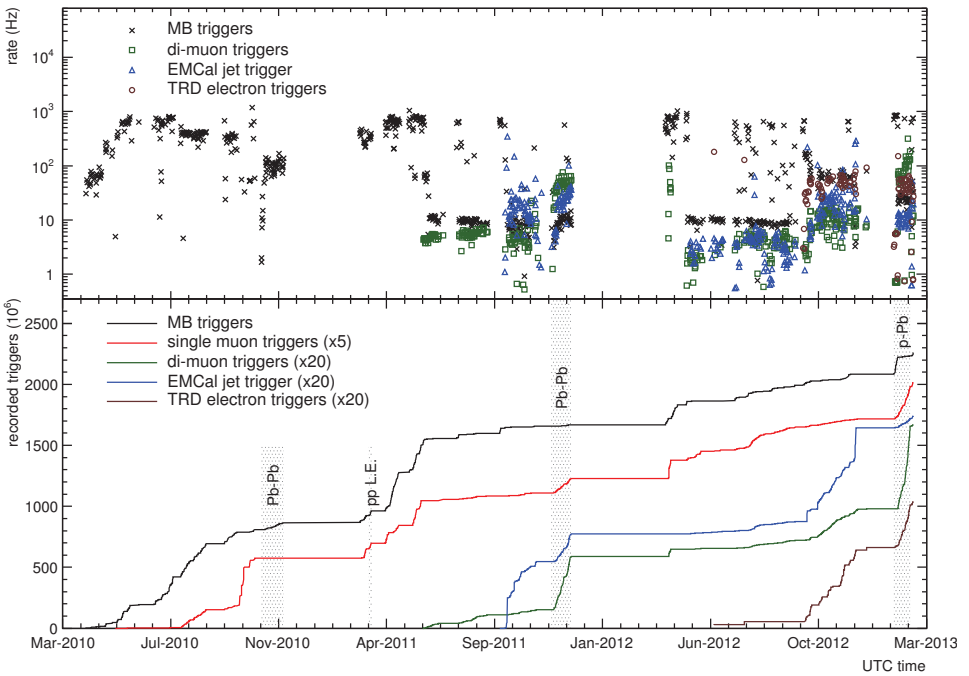

Fig. 9. Instantaneous rate (top) and number of collected events (bottom) for selected triggers in the running periods from 2010 to 2013. Special running periods (Pb–Pb, p–Pb, low energy pp) are indicated by shaded areas; the rest represents pp runs at the highest available energy.

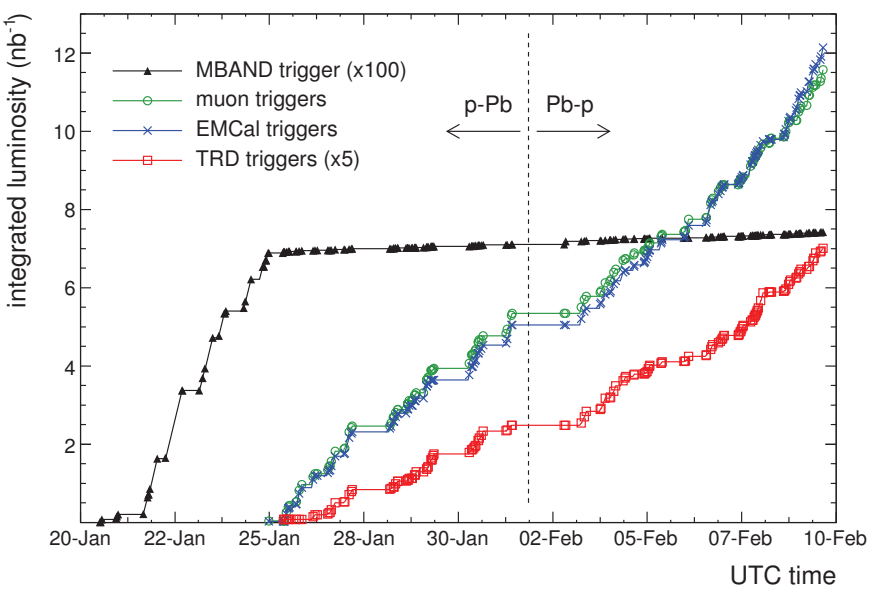

Fig. 10. Integrated luminosity in the 2013 p–Pb run, collected in the minimum bias and the rare-trigger mode (before and after January 25, respectively).

Table 9. Average busy times and event sizes of the ALICE detectors observed in typical rare-trigger pp runs in 2012, Pb–Pb runs in 2011, and p–Pb runs in 2013. ZDC was not active in the 2012 pp running therefore no value is given for the data size. In p–Pb runs, SPD busy time was either 0 or 370 μs depending on the running mode.

	pp		Pb–Pb		p–Pb	
Detector	Busy time (μs)	Data size (kB)	Busy time (μs)	Data size (kB)	Busy time (μs)	Data size (kB)
SPD	0	7	0	26	0 or 370	7
SDD	1024	22	1024	143	1024	16
SSD	265	46	265	180	265	42
TPC	500	6676	500	25740	350	15360
TRD	300	181	450	3753	270	350
TOF	0	23	0	63	0	23
PHOS	850	25	850	72	850	35
EMCal	270	22	300	53	270	25
HMPID	220	15	300	22	220	18
ACORDE	116	0.1	116	0.1	116	0.1
PMD	170	10	220	50	170	8
FMD	190	14	350	55	190	13
V0	0	6	0	6	0	6
T0	0	0.4	0	0.7	0	0.6
ZDC	122	—	122	0.8	122	0.7
MCH	300	35	300	61	250	18
MTR	160	7	160	7	160	7

The busy time of the data taking is mainly defined by the CTP waiting for the completion of the readout of all detectors. In addition, L1-rejected events contribute to the busy time because of the latency of the L1 decision. The detector busy time due to readout, in general, depends on the event size and thus on the collision system and background conditions. The ability to buffer events, possessed by some of the detectors, reduces their respective average busy times by a rate-dependent factor. The typical readout performance of the ALICE detectors in recent pp, Pb–Pb, and p–Pb runs is summarized in Table 9. By virtue of event buffering, SPD, TOF, T0, and V0 do not cause a "detector busy" state. TPC and TRD have multi-event buffers which efficiently reduce their busy times in rare-trigger pp and Pb–Pb runs at event rates of 200–300 Hz. The TPC busy duration is identical in these two collision systems although the event sizes are very different. The TPC busy time includes a protection period of approximately 300 μs covering the electron drift and the ion collection times.

The ALICE data volume is dominated by the event size of the TPC. The latter scales with the charged-particle multiplicity, including pileup tracks from other interactions within the TPC drift time window of $\sim$100 μs. The maximum TPC event size, observed in central Pb–Pb collisions, was 70 MB.

3.4. *Online data compression*

Over the course of preparations for the Pb–Pb run in 2011 it was estimated that the data rate would exceed the maximum bandwidth of the connection to mass storage. The data volume was then reduced by storing TPC cluster information instead of raw data, using online processing by HLT.[36,37] The reduced data are further compressed by HLT using lossless compression with Huffman encoding.[38] The procedure was tested during the pp runs in 2011, and successfully used in the lead-ion run and all subsequent data taking. For integrity checks, 1% of the events were recorded without compression. This way, a data compression by a factor of 5 was achieved for the TPC data. As the TPC is the dominant contributor to the event size, the compression factor for the total data volume in 2012 p–Pb running was about 4. The effect of the compression can be seen from the difference between "data read" and "data recorded" in Table 6.

4. Calibration Strategy

The momentum resolution and the particle identification performance critically depend on the quality of the calibration. The actual positions of the detectors (alignment), maps of dead or noisy elements, and time and amplitude calibrations are used in the reconstruction. For the drift detectors (SDD, TPC, TRD), the gain and the time response are calibrated differentially in space (single readout pads for TPC and TRD) and time (units of 15 minutes for TPC). Finally, the geometry of the luminous region and (for Pb–Pb collisions) calibrated centrality and event plane are important for physics analysis.

In this section we briefly describe the main sources of the various calibration parameters. Once determined, the calibration parameters are stored in the Offline Conditions Database (OCDB) and thus become accessible for reconstruction jobs running on the distributed computing Grid. The list of the calibration parameters, organized according to the source, is given in Table 10.

4.1. *Condition data and online calibration*

Condition data are monitored continuously and archived by the Detector Control System (DCS). Some of these data (e.g. temperatures and pressures) affect the detector response and thus are relevant to event reconstruction.

Those calibration parameters that can be derived from raw data are extracted online, i.e. during data taking, from interaction events and/or dedicated calibration events. The latter can be collected in dedicated calibration runs or in parallel with the physics data taking. The data processing takes place on the computers of the Data Acquisition (DAQ) system.[39]

At the end of each run the condition data and the online calibration parameters are collected by the Shuttle system[40] and transported to the OCDB. A successful Shuttle termination triggers the first reconstruction pass of the run.

Table 10. Calibration parameters used in the reconstruction, ordered according to their source. The following abbreviations are used: "v_{drift}" — drift velocity, "t_0" — time offset, "T" — temperature, "P" — pressure, "ped" — pedestals, "peds" — pedestal runs, "inject" — injector runs, "puls" — pulser runs, "laser" — laser runs/events, "LED" — LED runs/events, "Kr" — runs with radioactive krypton in the gas.

System	Condition data	Special runs	Physics runs online	After cpass0	After cpass1	After full pass
SPD	trigger chip map and thresholds		half-stave status pixel noise			pixel status (only for MC)
SDD		anode ped (peds) anode gain, status (puls) anode v_{drift} (inject)			anode gain ($r\phi$) anode $v_{\text{drift}}(r\phi)$ anode t_0	
SSD		strip ped, noise, status (peds)				module-side gain
TPC	P, $T(x, y, z)$ pad status trigger t_0	pad gain (Kr) pad noise (peds) v_{drift} (laser) pad status (puls)	v_{drift} (laser)	$v_{\text{drift}}(x, y)$, $t_0(x, y)$, alignment gain, attachment	as in cpass0 but higher granularity; Bethe-Bloch par.	
TRD		pad gain (Kr) pad noise, status (peds)		cham status, gain, t_0, v_{drift}, $E \times B$		det PID
TOF	channel status TDC t_0 BPTX t_0	pad noise (peds)	pad noise (calib) TDC status	t_0		pad t_0 pad slewing
PHOS		cell gain (LED)				cell gain, t_0 cell status
EMCal	supermodule T		cell gain (LED)		cell status	cell gain, t_0

Table 10 (*Continued*)

System	Condition data	Special runs	Physics runs online	After cpass0	After cpass1	After full pass
HMPID	chamber P, HV radiator T and transparency	pad ped, noise, status (peds)	pad noise, status			
ACORDE						
PMD		cell ped	cell gain			cell gain, status
FMD		strip ped, noise (peds) strip gain (puls)				strip gain
V0	PMT HV, trigger thresh. and t_0	PMT slewing (once)	PMT ped, noise, gain			
T0		PMT slewing	PMT t_0	t_0		
ZDC		ped (peds)	PMT t_0			PMT gain
MCH	chamber HV	pad ped, noise, status (peds), pad gain (puls)	noisy pads			alignment
MTR		strip, board status (puls)	strip, board status (special events)			
luminous region			x, y, z, σ_z from SPD	x, y, z, σ_x, σ_y, σ_z		
centrality				centrality from SPD, V0		centrality from TPC

4.2. *Offline calibration*

The first two reconstruction passes are performed on a sample of events from each run and serve for calibration and monitoring purposes. The first pass (cpass0) provides input for the calibration of TPC, TRD, TOF, T0, luminous region, and centrality. The second pass (cpass1) applies the calibration, and the reconstructed events are used as input for data quality assurance and for improved calibration of SDD, TPC, and EMCal. Once a data taking period (typically 4–6 weeks) is completed, a manual calibration spanning many runs is performed. The complete calibration is then verified by a validation pass (vpass) performed on a sample of events from all runs in the period. The subsequent physics reconstruction pass (ppass) is, in general, performed on all events and provides the input for physics analysis.

The complete calibration reconstruction sequence is thus: cpass0, calibration, cpass1, quality assurance and calibration, manual multi-run calibration, validation pass, quality assurance, physics reconstruction pass, quality assurance.

4.3. *Detector alignment*

The objective of the data-driven alignment of detectors is to account for deviations of the actual positions of sensitive volumes and material blocks from the nominal ones in the reconstruction and simulation software. In order to achieve this, first for those detectors for which standalone reconstruction is possible (ITS, TPC, TRD, MUON) an internal alignment (e.g. positions of ITS sensors with respect to the sensor staves and of staves with respect to the ITS center; relative positions of TRD chambers within a stack; etc.) was performed. This was done by iterative minimization of the residuals between the cluster positions (measured under the current assumption of alignment parameters) and the tracks to which these clusters were attached by the reconstruction procedure. Given the large number of degrees of freedom in the ITS and MUON detectors (14622 and 1488, respectively) their alignment was performed using a modified version of the Millepede algorithm.[41] The alignment of ITS,[42] TPC, and TRD was initially performed using the cosmic muons data, and then it was refined using tracks reconstructed in the collision events collected in physics runs as well as in dedicated runs without magnetic field. For the alignment of the MUON detector, muon tracks from runs with and without magnetic field were used together with the information from the optical geometric monitoring system.[43,44] The precision of the internal alignment in the ITS is estimated to be on the level of $\sim 10\,(70)$, $25\,(20)$, and $15\,(500)$ μm in the bending (nonbending) direction for SPD, SDD, and SSD layers, respectively. For MUON, the alignment precision is estimated to be better than 50–100 (100–150) μm in the bending (nonbending) direction, depending on muon station. The precision of the inter-sector alignment in the TPC is estimated to be ~ 0.1 mm.

After the internal alignment, the ITS and TPC were aligned to each other to a precision of ~ 30 μm and ~ 0.1 mrad by applying a Kalman-filter based procedure of minimizing the residuals between the tracks reconstructed in each detector.

The global alignment of other central-barrel detectors was performed by minimizing the residuals between their clusters and the extrapolation of the ITS–TPC tracks. The residual misalignment in the $r\phi$ and z directions is estimated to be smaller than ~ 0.6 mm for the TRD, ~ 5 mm for the TOF, 5–10 mm depending on chamber for HMPID, ~ 6 mm for the PHOS, and ~ 2 mm for the EMCal. The global alignment of MUON is performed by requiring the convergence of the muon tracks to the interaction vertex.

The alignment is checked and, if necessary, redone after shutdowns and/or interventions that may affect the detector positions. In order to minimize the influence of the residual misalignment on the reconstructed data, the physics measurements in ALICE are routinely performed with both magnetic field polarities.

5. Event Characterization

For spherical nuclei, the geometry of heavy-ion collisions is characterized by the impact parameter vector $\mathbf{b}$ connecting the centers of the two colliding nuclei in the plane transverse to the beams. In the experiment, the centrality (related to $b := |\mathbf{b}|$) and the reaction-plane angle (azimuthal angle of $\mathbf{b}$) are estimated using the particle multiplicities and/or the zero-degree energy, and the anisotropies of particle emission, respectively. Below we sketch the methods and quote the resolution achieved in these variables. A more detailed discussion of the centrality determination in ALICE can be found in Ref. 45.

5.1. *Centrality*

It is customary to express the centrality of nuclear collisions not in terms of the impact parameter b but via a percentage of the total hadronic interaction cross section σ_{AA}. The centrality percentile c of an AA collision with impact parameter b is defined as

$$c(b) = \frac{\int_0^b \frac{\mathrm{d}\sigma}{\mathrm{d}b'}\mathrm{d}b'}{\int_0^\infty \frac{\mathrm{d}\sigma}{\mathrm{d}b'}\mathrm{d}b'} = \frac{1}{\sigma_{AA}} \int_0^b \frac{\mathrm{d}\sigma}{\mathrm{d}b'}\,\mathrm{d}b' \,. \tag{3}$$

Experimentally, the centrality is defined as the fraction of cross section with the largest detected charged-particle multiplicity N_{ch} or the smallest zero-degree energy E_{ZDC}:

$$c \approx \frac{1}{\sigma_{AA}} \int_{N_{\mathrm{ch}}}^\infty \frac{\mathrm{d}\sigma}{\mathrm{d}N'_{\mathrm{ch}}}\,\mathrm{d}N'_{\mathrm{ch}} \approx \frac{1}{\sigma_{AA}} \int_0^{E_{\mathrm{ZDC}}} \frac{\mathrm{d}\sigma}{\mathrm{d}E'_{\mathrm{ZDC}}}\,\mathrm{d}E'_{\mathrm{ZDC}} \,. \tag{4}$$

The cross section may be replaced with the number of observed events n (corrected for the trigger efficiency and for the nonhadronic interaction background):

$$c \approx \frac{1}{N_{\mathrm{ev}}} \int_{N_{\mathrm{ch}}}^\infty \frac{\mathrm{d}n}{\mathrm{d}N'_{\mathrm{ch}}}\,\mathrm{d}N'_{\mathrm{ch}} \approx \frac{1}{N_{\mathrm{ev}}} \int_0^{E_{\mathrm{ZDC}}} \frac{\mathrm{d}n}{\mathrm{d}E'_{\mathrm{ZDC}}}\,\mathrm{d}E'_{\mathrm{ZDC}} \,. \tag{5}$$

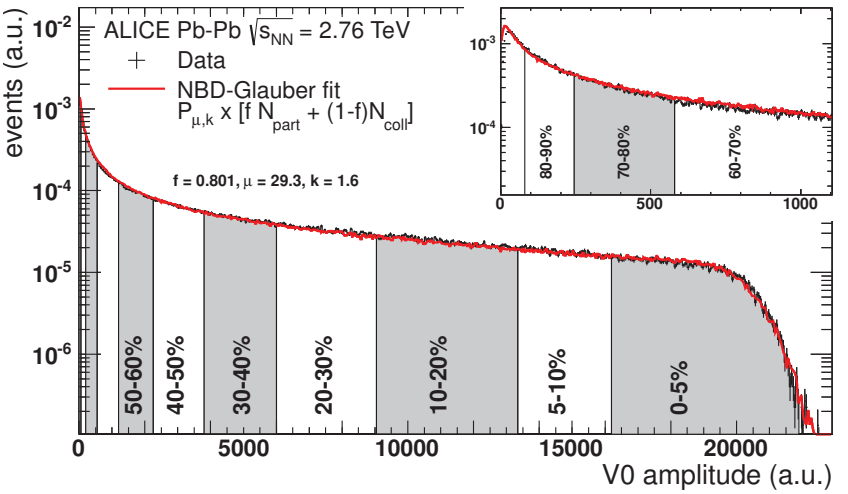

Fig. 11. (Color online) Distribution of the V0 amplitude (sum of V0A and V0C). The centrality bins are defined by integrating from right to left following Eq. (5). The absolute scale is determined by fitting to a model (red line), see below for details. The inset shows a magnified version of the most peripheral region.

Equations (4) and (5) are based on the assumption that, on average, the particle multiplicity at midrapidity (the zero-degree energy) increases (decreases) monotonically with the overlap volume, i.e. with centrality. For the zero-degree energy measurement (5), this assumption holds only for central collisions $c \lesssim 50\%$, because nuclear fragments emitted in peripheral collisions may be deflected out of the acceptance of the zero-degree calorimeter, leading to low signals indistinguishable from those seen in central collisions.

The centrality determination via the particle multiplicity in V0 is illustrated in Fig. 11. The V0 multiplicity (sum of V0A and V0C amplitudes) distribution was recorded in Pb–Pb collisions at $\sqrt{s_{\rm NN}} = 2.76$ TeV, requiring a coincidence of V0 and SPD, and using ZDC to reduce the electromagnetic dissociation background. Machine-induced background and parasitic collisions are removed using the timing information from V0 and ZDC. The analysis is restricted to events with a vertex position within $|z_{\rm vtx}| \lesssim 10$ cm. The centrality bins are defined by integrating the charged-particle multiplicity distribution following Eq. (5), and the absolute scale is determined by fitting to a model as described below.

The distribution of the energy deposited in the zero-degree calorimeter is shown in Fig. 12. The ambiguity between central and peripheral collisions with undetected nuclear fragments is resolved by correlating the zero-degree signal with the amplitude of the electromagnetic calorimeter at $4.8 < \eta < 5.7$ (ZEM).

An absolute determination of centrality according to Eqs. (4) or (5) requires knowledge of the total hadronic cross section σ_{AA} or the total number of events $N_{\rm ev}$, respectively. The total hadronic cross section σ_{AA} for Pb–Pb at $\sqrt{s_{\rm NN}} = 2.76$ TeV was measured in ALICE in a special run triggering on signals in the

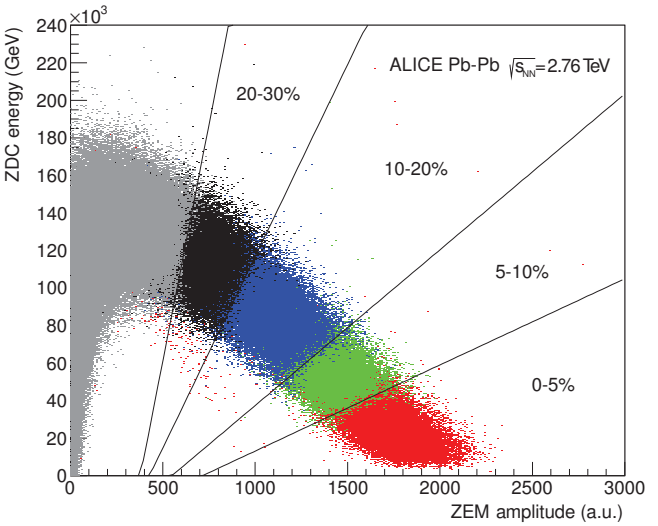

Fig. 12. (Color online) Correlation between the total energy deposited in the zero-degree calorimeters and the ZEM amplitude. The centrality bins defined based on this distribution (lines) are compared to the centrality from V0 (colored dots).

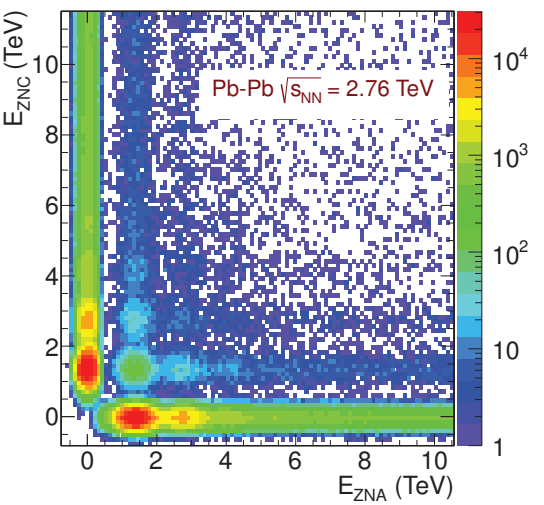

Fig. 13. Correlation between signals in the two neutron zero-degree calorimeters. Single electromagnetic dissociation events produce a signal in only one of the calorimeters. Mutual dissociation and hadronic interactions populate the interior of the plot and can be distinguished from each other by the signal in ZEM.

neutron zero-degree calorimeters (ZNs) with a threshold well below the signal of a 1.38 TeV neutron.[25] The recorded event sample is dominated by the electromagnetic dissociation (EMD) of one or both nuclei. The single EMD events can be clearly identified in the correlation plot between the two ZNs (Fig. 13). An additional

requirement of a signal in ZEM (see Sec. 1) allows one to distinguish between the mutual EMD and the hadronic interaction events. With the absolute normalization determined by means of a van der Meer scan as described in Subsec. 2.3.3, a hadronic cross section of $\sigma_{\mathrm{PbPb}} = \left(7.7 \pm 0.1(\mathrm{stat})^{+0.6}_{-0.5}(\mathrm{syst})\right)$ b was obtained. The centrality may then be derived from the calorimeter signals using Eq. (4).

A higher accuracy of the centrality calibration can be achieved by normalizing the measured event yield to the total number of events N_{ev} that would be registered in an ideal case, i.e. without background interactions and with a perfect trigger efficiency (Eq. (5)). This was the method of choice in ALICE. The high-multiplicity part of the multiplicity distribution was fitted by the Glauber model (red line in Fig. 11), and the extrapolation of the model was used to determine the unbiased number of events at low multiplicities. The Glauber model describes the collision geometry using the nuclear density profile, assuming that nucleons follow straight line trajectories and encounter binary nucleon–nucleon collisions according to an inelastic nucleon–nucleon cross section σ_{NN}. For the latter, 64 mb was assumed in the calculation; this value is consistent with the subsequent ALICE pp measurement reported in Subsec. 2.3.4. The number of binary NN collisions N_{coll} and the number of participants N_{part} (nucleons which underwent a NN collision) are determined for a given impact parameter. The multiplicity distribution was modeled assuming $fN_{\mathrm{part}} + (1-f)N_{\mathrm{coll}}$ particle sources, with each source producing particles following a negative binomial distribution (NBD) with fit parameters μ and k. The parameter f represents the contribution of soft processes to the particle production. The fit provides the integrated number of events N_{ev} needed for the absolute centrality scale and relates the number of participants and binary NN collisions to the centrality. The latter relation is presented in detail in Ref. 45.

The centrality for each event can be independently calculated from the multiplicities seen in V0A, V0C, ZDC, SPD, and TPC. The resolution of each of these centrality estimators, defined as their r.m.s. for a sample of events with a fixed b, was determined by studying correlations between them and is shown in Fig. 14. The resolution ranges from 0.5% to 4% depending on centrality and on the detector used. As expected, the resolution of each detector depends on its rapidity coverage, scaling with $\sim 1/\sqrt{N_{\mathrm{ch}}}$.

5.2. *Event plane*

The orientation of the reaction plane or, in case of flow fluctuations, the nth-harmonic collision symmetry plane is estimated with the nth-harmonic event-plane angle, Ψ_n^{EP}.[46] For a given harmonic n, one constructs the two-dimensional event-plane vector $\mathbf{Q}_n$ from the measured azimuthal distribution of particles produced in the event as follows:

$$\mathbf{Q}_n = (Q_{n,x}, Q_{n,y}) = \left(\sum_i w_i \cos n\phi_i, \sum_i w_i \sin n\phi_i \right). \tag{6}$$

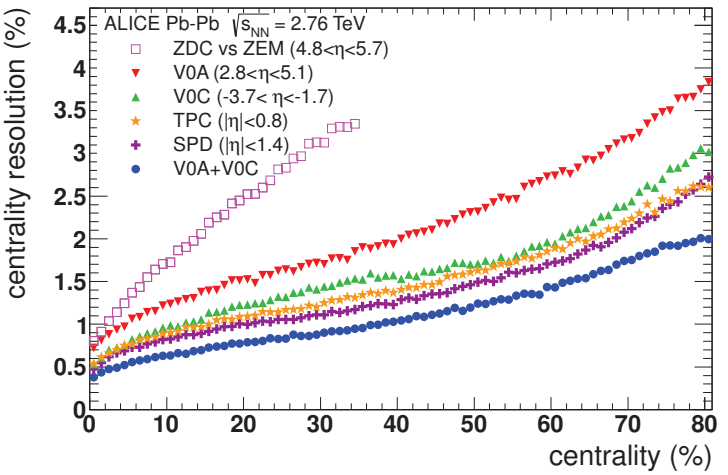

Fig. 14. Resolution of various centrality estimators.

Here the sum runs over all reconstructed tracks in the case of the TPC, or segments of the detectors with azimuthal segmentation like V0, FMD, ZDC, or PMD. The angle ϕ_i is the azimuthal emission angle of the particle i or the azimuthal coordinate of the detector element i, respectively. For TPC tracks the weight w_i can be unity or a specific function of p_{T}.[46] For segmented detectors, w_i is the signal observed in the detector element i. Using the components of the **Q**-vector one can calculate the Ψ_n^{EP}:[46]

$$\Psi_n^{\mathrm{EP}} = \frac{1}{n} \arctan 2(Q_{n,y}, Q_{n,x}) \,. \tag{7}$$

The correction for the finite event-plane angle resolution can be calculated using the two- or three- (sub-)detector correlation technique. The resolution correction factor, in the following for brevity called "resolution," is close to zero (unity) for poor (perfect) reconstruction of the collision symmetry plane. In case of two (sub-) detectors A and B the subevent resolution is defined as

$$R_n^{\mathrm{sub}} = \sqrt{\langle \cos n(\Psi_n^A - \Psi_n^B) \rangle} \,, \tag{8}$$

where Ψ_n^A and Ψ_n^B are the event-plane angles of the two subevents, and the angle brackets denote the average over an ensemble of the events. Typically, the same harmonic is used in the flow measurement and for the event-plane determination. In this case, the full event-plane resolution, i.e. the correlation between the event-plane angle for the combined subevents and the reaction-plane angle, can be calculated from[46]

$$R_n(\chi) = \sqrt{\pi}/2\chi \exp(-\chi^2/2)(I_0(\chi^2/2) + I_1(\chi^2/2)) \,, \tag{9}$$

$$R_n^{\mathrm{full}} = R_n\big(\sqrt{2}\chi_{\mathrm{sub}}\big) \,. \tag{10}$$

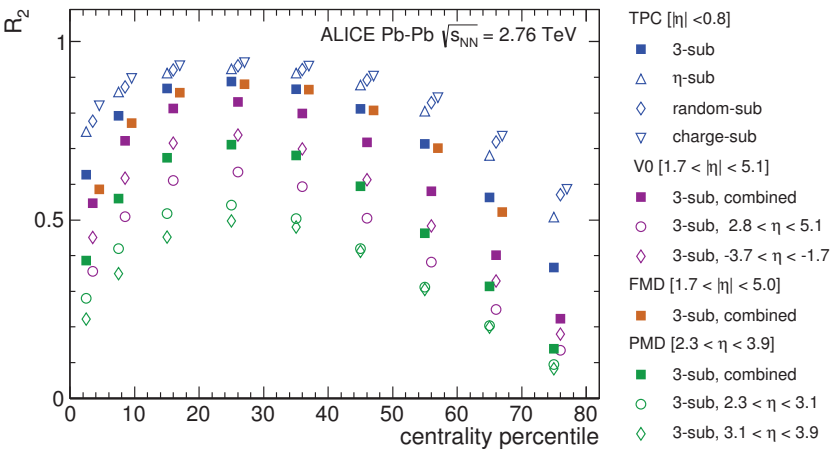

Fig. 15. Resolution of the second-order event-plane angle, Ψ_2^{EP}, extracted from two- and three-detector subevent correlations for TPC, V0, FMD, and PMD.

The variable χ represents the magnitude of flow normalized to the precision with which it can be measured, and I_0, I_1 are the modified Bessel functions. In case of (sub-)detectors with different kinematic coverages, such as V0A and V0C, a three-detector subevent technique can be used. In this case, the resolution for a given detector can be defined from the correlation between each detector pair

$$R_n^A = \sqrt{\frac{\left\langle \cos n\left(\Psi_n^A - \Psi_n^C\right)\right\rangle \left\langle \cos n\left(\Psi_n^A - \Psi_n^B\right)\right\rangle}{\left\langle \cos n\left(\Psi_n^B - \Psi_n^C\right)\right\rangle}}, \tag{11}$$

where Ψ_n^A is the event-plane angle for which the resolution is calculated, and B and C are any other two (sub-)detectors. One can get the resolution for each of the three detectors by permutation of the event-plane angles for all three detectors. Note that nonflow correlations and the effects of flow fluctuations can result in different resolutions being extracted for the same detector from two- or three- (sub-)detector correlations.

5.2.1. *Event plane from elliptic flow*

The dominant component of the anisotropic flow in mid-central collisions at LHC energies is the elliptic flow. Consequently, the resolution of the second-order event plane is the best. Figure 15 shows the resolution R_2 of the second-order event-plane angle Ψ_2^{EP}, extracted from two- and three-detector subevent correlations for TPC, V0, FMD, and PMD, versus the collision centrality. Effects from the azimuthal nonuniformity of the detectors, which may result in nonphysical correlations, were corrected at the time of the event-plane angle calculations. The resolution R_2 for charged particles measured in the TPC detector was calculated using four different methods: by randomly dividing particles into two subevents

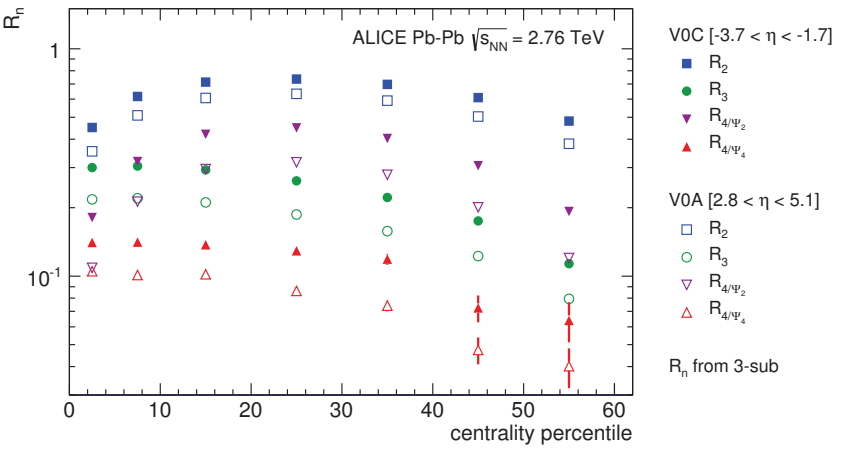

Fig. 16. Event-plane angle, Ψ_n^{EP}, resolution for $n = 2, 3$, and 4, calculated with a three-detector subevent technique separately for V0A and V0C detectors.

(denoted as "random-sub"), by constructing subevents from particles with opposite charges ("charge-sub") or particles separated by a rapidity gap of at least 0.4 units ("η-sub"), and from three-detector subevent correlations in combination with the V0A and V0C detectors ("3-sub"). Variations in the event-plane resolution calculated with different methods indicate differences in their sensitivity to the correlations unrelated to the reaction plane (nonflow) and/or flow fluctuations.

5.2.2. *Event plane from higher harmonics*

Figure 16 shows the resolution of the event-plane angle, Ψ_n^{EP}, for the $n = 2, 3$, and 4 harmonics calculated with a three-detector subevent technique separately for the V0A and V0C detectors. The TPC was used as a third, reference, detector. The ordering of the resolutions for mid-central collisions in Fig. 16 reflects the fact that higher harmonics of the anisotropic flow are gradually suppressed. At the same time, even with small signals we still can statistically resolve higher-harmonic event-plane angles with resolutions of the order of a few percent.

5.2.3. *Event plane from spectator deflection*

In noncentral nuclear collisions at relativistic energies, the spectator nucleons are assumed to be deflected in the reaction plane away from the center of the system. The first-order event-plane angle, which provides an experimental estimate of the orientation of the impact parameter vector **b**, can be reconstructed using the neutron ZDCs.[1] Located about a hundred meters from the interaction point, these detectors are sensitive to neutron spectators at beam rapidity. Each ZDC, A-side ($\eta > 0$) and C-side ($\eta < 0$), has a 2×2 tower geometry. Event-by-event spectator

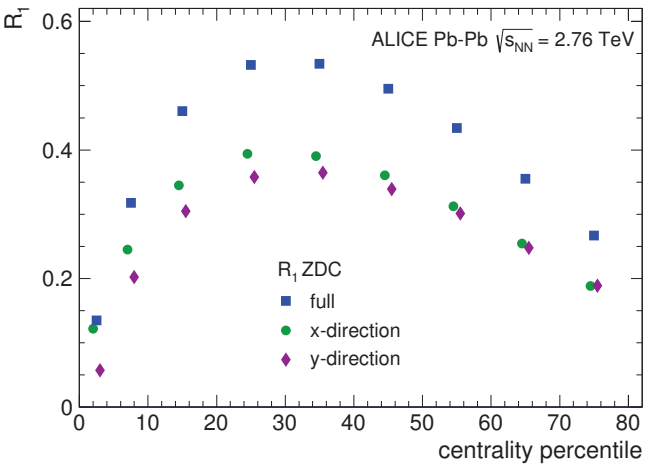

Fig. 17. Resolution of the first-harmonic event plane estimated from spectator deflection, as measured by the two ZDCs.

deflection is estimated from the ZDC centroid shifts $\mathbf{Q_1}$:

$$\mathbf{Q_1} = \sum_{i=1}^{4} \mathbf{r}_i E_i \Big/ \sum_{i=1}^{4} E_i \,, \tag{12}$$

where $\mathbf{r}_i = (x_i, y_i)$ and E_i are the coordinates and the recorded signal of the ith ZDC tower, respectively. To correct for the time-dependent variation of the beam crossing position and event-by-event spread of the collision vertex with respect to the center of the TPC we perform the recentering procedure:

$$\mathbf{Q_1'} = \mathbf{Q_1} - \langle \mathbf{Q_1} \rangle \,. \tag{13}$$

Recentering (subtracting the average centroid position $\langle \mathbf{Q_1} \rangle$) is performed as a function of time, collision centrality, and transverse position of the collision vertex. After recentering we observe an anticorrelation of the spectator deflections on the A and C sides. This demonstrates the capability to measure directed flow using the ZDCs. Figure 17 shows, as a function of centrality, the first-order event-plane resolution obtained from two different transverse directions x and y in the detector laboratory frame together with the combined resolution from both ZDCs.

6. Central Barrel Tracking

This section describes track finding in the central barrel. The procedure, shown schematically in Fig. 18, starts with the clusterization step, in which the detector data are converted into "clusters" characterized by positions, signal amplitudes, signal times, etc., and their associated errors. The clusterization is performed separately for each detector. The next step is to determine the preliminary interaction vertex using clusters in the first two ITS layers (SPD). Subsequently, track finding and fitting is performed in TPC and ITS using the Kalman filter technique.[47]

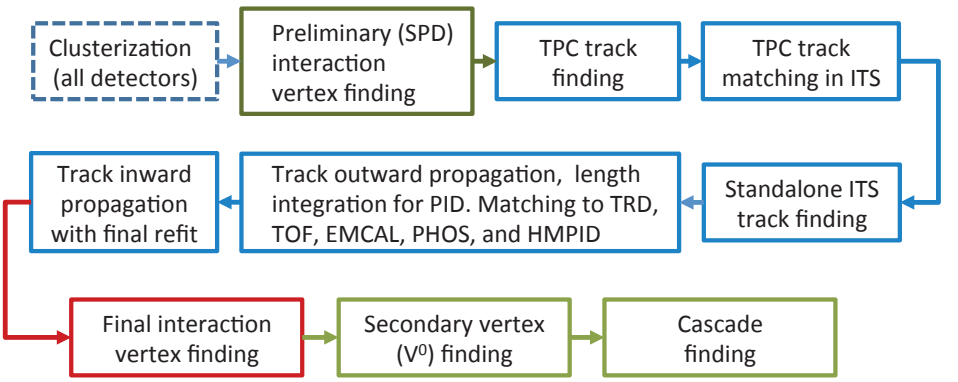

Fig. 18. Event reconstruction flow.

The found tracks are matched to the other central-barrel detectors and fitted. The final interaction vertex is determined using the reconstructed tracks. A search for photon conversions and decays of strange hadrons K^0_S/Λ (denoted as V^0), $\Xi^{\pm}$, and $\Omega^{\pm}$ concludes the central-barrel tracking procedure. The steps are described in further detail in this section.

6.1. *Preliminary determination of the interaction vertex*

Tracking in the central barrel starts with the determination of the interaction vertex using the two innermost layers (SPD) of the ITS. It is found as a space point to which a maximum number of tracklets (lines defined by pairs of clusters, one cluster in each SPD layer) converge. In pp collisions, where interaction pileup is expected, the algorithm is repeated several times, discarding at each iteration those clusters which contributed to already-found vertices. By construction, the first vertex found has the largest number of contributing tracklets and is assumed to be the primary one. When a single convergence point is not found (particularly in low-multiplicity events) the algorithm performs a one-dimensional search of the maximum in the z-distribution of the points of closest approach (PCA) of tracklets to the nominal beam axis.

6.2. *Track reconstruction*

Track finding and fitting is performed in three stages, following an inward–outward–inward scheme.[48,49]

The first inward stage starts with finding tracks in the TPC. The TPC readout chambers have 159 tangential pad rows and thus a track can, ideally, produce 159 clusters within the TPC volume. The track search in the TPC starts at a large radius. Track seeds are built first with two TPC clusters and the vertex point, then with three clusters and without the vertex constraint. The seeds are propagated inward and, at each step, updated with the nearest cluster provided that it fulfills

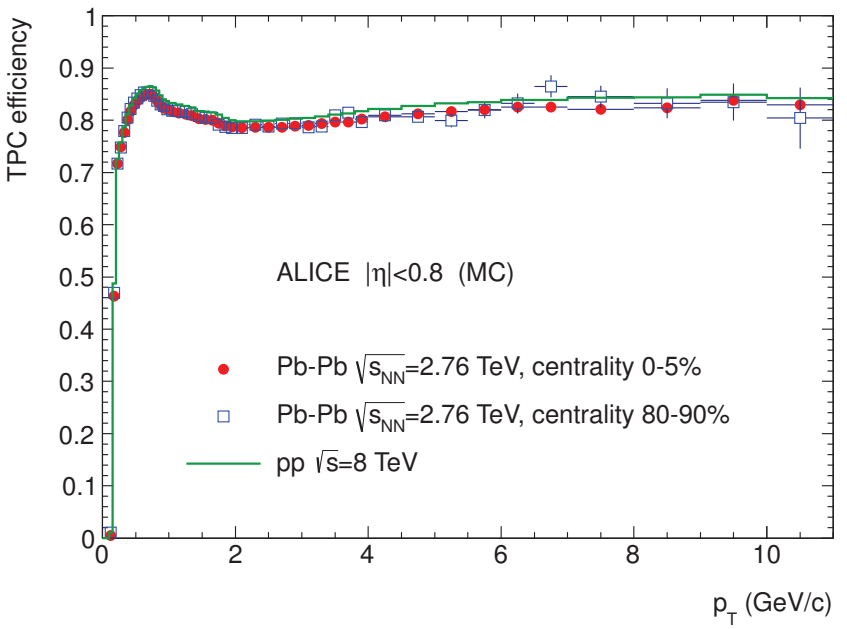

Fig. 19. TPC track finding efficiency for primary particles in pp and Pb–Pb collisions (simulation). The efficiency does not depend on the detector occupancy.

a proximity cut. Since the clusters can be reused by different seeds, the same physical track can be reconstructed multiple times. In order to avoid this, a special algorithm is used to search for pairs of tracks with a fraction of common clusters exceeding a certain limit (between 25% and 50%). The worse of the two is rejected according to a quality parameter based on the cluster density, number of clusters, and momentum. Only those tracks that have at least 20 clusters (out of maximum 159 possible) and that miss no more than 50% of the clusters expected for a given track position are accepted. These are then propagated inwards to the inner TPC radius. A preliminary particle identification is done based on the specific energy loss in the TPC gas (see Sec. 7). The most-probable-mass assignment is used in the ionization energy loss correction calculations in the consecutive tracking steps. (Due to the ambiguity of electron identification, the minimum mass assigned is that of a pion). Figure 19 shows the tracking efficiency, defined as the ratio between the reconstructed tracks and generated primary particles in the simulation, as a function of transverse momentum. While the drop below a transverse momentum of ~ 0.5 GeV/c is caused by energy loss in the detector material, the characteristic shape at larger p_{T} is determined by the loss of clusters in the p_{T}-dependent fraction of the track trajectory projected on the dead zone between readout sectors. The efficiency is almost independent of the occupancy in the detector. Even in the most central Pb–Pb collisions the contamination by tracks with more than 10% wrongly associated clusters does not exceed 3%.

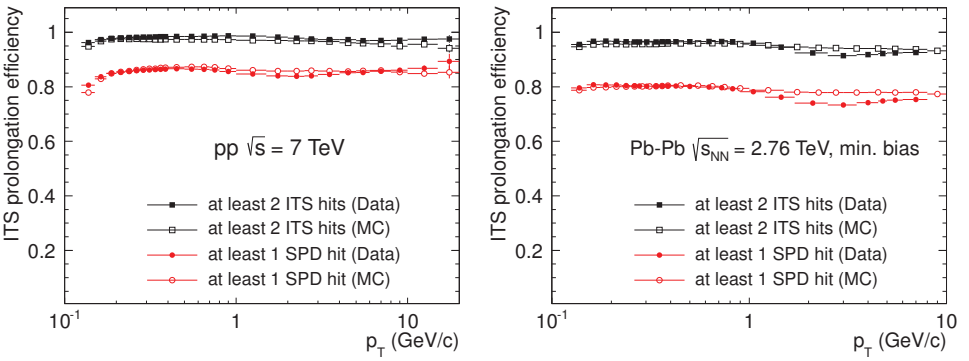

Fig. 20. ITS–TPC matching efficiency versus p_T for data and Monte Carlo for pp (left) and Pb–Pb (right) collisions.

The reconstructed TPC tracks are then propagated to the outermost ITS layer and become the seeds for track finding in the ITS. The seeds are propagated inward and are updated at each ITS layer by all clusters within a proximity cut, which takes into account positions and errors. The result of each update is saved as a new seed. In order to account for the detection inefficiency, seeds without an update at a given layer are also used for further track finding. The χ^2 of such seeds is increased by a penalty factor for a missing cluster (unless the seed extrapolation happened to be in the dead zone of the layer, in which case no cluster should be expected). Thus, each TPC track produces a tree of track hypotheses in the ITS. As is the case in the TPC, this seeding procedure is performed in two passes, with and without vertex constraint. Once the complete tree of prolongation candidates for the TPC track is built, the candidates are sorted according to the reduced χ^2. The candidates with the highest quality from each tree are checked for cluster sharing among each other. If shared clusters are found, an attempt is made to find alternative candidates in the involved trees. In the case of a failure to completely resolve the conflict between two tracks, the worse of the two acquires a special flag for containing potentially incorrectly matched ("fake") clusters. Finally, the highest quality candidate from each hypothesis tree is added to the reconstructed event. Figure 20 shows the TPC track prolongation efficiency to ITS in pp and Pb–Pb collisions as a function of track transverse momentum, with different requirements of ITS layer contributions. The data and Monte Carlo (MC) efficiencies are shown by solid and open symbols, respectively. The fraction of tracks with at least one fake cluster in the ITS in the most central Pb–Pb collisions reaches $\sim 30\%$ at $p_T < 0.2$ GeV/c, decreases to $\sim 7\%$ at 1 GeV/c, and drops below 2% at 10 GeV/c.

As one can see in Fig. 19, the reconstruction efficiency in the TPC sharply drops at low transverse momentum. The cutoff is around 200 MeV/c for pions and 400 MeV/c for protons, and is caused by energy loss and multiple scattering in the detector material. For this reason, a standalone ITS reconstruction is performed with those clusters that were not used in the ITS–TPC tracks. The helical seeds are

built using two clusters from the three innermost ITS layers and the primary vertex point. Each such seed is propagated to the other layers and updated with clusters within a proximity cut. Each matching cluster increments the number of seed-completion hypotheses. For the final step of seed processing, all of the hypotheses are refitted by a Kalman filter and the track with the best fit χ^2 is accepted, with its clusters being removed from further searches. In order to increase the efficiency of tracking, the whole procedure is repeated a few times, gradually opening the seed completion road widths. This algorithm enables the tracking of particles with transverse momenta down to about 80 MeV/c.

Once the reconstruction in the ITS is complete, all tracks are extrapolated to their point of closest approach to the preliminary interaction vertex, and the outward propagation starts. The tracks are refitted by the Kalman filter in the outward direction using the clusters found at the previous stage. At each outward step, the track length integral, as well as the time of flight expected for various particle species $(\mathrm{e}, \mu, \pi, \mathrm{K}, \mathrm{p})$, are updated for subsequent particle identification with TOF (see Sec. 7). Once the track reaches the TRD ($R = 290$ cm), an attempt is made to match it with a TRD tracklet (track segment within a TRD layer) in each of the six TRD layers. Similarly, the tracks reaching the TOF detector are matched to TOF clusters. The track length integration and time-of-flight calculation are stopped at this stage. The tracks are then propagated further for matching with signals in EMCal, PHOS, and HMPID (see Secs. 7 and 8 for the performance of matching to external detectors). The detectors at a radius larger than that of the TPC are currently not used to update the measured track kinematics, but their information is stored in the track object for the purposes of particle identification.

At the final stage of the track reconstruction, all tracks are propagated inwards starting from the outer radius of the TPC. In each detector (TPC and ITS), the tracks are refitted with the previously found clusters. The track's position, direction, inverse curvature, and its associated covariance matrix are determined.

The majority of tracks reconstructed with the described procedure come from the primary interaction vertex (Fig. 21). Secondary tracks, representing the products of decays and of secondary interactions in the detector material, can be further suppressed by cuts on the longitudinal and transverse distances of closest approach (d_0) to the primary vertex. The dedicated reconstruction of secondary tracks is the subject of Subsec. 6.4.

The left panel of Fig. 22 shows the resolution of the transverse distance to the primary vertex for identified ITS–TPC tracks in pp collisions, compared with simulation. The contribution from the vertex resolution is not subtracted. The right panel of Fig. 22 shows the same quantity for all charged particle tracks for three colliding systems and with a higher p_{T} reach. One can notice an improvement of the resolution in heavier systems thanks to the more precisely determined vertex for higher multiplicities.

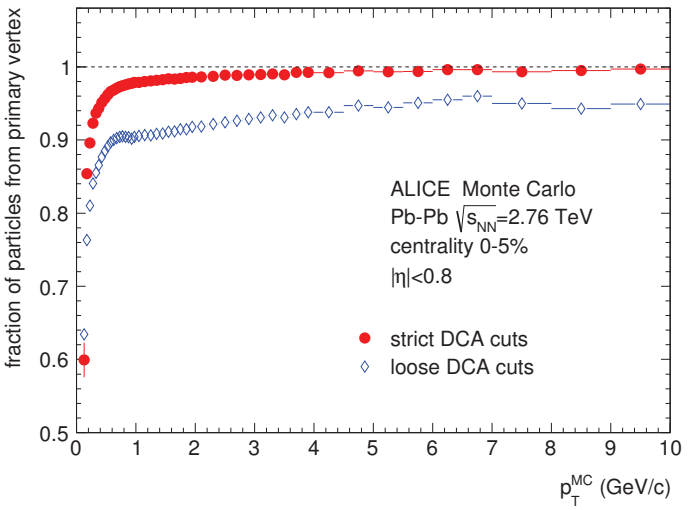

Fig. 21. Fraction of reconstructed tracks coming from the primary interaction vertex. Two sets of cuts on the track distance of closest approach (d_0) to the primary vertex are shown: "loose" with $|d_{0,z}| < 3$ cm, $d_{0,xy} < 3$ cm and "strict" with $|d_{0,z}| < 2$ cm, $d_{0,xy} < (0.0182 + 0.0350\ \text{GeV}/cp_T^{-1})$ cm.

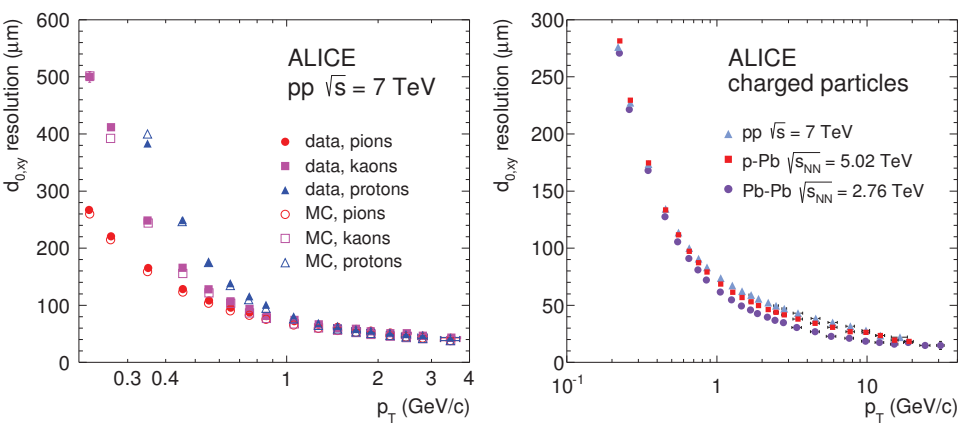

Fig. 22. Resolution of the transverse distance to the primary vertex for identified particle global ITS–TPC tracks (left) and for all charged ITS–TPC tracks (right). The contribution from the vertex resolution is not subtracted.

The transverse momentum resolution for TPC standalone tracks and ITS–TPC combined tracks, extracted from the track covariance matrix, is shown in Fig. 23. The effect of constraining the tracks to the primary vertex is shown as well. The inverse-p_T resolution, plotted in this figure, is connected to the relative transverse momentum resolution via

$$\frac{\sigma_{p_T}}{p_T} = p_T\ \sigma_{1/p_T}\,. \tag{14}$$

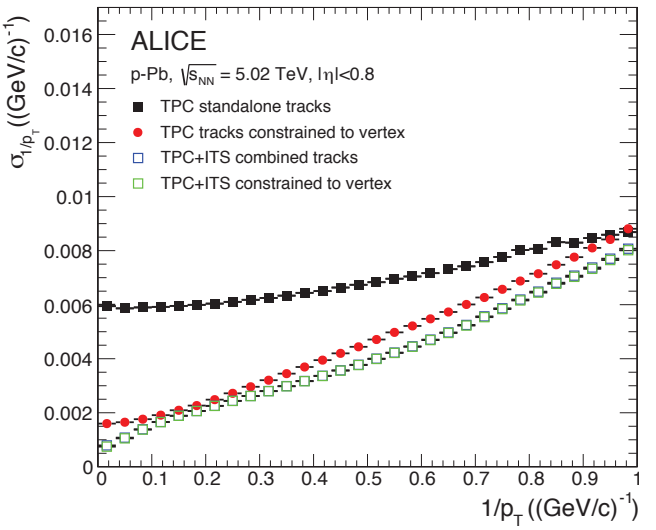

Fig. 23. (Color online) The p_T resolution for standalone TPC and ITS–TPC matched tracks with and without constraint to the vertex. The vertex constrain significantly improves the resolution of TPC standalone tracks. For ITS–TPC tracks, it has no effect (green and blue squares overlap).

The plot represents the most advanced reconstruction scheme that was applied to the data taken in the recent p–Pb run. In central Pb–Pb collisions, the p_T resolution is expected to deteriorate by $\sim$10–15% at high p_T due to the loss (or reduction) of clusters sitting on ion tails, cluster overlap, and fake clusters attached to the tracks.

To demonstrate the mass resolution achievable with ITS–TPC global tracks we show in Fig. 24 the invariant mass spectra of $\mu^+\mu^-$ (left) and e^+e^- (right) pairs measured in ultraperipheral Pb–Pb collisions at $\sqrt{s_{NN}} = 2.76$ TeV. The mass resolution at the J/ψ peak is better than 1%.

Although it provides the best estimate of track parameters, the global ITS–TPC track reconstruction suffers from gaps in the ITS acceptance. In particular, in the innermost two SPD layers, up to 20% and 30% of the modules were inactive in the years 2010 and 2011, respectively. The inefficiency was reduced to $\sim$5% in 2012 after solving problems with detector cooling. For those analyses that require a uniform detector response, the parameters of the tracks fitted only in the TPC and constrained to the primary vertex can be used. The transverse momentum resolution of these tracks is comparable to that of the global tracks up to $p_T \approx 10$ GeV/c and significantly worse for higher momenta (red filled circles in Fig. 23).

The ability to reconstruct pairs of close tracks is important for particle-correlation measurements. The track-separation dependent efficiency has to be either corrected for or, when dealing with ratios, close pairs[g] have to be removed

[g]Two tracks that are so close to each other that the presence of one track affects the reconstruction efficiency of the other.

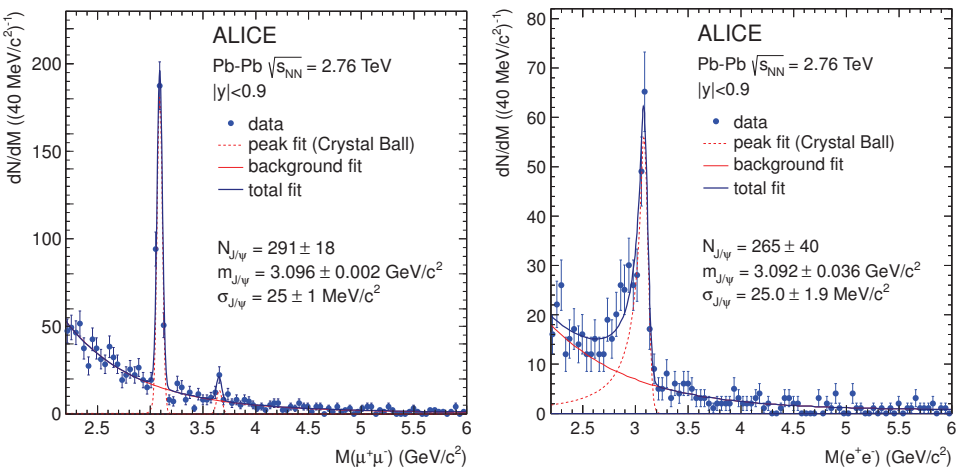

Fig. 24. Invariant mass spectra of $\mu^+\mu^-$ (left) and e^+e^- (right) pairs in ultraperipheral Pb–Pb collisions. The solid and dotted lines represent the background (exponential) and peak (Crystal Ball[50]) fit components, respectively. The bremsstrahlung tail in the e^+e^- spectrum is reproduced in simulation. The mass resolution is better than 1%.

in the numerator and denominator of the correlation function. In the first pion femtoscopy analysis in Pb–Pb collisions,[51] those pairs of tracks that were separated by less than 10 mrad in θ and by less than 2.4 cm in $r\phi$ at a cylindrical radius of $r = 1.2$ m were removed. This was sufficient to determine precisely the shape of the two-particle correlation function.

6.3. *Final determination of the interaction vertex*

Global tracks, reconstructed in TPC and ITS, are used to find the interaction vertex with a higher precision than with SPD tracklets alone. By extrapolating the tracks to the point of closest approach to the nominal beam line and removing far outliers, the approximate point of closest approach of validated tracks is determined. Then the precise vertex fit is performed using track weighting to suppress the contribution of any remaining outliers.[52] In order to improve the transverse vertex position precision in low-multiplicity events, the nominal beam position is added in the fit as an independent measurement with errors corresponding to the transverse size of the luminous region.

For data-taking conditions where a high pileup rate is expected, a more robust version of vertex finding inspired by the algorithm from Ref. 53 is used. It is based on iterative vertex finding and fitting using Tukey bisquare weights[54] to suppress outliers. A scaling factor is applied to the errors on the tracks extrapolated to the nominal beam axis and inflated until at least two tracks with nonzero weights are found for an initial vertex position. The fit, similar to Ref. 52 but accounting for these weights, is performed, and as the fitted vertex moves towards its true position, the scaling factor is decreased. The iterations stop when the distance

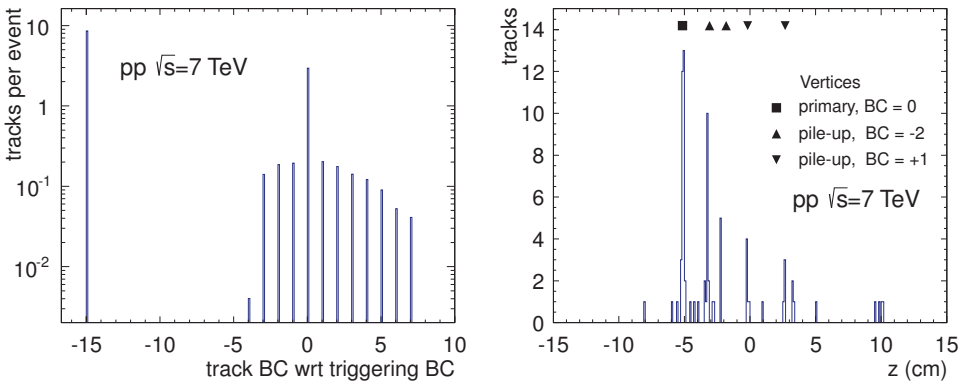

Fig. 25. Left: Bunch crossing (BC) ID of tracks obtained from the comparison of time of flight measured in the TOF detector and expected from the track kinematics. The ID is defined with respect to the BC in which the triggering interaction took place. The peak at −15 corresponds to tracks not matched in TOF (mostly from the pileup in the TPC, outside of the TOF readout window of 500 ns). Right: z coordinates of tracks' PCA to the beam axis in a single event with pileup; the positions of reconstructed vertices with attributed bunch crossings are shown by markers.

between successively fitted vertices is below 10 μm. If the scaling factor at this stage is still significantly larger than unity or the maximum number of iterations is reached, the vertex candidate is abandoned and the search is repeated with a different seeding position. Otherwise the final fit of the weighted tracks is done, the vertex is validated, the tracks with nonzero weights are removed from the pool, and the search for the next vertex in the same event is performed. The algorithm stops when no more vertices are found in the scan along the beam direction. In order to reduce the probability of including tracks from different bunch crossings in the same vertex, only tracks with the same or undefined bunch crossing are allowed to contribute to the same vertex. Tracks are associated with bunch crossings using the time information measured by the TOF detector. The left plot of Fig. 25 shows bunch-crossings assigned to ITS–TPC tracks in a typical high intensity pp run. On the right an example of a single event with identified pileup is shown. The histogram shows the z coordinate of tracks' closest approach to the beam axis, while the positions of reconstructed vertices with attributed bunch crossings are shown by markers.

Figure 26 shows the x (left) and z (right) profiles of the luminous region obtained from reconstructed vertices in pp and Pb–Pb collisions. The transverse resolution of the preliminary interaction vertices found with SPD (Subsec. 6.1) and of the final ones, found with global tracks, are shown in Fig. 27. As expected, both resolutions scale with the square root of the number of contributing tracks.

6.4. *Secondary vertices*

Once the tracks and the interaction vertex have been found in the course of event reconstruction, a search for photon conversions and secondary vertices from particle

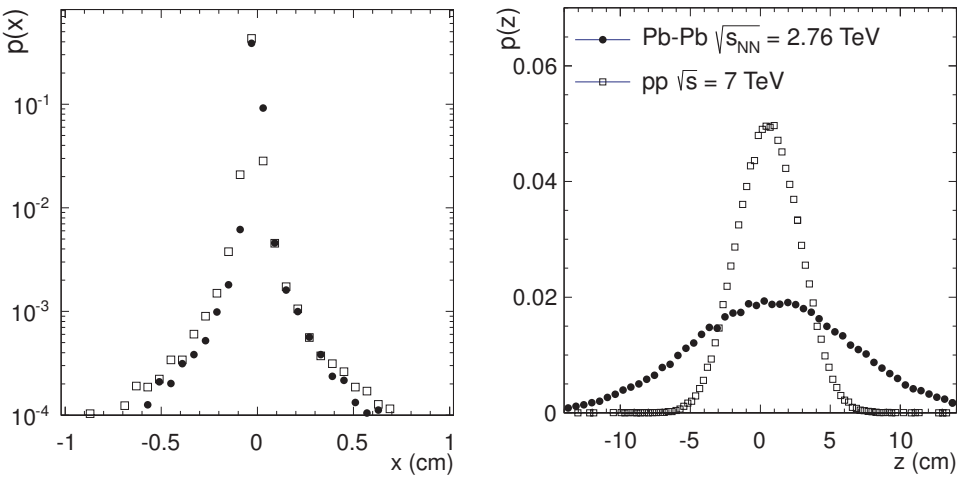

Fig. 26. The x (left) and z (right) projections of the luminous region obtained from reconstructed vertices in pp and Pb–Pb collisions (folded with vertex resolution).

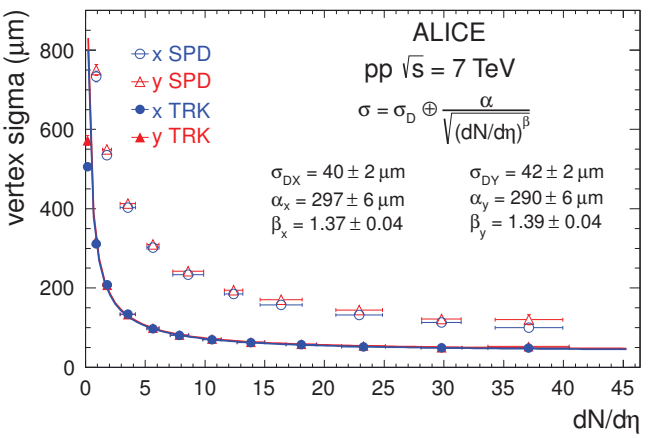

Fig. 27. Transverse width of the final vertex distribution (solid points), decomposed into the finite size of the luminous region σ_D and the vertex resolution $\alpha/\sqrt{(\mathrm{d}N_{\mathrm{ch}}/\mathrm{d}\eta)^{\beta}}$. For comparison, the widths of the preliminary (SPD) interaction vertices are shown as open points.

decays is performed as shown in Fig. 28. Tracks with a distance of closest approach to the interaction vertex exceeding a certain minimum value (0.5 mm in pp and 1 mm in Pb–Pb) are selected. For each unlike-sign pair of such tracks (called V^0 candidate) the point of closest approach between the two tracks is calculated. The V^0 candidates are then subjected to further cuts: (i) the distance between the two tracks at their PCA is requested to be less than 1.5 cm; (ii) the PCA is requested to be closer to the interaction vertex than the innermost hit of either of the two tracks; (iii) the cosine of the angle θ between the total momentum vector of the pair $\vec{p}_{\mathrm{pair}}$ and the straight line connecting the primary (interaction) and secondary

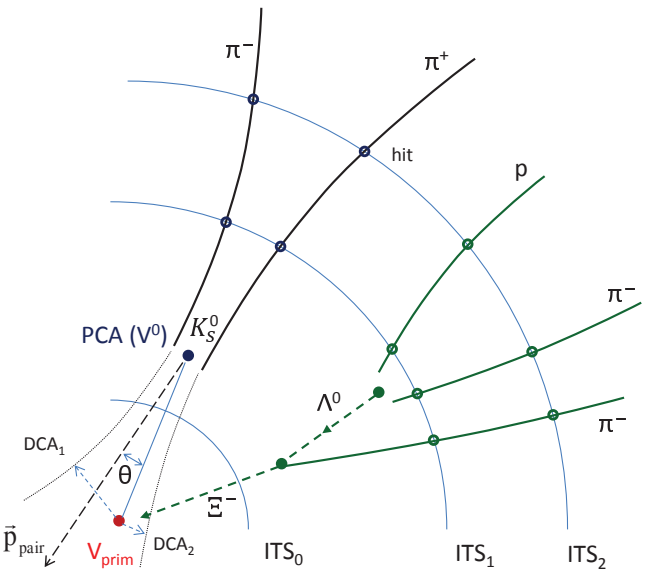

Fig. 28. Secondary vertex reconstruction principle, with K^0_S and Ξ^- decays shown as an example. For clarity, the decay points were placed between the first two ITS layers (radii are not to scale). The solid lines represent the reconstructed charged particle tracks, extrapolated to the secondary vertex candidates. Extrapolations to the primary vertex and auxiliary vectors are shown with dashed lines.

vertices must exceed 0.9. For V^0 candidates with a momentum below 1.5 GeV/c, the latter cut is relaxed. This facilitates the subsequent search for cascade decays.

Figure 29 shows K^0_S (left) and Λ (center) peaks obtained in central Pb–Pb collisions. Proton daughters of Λ with $p_T < 1.5$ GeV/c were identified by their energy loss in the TPC gas (see Sec. 7). The right plot shows the K^0_S and Λ reconstruction efficiencies in central and peripheral collisions as a function of their p_T. The drop in Λ reconstruction efficiency at high p_T is due to the smaller probability of decay in the fiducial volume ($r < 100$ cm) of the V^0 search at higher momenta. The distributions of decay point distances from the interaction vertex agree, after correcting for the acceptance and efficiency, with the expectations based on the known lifetime of the hyperons and neutral kaons (Fig. 30).

After finding V^0 candidates, the search for the cascade (Ξ^-) decays is performed as shown schematically in Fig. 28. V^0 candidates with an invariant mass in the vicinity of the Λ are matched with a secondary track by cutting on their mutual distance at the PCA and requesting that the latter is outside of a cylindrical volume around the interaction vertex ($r > 0.2$ cm).

The reconstruction of more complex secondary vertices is performed later, at the analysis stage. For the study of heavy-flavor decays close to the interaction point, the secondary vertex is searched for by considering all unlike-sign track pairs and selecting those passing a set of topological cuts.[55] In particular,

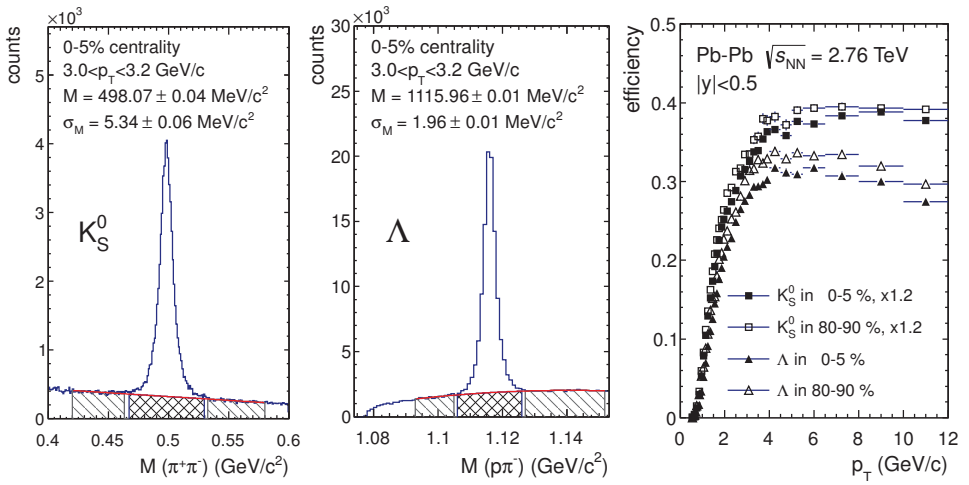

Fig. 29. Invariant mass distributions of $\pi^+\pi^-$ (left panel) and $p\pi^-$ (middle panel) pairs in central Pb–Pb collisions at $\sqrt{s_{NN}} = 2.76$ TeV. The hatched areas show the regions of the K^0_S and Λ peaks and of the combinatorial background. The right-hand panel shows the reconstruction efficiencies (including the candidate selection cuts) as a function of transverse momentum for central (0–5%) and peripheral (80–90%) collisions.

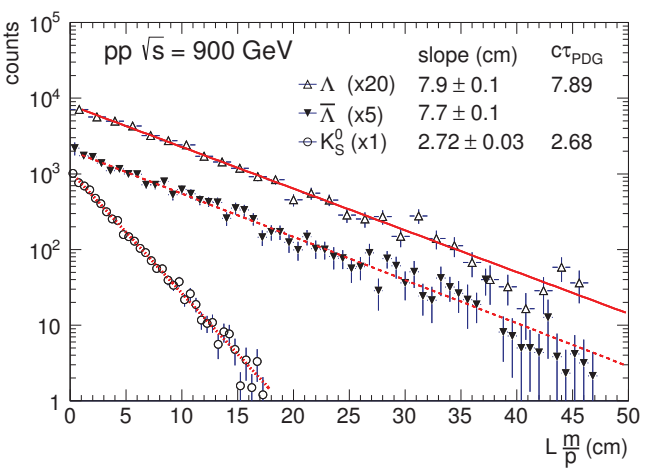

Fig. 30. Distance of the Λ, $\bar{\Lambda}$, and K^0_S decay vertex from the interaction vertex, scaled by p/m. The slopes of the distributions are consistent with the known lifetimes.

the strongest improvement of the signal-to-background ratio is achieved by cuts on the significance of the projection of the decay length in the transverse plane $L_{xy}/\sigma_{L_{xy}} > 7$ and on the transverse pointing angle $\cos(\theta_{xy}) > 0.998$. L_{xy} is defined as $\left(\vec{u}^T S^{-1}\vec{r}\right)/\left(\vec{u}^T S^{-1}\vec{u}\right)$, where $\vec{r}$ is the vector connecting the decay and primary vertices, $\vec{u}$ is the unit vector in direction of the decaying particle, and S^{-1} is the inverse of the sum of the covariance matrices of the primary and secondary vertices.

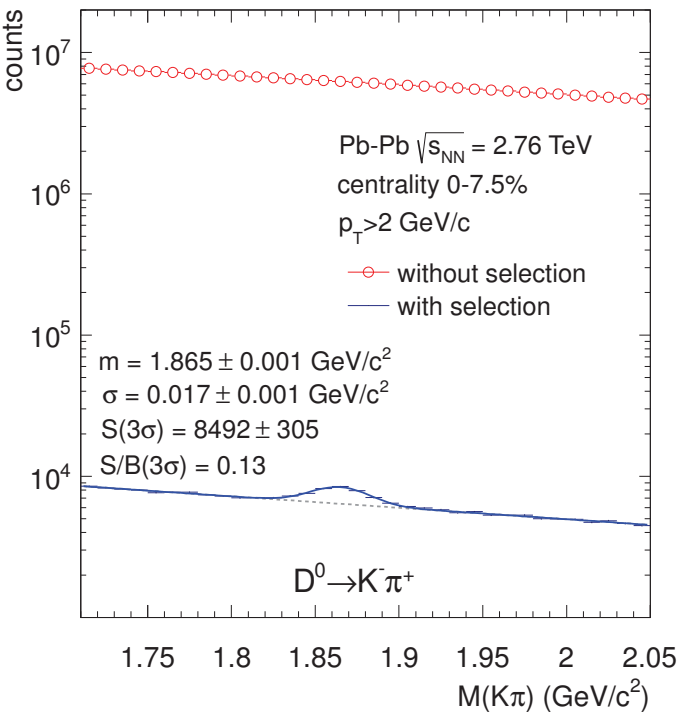

Fig. 31. Invariant mass distribution of $K^-\pi^+$ pairs before (symbols) and after (line) selection cuts on the relation between the secondary (D^0 decay) and primary vertices. The extracted D^0 mass and its resolution as well as the significance are shown after selection.

The effect of the described cuts is illustrated in Fig. 31 which shows the resulting suppression of the combinatorial background in the analysis of $D^0 \to K^-\pi^+$.

The implementation of the geometry and material distribution of the detectors in the simulation and reconstruction software is verified by comparing the distributions of reconstructed hadronic interaction vertices to simulations. The hadronic interaction vertices are found at the analysis level by identifying groups of two or more tracks originating from a common secondary vertex. For these, none of the track pairs should have an invariant mass of γ, K^0_S, or Λ. Figure 32 shows the r–z distribution of such vertices representing the material of the apparatus.

7. Hadron Identification

The ALICE detector has a number of different subsystems for identifying charged hadrons and electrons. The following subsystems are used for hadron identification:

- *ITS*: The outer four layers of the Inner Tracking System have an analog readout to measure the deposited charge, thereby providing a $\mathrm{d}E/\mathrm{d}x$ measurement. This is mainly useful for low-p_T tracks ($p_\mathrm{T} \lesssim 0.7$ GeV/c), specifically at very low p_T, where the ITS is used for standalone tracking.

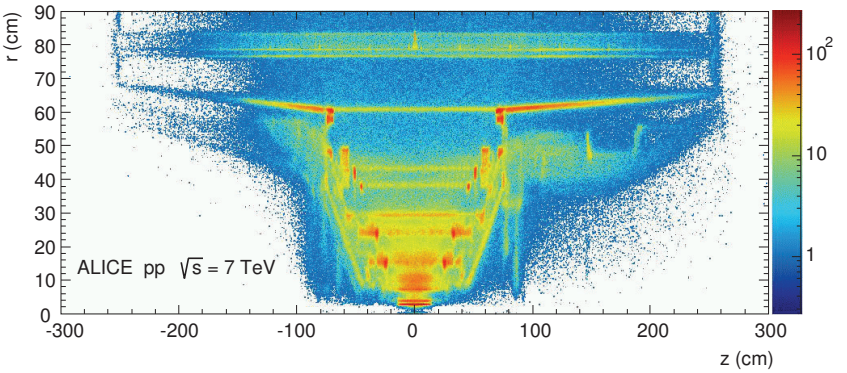

Fig. 32. Distribution of secondary vertices from hadronic interactions in the ALICE material. The ITS layers ($r < 50$ cm), the inner TPC containment vessel (60 cm $< r <$ 70 cm), and the inner TPC field cage ($r \sim 80$ cm) are visible.

- *TPC*: The Time Projection Chamber measures the charge deposited on up to 159 padrows. A truncated mean $\mathrm{d}E/\mathrm{d}x$ (40% highest-charge clusters discarded) is calculated and used for a wide range of momenta. The largest separation is achieved at low p_{T} ($p_{\mathrm{T}} \lesssim 0.7$ GeV/c) but a good separation is also present in the relativistic rise region ($p_{\mathrm{T}} \gtrsim 2$ GeV/c) up to ~ 20 GeV/c.
- *TOF*: The Time-Of-Flight detector is a dedicated detector for particle identification that measures the arrival time of particles with a resolution of ~ 80 ps. This provides a good separation of kaons and protons up to $p_{\mathrm{T}} \simeq 4$ GeV/c.
- *HMPID*: The High Momentum Particle Identification Detector is a ring-imaging Cherenkov detector that covers $|\eta| < 0.6$ in pseudorapidity and 57.6° in azimuth, corresponding to 5% acceptance of the central barrel, and provides proton/kaon separation up to $p_{\mathrm{T}} \simeq 5$ GeV/c.

The measurements in the different particle identification detector systems are then combined to further improve the separation between particle species. This is discussed in Subsecs. 7.5 and 7.7.

The particle identification (PID) capabilities of these detectors are used for a wide range of physics analyses, including transverse momentum spectra for pions, kaons, and protons;[56–58] heavy-flavor decays;[55] Bose–Einstein correlations for pions[51,59,60] and kaons;[61,62] and resonance studies.[63] The hadron identification systems is also used to identify electrons. In addition, the calorimeters (PHOS and EMCal) and the Transition Radiation Detector (TRD) provide dedicated electron identification, which will be discussed in Sec. 8.

7.1. *Particle identification in the ITS*

The inner tracking system (ITS) of ALICE consists of six layers of silicon detectors. The outer four layers provide a measurement of the ionization energy loss of particles as they pass through the detector. The measured cluster charge is normalized to

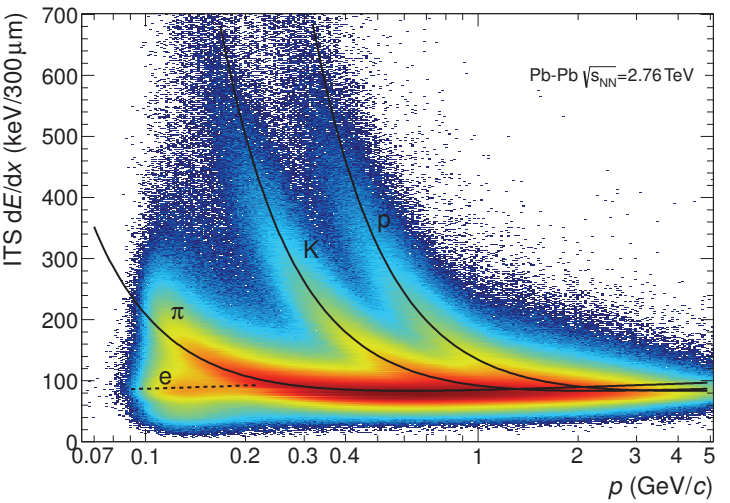

Fig. 33. Distribution of the energy-loss signal in the ITS as a function of momentum. Both the energy loss and momentum were measured by the ITS alone.

the path length, which is calculated from the reconstructed track parameters to obtain a $\mathrm{d}E/\mathrm{d}x$ value for each layer. For each track, the $\mathrm{d}E/\mathrm{d}x$ is calculated using a truncated mean: the average of the lowest two points if four points are measured, or a weighted sum of the lowest (weight 1) and the second-lowest points (weight 1/2), if only three points are measured. An example distribution of measured truncated mean energy loss values as a function of momentum in the ITS is shown in Fig. 33.

7.2. *Particle identification in the TPC*

The TPC[64] is the main tracking detector in ALICE. In addition it provides information for particle identification over a wide momentum range. Particle identification is performed by simultaneously measuring the specific energy loss ($\mathrm{d}E/\mathrm{d}x$), charge, and momentum of each particle traversing the detector gas. The energy loss, described by the Bethe-Bloch formula, is parametrized by a function originally proposed by the ALEPH collaboration,[65]

$$f(\beta\gamma) = \frac{P_1}{\beta^{P_4}}\left(P_2 - \beta^{P_4} - \ln\left(P_3 + \frac{1}{(\beta\gamma)^{P_5}}\right)\right), \tag{15}$$

where β is the particle velocity, γ is the Lorentz factor, and P_{1-5} are fit parameters. Figure 34 shows the measured $\mathrm{d}E/\mathrm{d}x$ versus particle momentum in the TPC, demonstrating the clear separation between the different particle species. The lines correspond to the parametrization. While at low momenta ($p \lesssim 1$ GeV/c) particles can be identified on a track-by-track basis, at higher momenta particles can still be separated on a statistical basis via multi-Gaussian fits. Indeed, with long tracks ($\gtrsim 130$ samples) and with the truncated-mean method the resulting $\mathrm{d}E/\mathrm{d}x$ peak shape is Gaussian down to at least 3 orders of magnitude.

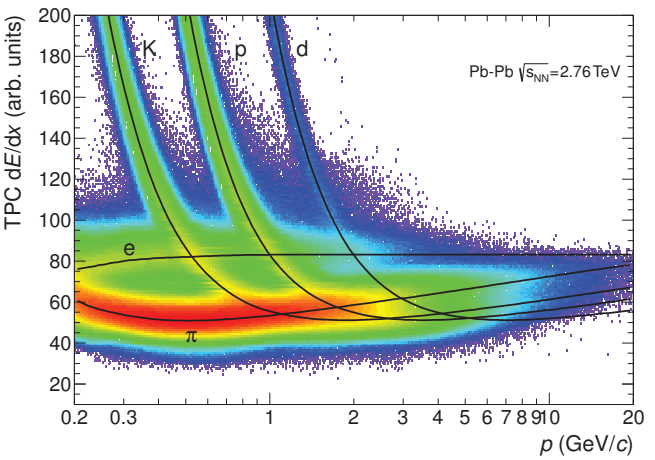

Fig. 34. Specific energy loss ($\mathrm{d}E/\mathrm{d}x$) in the TPC versus particle momentum in Pb–Pb collisions at $\sqrt{s_{\mathrm{NN}}} = 2.76$ TeV. The lines show the parametrizations of the expected mean energy loss.

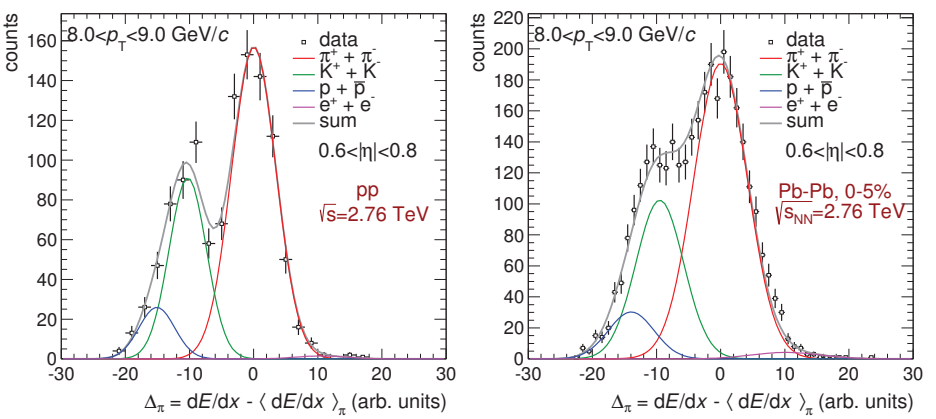

Fig. 35. Ionization energy loss ($\mathrm{d}E/\mathrm{d}x$) distributions in the TPC in pp (left) and Pb–Pb collisions (right) at $\sqrt{s_{\mathrm{NN}}} = 2.76$ TeV. The lines represent Gaussian fits as described in the main text.

In the relativistic rise region, the $\mathrm{d}E/\mathrm{d}x$ exhibits a nearly constant separation for the different particle species over a wide momentum range. Due to a $\mathrm{d}E/\mathrm{d}x$ resolution of about 5.2% in pp collisions and 6.5% in the 0–5% most central Pb–Pb collisions,[h] particle ratios can be measured at a p_{T} of up to 20 GeV/c.[66] The main limitation at the moment is statistical precision, so it is expected that the measurement can be extended up to ~ 50 GeV/c in the future.

As an example, $\mathrm{d}E/\mathrm{d}x$ distributions for charged particles with $p_{\mathrm{T}} \approx 10$ GeV/c are shown in Fig. 35 for pp and the 0–5% most central Pb–Pb collisions. Note that,

[h]The deterioration of the energy-loss resolution in high-multiplicity events is caused by clusters overlapping in z and/or sitting on top of a signal tail from an earlier cluster.

for this analysis, a specific η range was selected in order to achieve the best possible $\mathrm{d}E/\mathrm{d}x$ resolution. The curves show Gaussian fits where the mean and width were fixed to the values obtained using clean samples of identified pions and protons from, respectively, K^0_S and Λ decays, and assuming that the $\mathrm{d}E/\mathrm{d}x$ response at high p_T depends only on $\beta\gamma$.

7.3. *Particle identification in TOF*

The Time-Of-Flight (TOF) detector[67] of ALICE is a large area array of Multigap Resistive Plate Chambers (MRPC), positioned at 370–399 cm from the beam axis and covering the full azimuth and the pseudorapidity range $|\eta| < 0.9$. In Pb–Pb collisions, in the centrality range 0–70% the overall TOF resolution is 80 ps for pions with a momentum around 1 GeV/c. This value includes the intrinsic detector resolution, the contribution from electronics and calibration, the uncertainty on the start time of the event, and the tracking and momentum resolution.[68] TOF provides PID in the intermediate momentum range, up to 2.5 GeV/c for pions and kaons, and up to 4 GeV/c for protons.

The start time for the TOF measurement is provided by the T0 detector, which consists of two arrays of Cherenkov counters T0C and T0A, positioned at opposite sides of the interaction point (IP) at $-3.28 < \eta < -2.97$ and $4.61 < \eta < 4.92$, respectively. Each array has 12 cylindrical counters equipped with a quartz radiator and photomultiplier tube.[69] Figure 36 (left panel) shows the distribution of the start time (interaction time of the collision) as measured by the sum of the time signals from the T0A and T0C detectors in Pb–Pb collisions at $\sqrt{s_{NN}} = 2.76$ TeV with respect to the nominal LHC clock value. The width of the distribution is indicative of how much the collision time can jitter with respect to its nominal value (the LHC clock edge). This is due to the finite size of the bunches and the clock-phase shift during a fill. The time resolution of the detector, estimated by the time difference registered in T0A and T0C, is 20–25 ps in Pb–Pb collisions (Fig. 36, right panel) and ~ 40 ps in pp collisions. The efficiency of T0 is 100% for the 60% most central Pb–Pb collisions at $\sqrt{s_{NN}} = 2.76$ TeV, dropping to about 50% for events with centrality around 90%. For pp collisions at $\sqrt{s} = 7$ TeV, the efficiency is about 50% for a T0 coincidence signal (T0A-AND-T0C) and 70% if only one of the T0 detectors is requested (T0A-OR-T0C).

The start time of the event t_{ev} is also estimated using the particle arrival times at the TOF detector. A combinatorial algorithm based on a χ^2 minimization between all the possible mass hypotheses is used in the latter case. It can be invoked when at least three particles reach the TOF detector, to provide increased resolution and efficiency at larger multiplicity. With 30 tracks, the resolution on t_{ev} reaches 30 ps.[68] This method is particularly useful for events in which the T0 signal is not present. If neither of these two methods is available, an average TOF start time for the run is used instead.

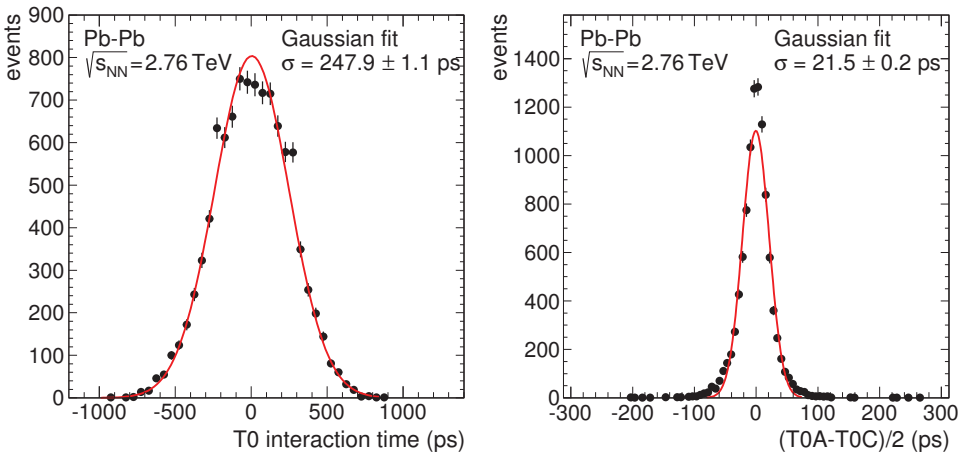

Fig. 36. Interaction time of the collision with respect to the LHC clock measured by the T0 detector (left) and the resolution of the system obtained as the time difference between T0A and T0C (right). The time difference is corrected for the longitudinal event-vertex position as measured by the SPD.

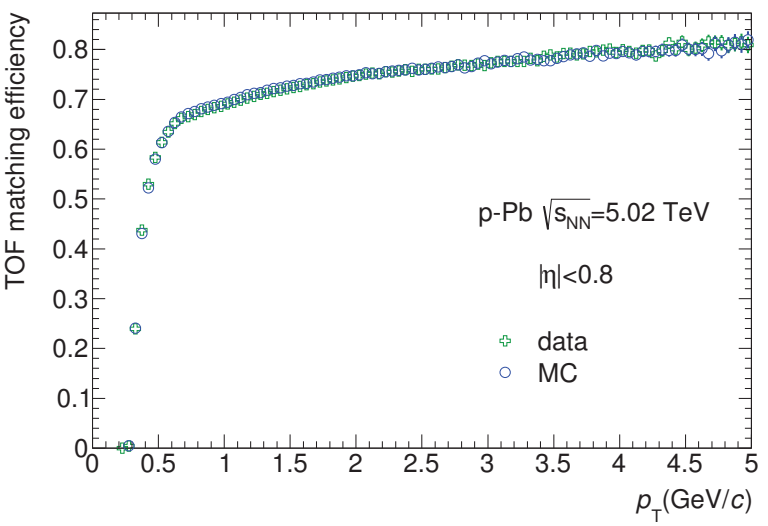

Fig. 37. Matching efficiency (including the geometric acceptance factor) at TOF for tracks reconstructed in the TPC in p–Pb collisions at $\sqrt{s_{\rm NN}} = 5.02$ TeV, compared to Monte Carlo simulation.

The efficiency of matching TPC tracks to TOF in the 2013 p–Pb run is compared with Monte Carlo simulation in Fig. 37. At $p_{\rm T} < 0.7$ GeV/c, the matching efficiency is dominated by energy loss and the rigidity cutoff generated by the magnetic field. At higher transverse momenta it reflects the geometrical acceptance (dead space between sectors), the inactive modules, and the finite efficiency of the MRPCs (98.5% on average).

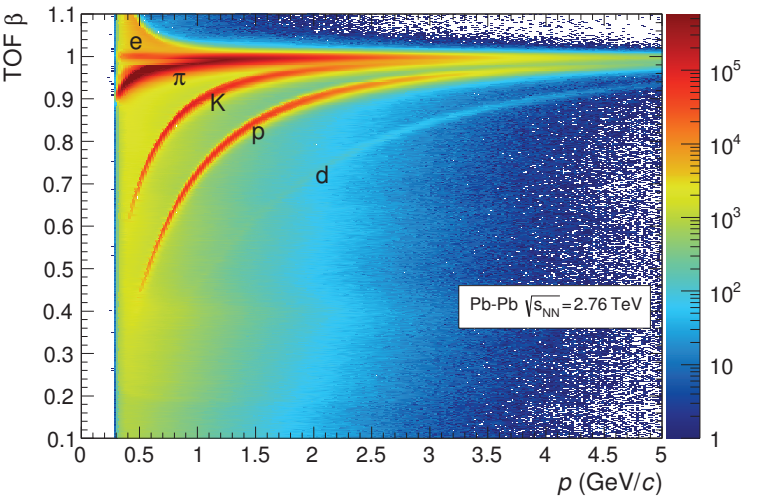

Fig. 38. Distribution of β as measured by the TOF detector as a function of momentum for particles reaching the TOF in Pb–Pb interactions.

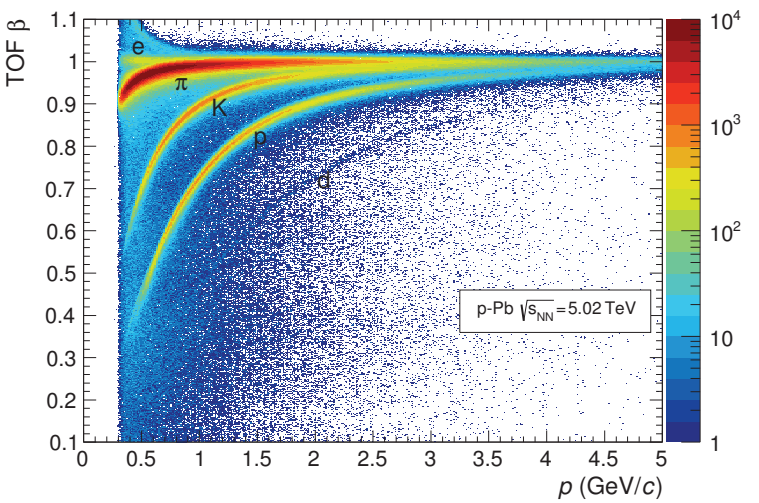

Fig. 39. Distribution of β as measured by the TOF detector as a function of momentum for particles reaching TOF in p–Pb interactions. The background of mismatched tracks is lower than in Pb–Pb.

Figure 38 illustrates the performance of the TOF detector by showing the measured velocity β distribution as a function of momentum (measured by the TPC). The background is due to tracks that are incorrectly matched to TOF hits in high-multiplicity Pb–Pb collisions. The distribution is cleaner in p–Pb collisions (Fig. 39), showing that the background is not related to the resolution of the TOF detector, but is rather an effect of track density and the fraction of mismatched

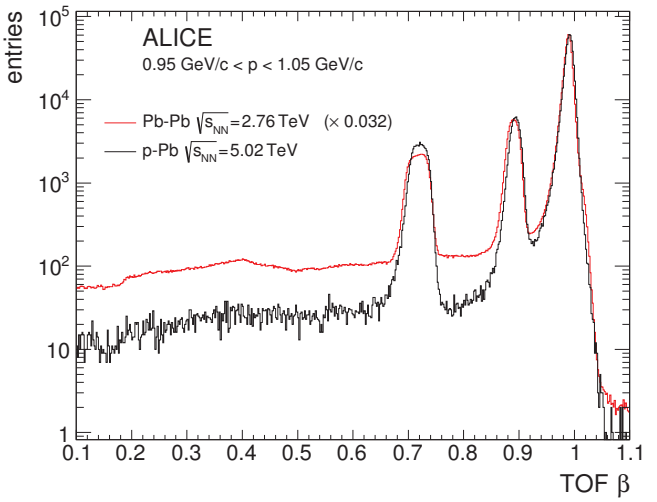

Fig. 40. TOF β distribution for tracks with momentum 0.95 GeV/c < p < 1.05 GeV/c. The Pb–Pb histogram is normalized to the p–Pb one at the pion peak ($\beta = 0.99$). While the resolution (width of the mass peaks) is the same, the background of mismatched tracks increases in the high-multiplicity environment of Pb–Pb collisions. Both samples are minimum bias.

tracks. This is also visible in Fig. 40 where the β distribution is shown for a narrow momentum band. The pion, kaon, and proton peaks are nearly unchanged but the level of background due to mismatched tracks is higher in Pb–Pb. The fraction of mismatched tracks above 1 GeV/c in Pb–Pb events is closely related to the TOF occupancy. With 10^4 hits at TOF (corresponding to a very central Pb–Pb event) the TOF pad occupancy is 6.7% and the fraction of mismatched hits is around 6.5%.

The resolution can be studied in a given narrow momentum interval by computing the difference between the time of flight measured by TOF and the pion time expectation. The distribution is fitted with a Gaussian whose width is the convolution of the intrinsic time resolution of the TOF detector and the resolution of the event time. In the limit of high track multiplicity the width becomes equal to the intrinsic resolution of the TOF detector and has a value of 80 ps (Fig. 41).

At those transverse momenta where the TOF resolution does not permit track-by-track identification, a fit of multiple Gaussian peaks is used to determine the particle yields. To illustrate this, Fig. 42 shows, for tracks with $1.5 < p_{\mathrm{T}} < 1.6$ GeV/c, the difference between the measured time of flight and the expectation for kaons, together with a template fit to the pion, kaon, and proton peaks and the combinatorial background from mismatched tracks.

7.4. *Particle identification in the HMPID*

The High Momentum Particle Identification Detector consists of seven identical RICH (ring-imaging Cherenkov) modules in proximity focusing configuration, exploiting a liquid C_6F_{14} radiator coupled to MWPC (multiwire proportional

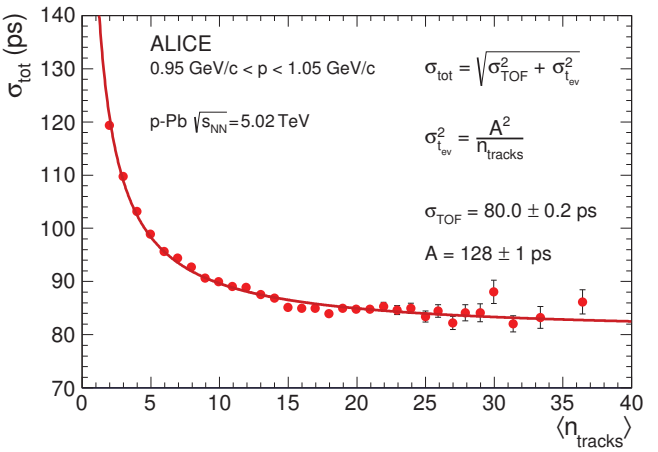

Fig. 41. Time resolution of pion tracks with $0.95 < p < 1.05$ GeV/c as a function of the number of tracks used to define the start time of the collision $t_{\rm ev}$.[68] The data are from p–Pb collisions.

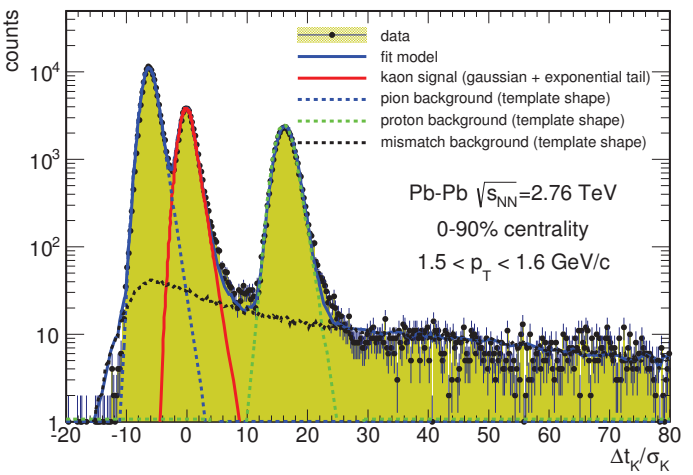

Fig. 42. TOF measured in Pb–Pb collisions at $\sqrt{s_{\rm NN}} = 2.76$ TeV. The expected time of flight for kaons is subtracted and the result is divided by the expected resolution.

chamber)-based photon detectors with CsI photocathodes and covering 11 m^2 ($\approx 5\%$ of TPC acceptance). On average 14 photoelectrons per ring are detected at saturation ($\beta \approx 1$). The HMPID detector extends track-by-track charged hadron identification in ALICE to higher $p_{\rm T}$. The identification is based on the Cherenkov angle of the ring produced by charged tracks. The Cherenkov angle is given by:

$$\cos\theta = \frac{1}{n\beta}\,, \tag{16}$$

where n is the refractive index of the radiator ($n \approx 1.289$ at 175 nm). The matching efficiency of tracks reconstructed in the TPC with the HMPID is shown in

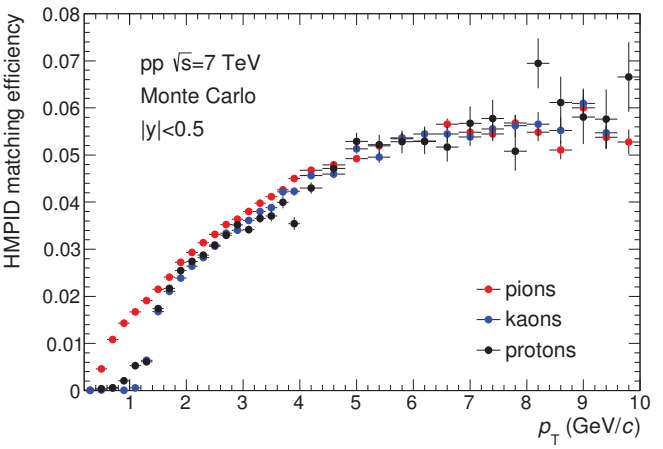

Fig. 43. Matching efficiency (including the geometric acceptance factor) at HMPID for tracks reconstructed in the TPC.

Fig. 43 for pp data and positive particles. The value at large transverse momentum is dominated by the geometrical acceptance of the detector. At low p_T, the matching efficiency is shaped by energy loss, a lower momentum cut due to the magnetic field, and the mass-dependent momentum threshold of the Cherenkov effect. Negative particles (not shown) have similar behavior. Antiprotons have a slightly lower efficiency due to differing absorption behavior in the material between TPC and HMPID.

Figure 44 shows the measured mean Cherenkov angle as a function of track momentum for pions, kaons, and protons in pp collisions at 7 TeV. The lines represent parametrizations of Eq. (16) for each species. The separation of kaons from

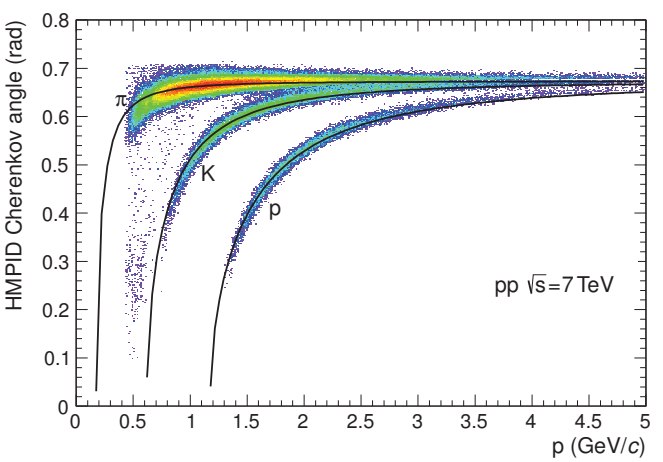

Fig. 44. Mean Cherenkov angle measured by HMPID in pp collisions at 7 TeV as a function of track momentum. The lines represent parametrizations of Eq. (16) for each species.

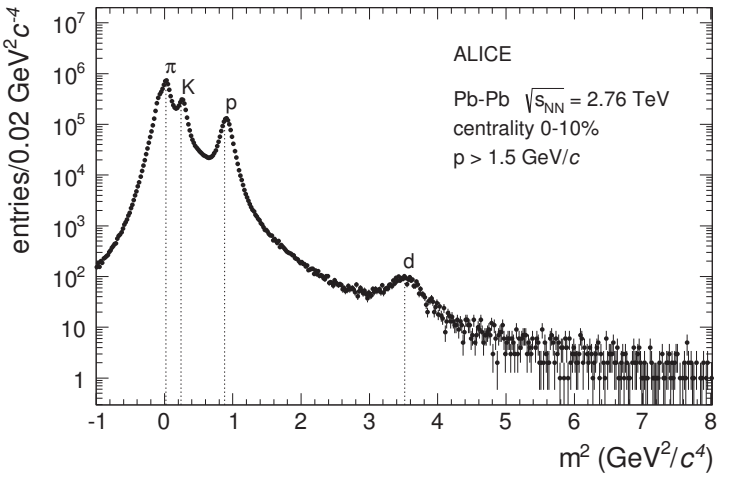

Fig. 45. Squared particle masses calculated from the momentum and velocity determined with ITS-TPC and HMPID, respectively, in central Pb–Pb collisions at $\sqrt{s_{\rm NN}} = 2.76$ TeV. The velocity is calculated from the Cherenkov angle measured in the HMPID. Dotted lines indicate the PDG mass values. The pion tail on the left-hand side is suppressed by an upper cut on the Cherenkov angle. The deuteron peak is clearly visible.

other charged particles, determined by fitting the Cherenkov angle distribution with three Gaussians for each transverse momentum bin (the background is negligible), is 3σ for $p_{\rm T} < 3$ GeV/c for pions, and $p_{\rm T} < 5$ GeV/c for protons.

Figure 45 shows the mass distribution of particles identified in the HMPID in central Pb–Pb collisions. The mass is calculated from the Cherenkov angle measured in the HMPID and the momentum determined by the central-barrel tracking detectors. For tracks with $p > 1.5$ GeV/c and with 5–15 clusters per ring, the deuteron peak becomes clearly visible. This, and the fact that all of the particle peaks are at their nominal mass values, shows the good performance of the pattern recognition in the high-multiplicity environment of central Pb–Pb collisions.

7.5. *Overview of separation powers and combined PID*

Figure 46 shows the pion–kaon (left panel) and kaon–proton (right panel) separation power of the ITS, TPC, TOF, and HMPID as a function of $p_{\rm T}$. The separation is calculated as the distance Δ between the peaks divided by the Gaussian width σ of the pion and the kaon response, respectively. Note that the detector response for the individual detectors in Figs. 33, 34, 38, 39, and 44 is naturally a function of total momentum p. However, since most physics results are analyzed in transverse momentum bins, in Fig. 46 we present the separation power in $p_{\rm T}$ bins, averaging the momentum-dependent response over the range $|\eta| < 0.5$. For the TPC, a forward pseudorapidity slice, relevant for high-$p_{\rm T}$ PID analysis, is shown as well. This also demonstrates the effect of averaging over a larger η range, which mixes different momentum slices.

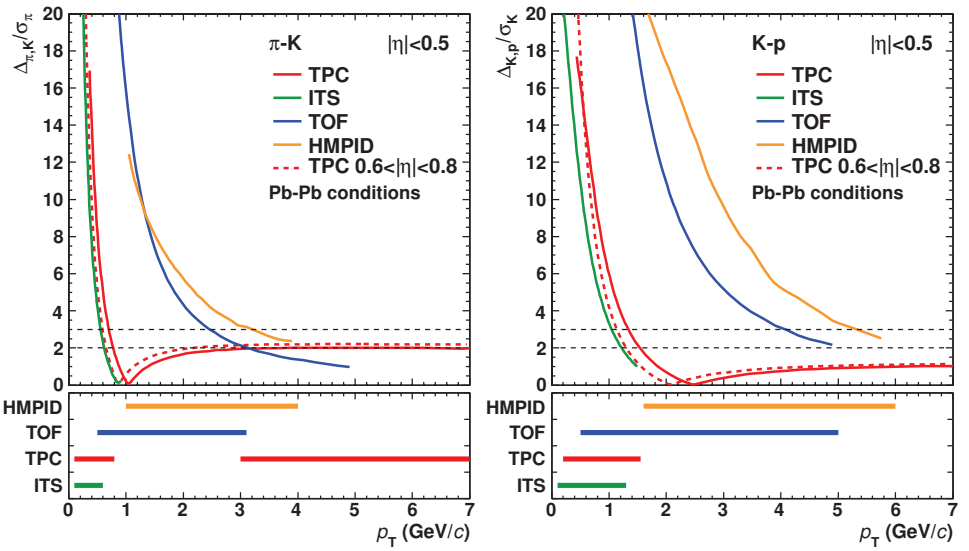

Fig. 46. Separation power of hadron identification in the ITS, TPC, TOF, and HMPID as a function of p_{T} at midrapidity. The left (right) panel shows the separation of pions and kaons (kaons and protons), expressed as the distance between the peaks divided by the resolution for the pion and the kaon, respectively, averaged over $|\eta| < 0.5$. For the TPC, an additional curve is shown in a narrower η region. The lower panels show the range over which the different ALICE detector systems have a separation power of more than 2σ.

The plots demonstrate the complementarity of the different detector systems. At low $p_{\mathrm{T}} < 500$ MeV/c, the TPC and ITS provide the main separation, because TOF and HMPID are not efficient. At intermediate p_{T}, up to 3 (4) GeV/c for pions/kaons and 5 (6) GeV/c for protons, TOF(HMPID) provides more than 3σ separation power. TOF has full azimuthal coverage and it reaches lower p_{T}, while HMPID only covers 5% of the full acceptance. At higher p_{T}, the TPC can be used to separate pions from protons and kaons with $\sim 2\sigma$ separation, exploiting the relativistic rise of the energy loss. Protons and kaons can be separated statistically with a multi-Gaussian fit to the collected signal (see Fig. 35).

The separation of hadron species can be further improved by combining information from multiple detectors, thus allowing a further extension of the momentum range for identified particle measurements. An example of this approach is shown in Fig. 47, where at intermediate p_{T} the difference between the measured and expected PID signals for TPC and TOF are represented. It is evident that cuts or fits using a combination of the variables provide a better separation than just considering their projections. This technique was used to measure the p/π ratio in di-hadron correlations[70] and permits, using fits of the bidimensional distribution, to extend the kaon/pion separation up to a transverse momentum of 5 GeV/c in Pb–Pb.

A Bayesian approach to combined PID, making use of the known relative yields of different particle species, is under development.

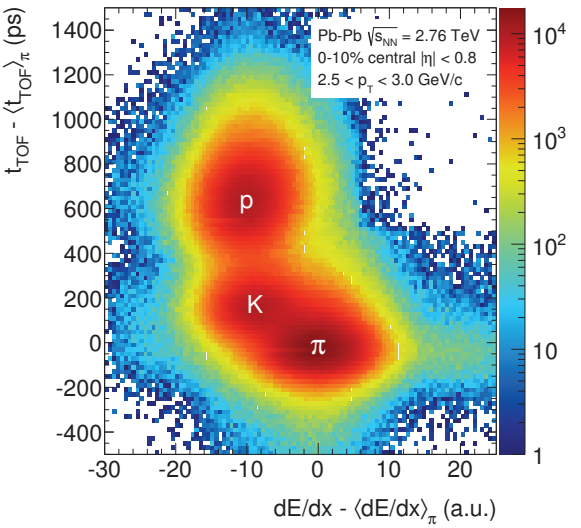

Fig. 47. Combined pion identification with TOF and with $\mathrm{d}E/\mathrm{d}x$ in the TPC.

7.6. *Particle identification using weak decay topology*

In addition to the direct identification of the more stable hadrons $(\pi, \mathrm{K}, \mathrm{p})$ using mass-dependent signals such as $\mathrm{d}E/\mathrm{d}x$, TOF and Cherenkov radiation, ALICE also identifies hadrons through their weak decay topology. This technique is used for strange hadrons, such as K^0_S, Λ, and the multi-strange baryons Ξ and Ω, as well as for charmed hadrons. In all of these cases a full kinematical reconstruction of the decay into charged hadrons is used, as described in Subsec. 6.4.

In addition to these, charged kaons can be identified by a distinct kink in the track owing to the decay into a muon and a neutrino with a branching ratio (BR) of 63.5%. Figure 48 shows an invariant mass distribution of kink-decay daughters, assumed to be a muon and a neutrino. The muon momentum is taken from the track segment after the kink. For the neutrino momentum, the difference between the momenta of the track segments before and after the kink is used. The distribution shows two peaks representing the muonic decays of pions and kaons, as well as $\mathrm{K}^\pm \to \pi^\pm + \pi^0$ (BR = 20.7%) reconstructed with an incorrect mass assumption. The broad structure outside the pion mass region mainly originates from three-body decays of kaons. The efficiency for reconstruction and identification of charged kaons is $\sim 60\%$ at p_T around 1.0 GeV/c and decreases gradually at higher transverse momenta, as the angle between mother and daughter tracks becomes smaller. The structures in the invariant mass distribution are well reproduced in simulation. The simulation also provides an estimate of the contamination. For kaons with transverse momenta up to 8 GeV/c, the contamination is below 3%. Most of the contamination arises due to single charged-particle tracks with a small-angle kink caused by scattering rather than a decay.

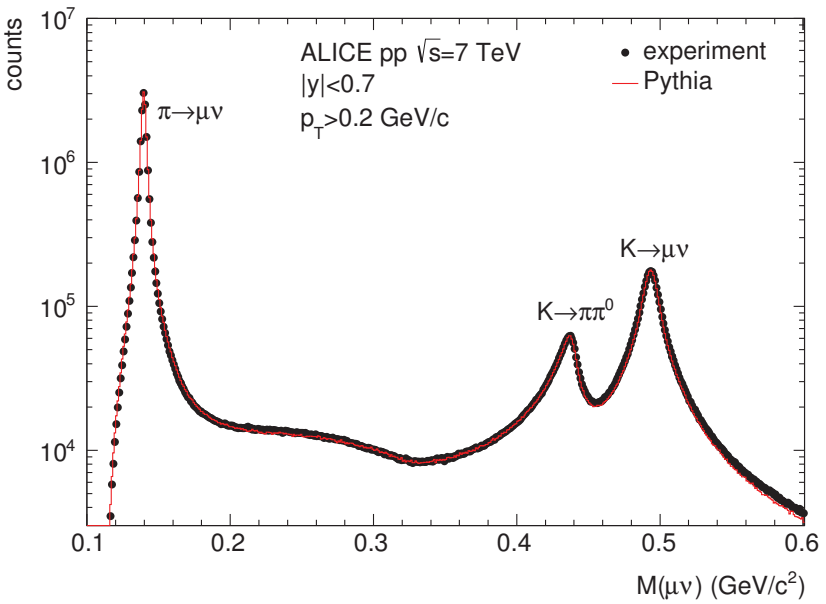

Fig. 48. Invariant mass of reconstructed charged particles (pions and kaons) decaying inside the TPC volume and producing a secondary vertex (kink). The mass is calculated assuming that the track segment after the kink represents a muon and that the neutral decay daughter is a neutrino. The neutrino momentum is taken from the difference between the momenta of the track segments before and after the kink.

7.7. *Particle identification in physics analysis*

The use and performance of particle identification can best be illustrated using examples of specific physics analyses. Transverse momentum spectra of π, K, and p, identified using ITS, TPC, TOF, and decay topology, were published for pp[56] and Pb–Pb[57,58] collisions. Applications of PID techniques to analyses of ϕ, D, and light nuclei are briefly discussed below.

7.7.1. *ϕ meson*

The ϕ meson predominantly decays into two charged kaons $\phi \rightarrow \mathrm{K}^{+}\mathrm{K}^{-}$. Since this is a strong decay, it is not possible to topologically reconstruct the decay. Identification of the decay products, however, dramatically improves the signal-to-background ratio. This is demonstrated in Fig. 49, which shows the ϕ signal in 3 million central Pb–Pb events without particle identification (green circles) and with particle identification using a 2σ cut on the TPC $\mathrm{d}E/\mathrm{d}x$ (red dots). The signal-to-background ratio at the ϕ peak for $1 < p_{\mathrm{T}} < 1.5$ GeV/c ($p_{\mathrm{T}} < 24$ GeV/c) improves from 0.3×10^{-3} (0.1×10^{-3}) to 5×10^{-3} (4×10^{-3}) when the PID cut is applied. In terms of the peak significance, the improvement is from 14 to 45 (from 15 to 75).

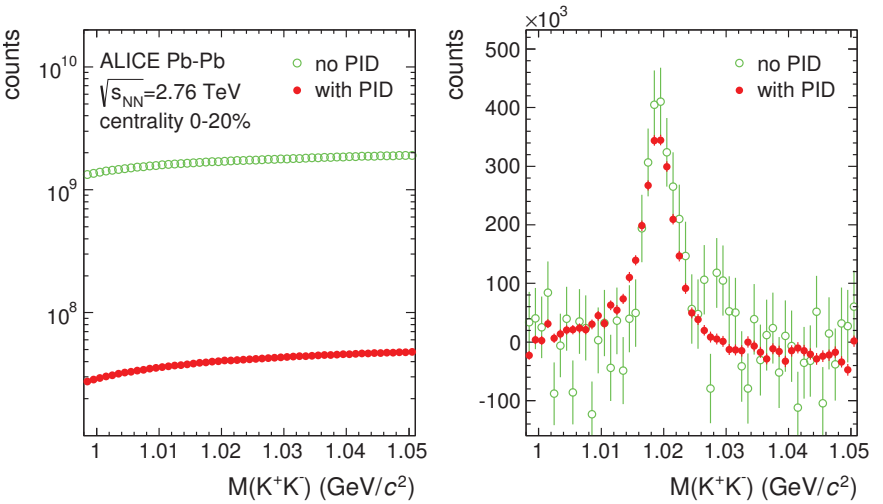

Fig. 49. (Color online) Invariant mass distribution of K^+K^- candidate pairs for reconstruction of the $\phi \to$ KK decay, with and without particle identification, before (left panel) and after (right panel) background subtraction.

7.7.2. D *meson*

Charm production measurements in ALICE are performed, among others, using hadronic decays of the charmed mesons D^0, $D^{\pm}$, and $D^{*\pm}$.[55,71,72] For these analyses, the identification of the kaons greatly enhances the signal significance. As an example, Fig. 50 shows the invariant mass distribution of Kπ candidate pairs with

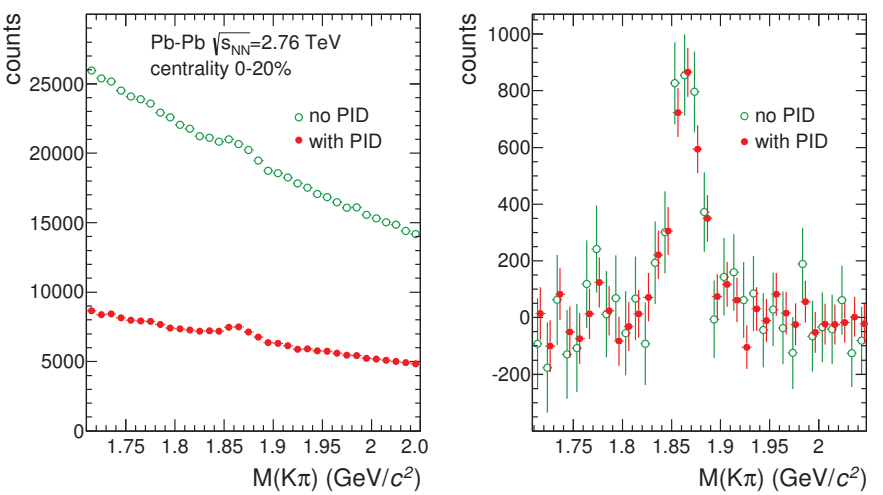

Fig. 50. Invariant mass distribution of Kπ candidate pairs for reconstruction of the $D^0 \to$ Kπ decay, with and without particle identification, before (left panel) and after (right panel) background subtraction.

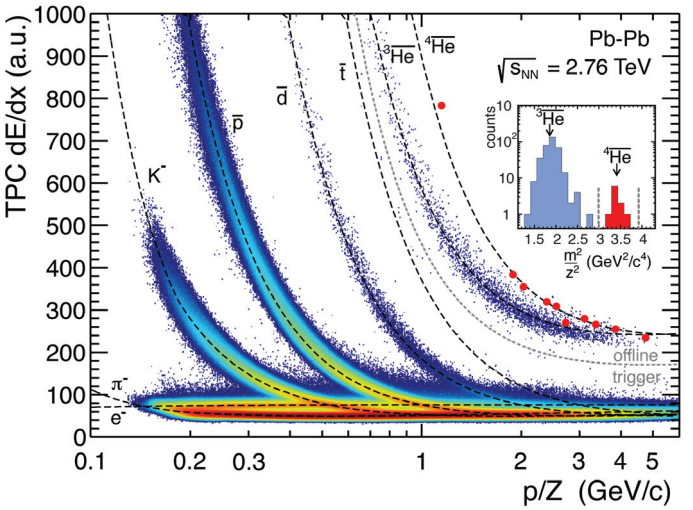

Fig. 51. Measured $\mathrm{d}E/\mathrm{d}x$ signal in the ALICE TPC versus magnetic rigidity, together with the expected curves for negatively-charged particles. The inset panel shows the TOF mass measurement which provides additional separation between $^3\overline{\mathrm{He}}$ and $^4\overline{\mathrm{He}}$ for tracks with $p/Z > 2.3$ GeV/c.

and without particle identification. The pairs were preselected using cuts on p_{T}, impact parameter, and various requirements on the decay topology. In this case, loose particle identification cuts are used to ensure a high efficiency in the selection. A clear reduction of the combinatorial background by a factor of ~ 3 can be seen in Fig. 50, with negligible (a few percent) loss of signal.

7.7.3. *Light nuclei*

In Pb–Pb collisions light nuclei were identified via the $\mathrm{d}E/\mathrm{d}x$ signal in the TPC and time-of-flight measurements with the TOF detector. Figure 51 illustrates the separation between $^3\overline{\mathrm{He}}$ and $^4\overline{\mathrm{He}}$ in TPC and TOF. This identification technique was used to study the formation of antinuclei and hyperons in Pb–Pb collisions.

8. Electron Identification

The detector systems for hadron identification that are described in the previous section are also used to identify electrons. In addition, the following systems have dedicated electron identification capabilities:

- *TRD*: The Transition Radiation Detector identifies electrons based on their specific energy loss and transition radiation (TR) and covers the full central barrel.[i]

[i]As of 2013, 5 out of 18 TRD supermodules are yet to be installed. See Table 2 for details.

- *EMCal*: The Electromagnetic Calorimeter identifies electrons by measuring their energy deposition and comparing it to the measured track momentum (E/p method). The EMCal has a partial coverage $|\eta| < 0.7$ and 107° in ϕ.
- *PHOS*: The Photon Spectrometer is a high-granularity electromagnetic calorimeter that can also identify electrons using the E/p method. PHOS covers $|\eta| < 0.12$ with up to five modules, 20° in azimuth each. Three modules were installed in 2009–2013.

The PHOS, EMCal, and TRD also have capabilities to trigger on high-momentum electrons, charged particles, and photons (PHOS and EMCal only).

These detector systems provide complementary capabilities for electron measurements: the TRD with its large acceptance and triggering capabilities at intermediate $p_{\mathrm{T}} = 2$–5 GeV/c is particularly suited for dilepton measurements, including quarkonia, while the trigger capabilities of EMCal (and PHOS) make it possible to sample the full luminosity for high-p_{T} electron measurements (from heavy-flavor decays). To obtain a pure electron sample for physics analysis, signals from multiple detectors are used (see Subsec. 8.3 for some examples).

8.1. *Electron identification in the EMCal*

Electrons deposit their entire energy in the calorimeter while hadrons typically only lose a small fraction. The ratio E/p of the energy E of EMCal clusters (for cluster finding see Subsec. 9.1.2) and the momentum p of reconstructed tracks that point to the cluster is therefore used to separate electrons and hadrons. An EMCal cluster is considered to be matched to a track when the maximum distance between the extrapolated track position as shown in Fig. 52 is less than a predetermined cutoff value (for a minimum hadron contamination one uses $\Delta\eta < 0.0025$ and $\Delta\phi < 0.005$). The electron–hadron separation can be further enhanced by taking into account the different electromagnetic shower shapes for electrons and hadrons.

In order to determine the E/p distribution, clean electron and hadron samples were obtained from experimental data using the charged tracks originating from decays of neutral particles. Protons and pions are identified from the decays of Λ and K^0_{S} particles and a clean electron sample was obtained from photon conversions in the detector material.

In Fig. 53 the E/p distributions for electrons and pions are shown for experimental and MC data in a transverse momentum interval 2.5 GeV/$c < p_{\mathrm{T}} < 3.0$ GeV/c. The normalization of both distributions is arbitrary and does not reflect the yield ratio between the two particle species. Electrons exhibit a clear peak at $E/pc \sim 1$, with a tail at lower values due to bremsstrahlung in the detector material in front of the EMCal. Pions, on the other hand, are mostly minimum-ionizing particles, with a typical $E/pc \sim 0.1$ and a shoulder at higher values due to additional hadronic interactions in the calorimeter.

The E/p distribution for electrons can be characterized using a Gaussian fit, which then can be cut on for electron identification or used to calculate probability

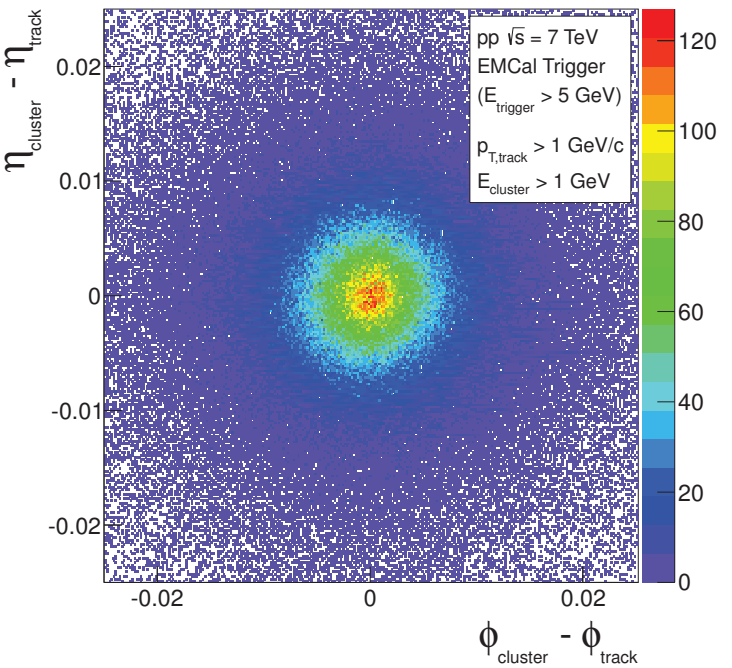

Fig. 52. Distribution of the residuals for the EMCal clusters to track matching in pseudorapidity ($\eta_{\rm cluster} - \eta_{\rm track}$) versus azimuth ($\phi_{\rm cluster} - \phi_{\rm track}$) in pp collisions at $\sqrt{s} = 7$ TeV triggered by EMCal. Only clusters with an energy $E_{\rm cluster} > 1$ GeV and tracks with a transverse momentum $p_{\rm T,\,track} > 1$ GeV/c are used.

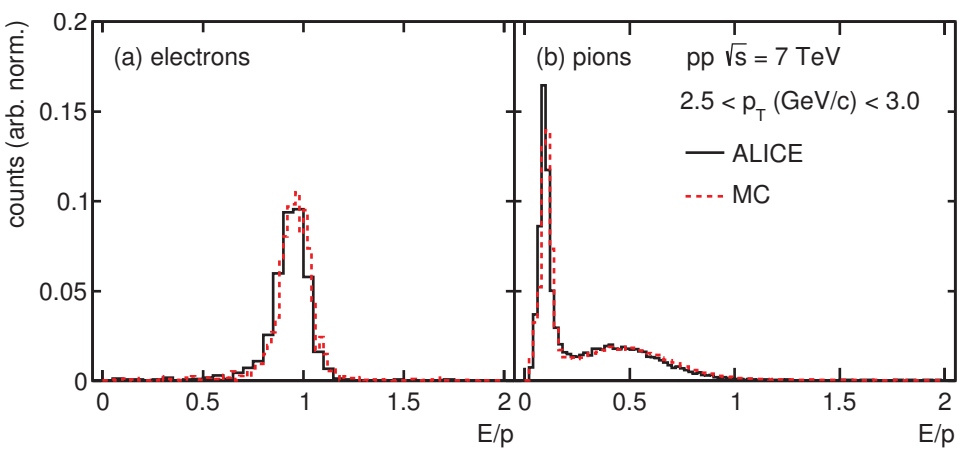

Fig. 53. (Color online) E/p distributions for (a) electrons and (b) pions in pp collisions at $\sqrt{s} = 7$ TeV, measured in the experiment (red dotted line), and compared to simulation (black full line). The samples of identified electrons and pions were obtained from reconstructed γ conversions and $\Lambda/K^0_{\rm S}$ decays, respectively. The simulation is a Pythia simulation with realistic detector configuration and full reconstruction.

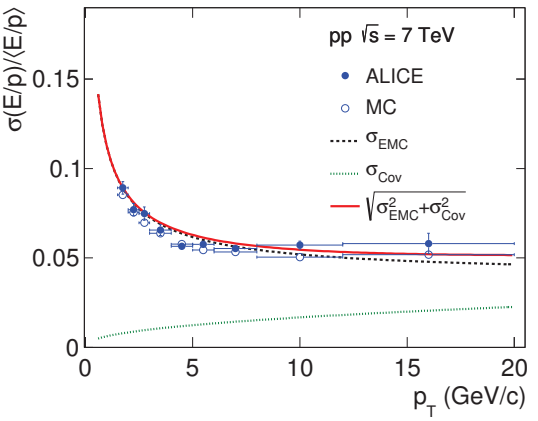

Fig. 54. (Color online) Relative resolution of E/p versus transverse momentum p_{T} for electrons in experimental data (full dots) and from a fully reconstructed MC (open circles) in pp collisions at $\sqrt{s} = 7$ TeV. The EMCal energy resolution deduced from the width of the π^0 and η invariant mass peaks (black dotted line), added in quadrature to the TPC p_{T} resolution (green dash-dotted line), describes the measurement reasonably well (red solid line).

densities and a Bayesian probability. For the latter, a parametrization of the hadron distributions is determined as well. Figure 54 shows the relative resolution of E/p as a function of transverse momentum as measured in the experiment, compared to detector simulations of full events from Pythia. The experimental data are compatible with the simulation within uncertainties. Shown in the same figure are the EMCal energy resolution, deduced from the width of the π^0 and η peaks in the invariant mass distribution of photon pairs, and the momentum resolution of electrons from tracking (relevant at high momentum). The two contributions added in quadrature describe the measured E/p resolution reasonably well.

8.2. *Electron identification in the TRD*

The Transition Radiation Detector provides electron identification in the central barrel ($|\eta| < 0.9$)[73] and can also be used to trigger (L1 hardware trigger, as discussed in Subsec. 3.2) on electrons with high transverse momenta and on jets.[74] The electron identification is based on the specific energy loss and transition radiation. The TRD is composed of six layers consisting of a radiator followed by a drift chamber. Transition radiation is produced when a relativistic charged particle ($\gamma \gtrsim 10^3$) traverses many interfaces of two media of different dielectric constants[75] composing the radiator. On average, for each electron with a momentum above 1 GeV/c, one TR photon (energy range: 1–30 keV) is absorbed and converted in the high-Z gas mixture (Xe-CO_2 [85-15]) in each layer of the detector. Figure 55 shows the combined TRD signal ($\mathrm{d}E/\mathrm{d}x$ and TR) as a function of momentum for p–Pb collisions. The dependence of the most probable TRD signal on $\beta\gamma$ is shown in Fig. 56. The data are from measurements with pions and electrons in

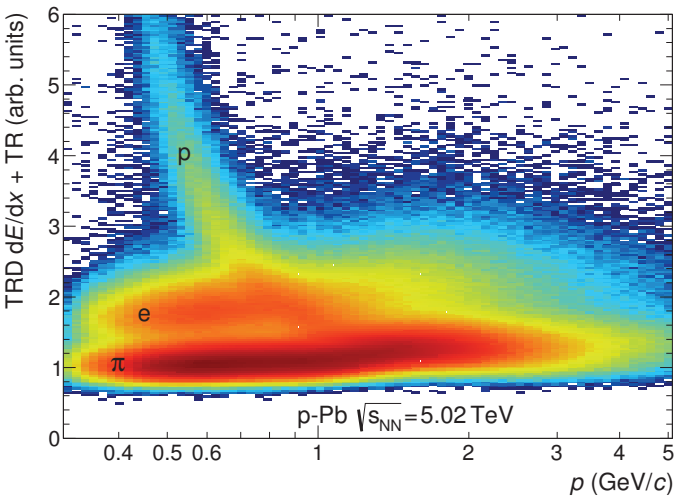

Fig. 55. Sum of the TRD signal (ionization energy loss plus transition radiation) as a function of momentum for protons from Λ decays, charged pions from K^0_S decays, and electrons from γ conversions in p–Pb collisions.

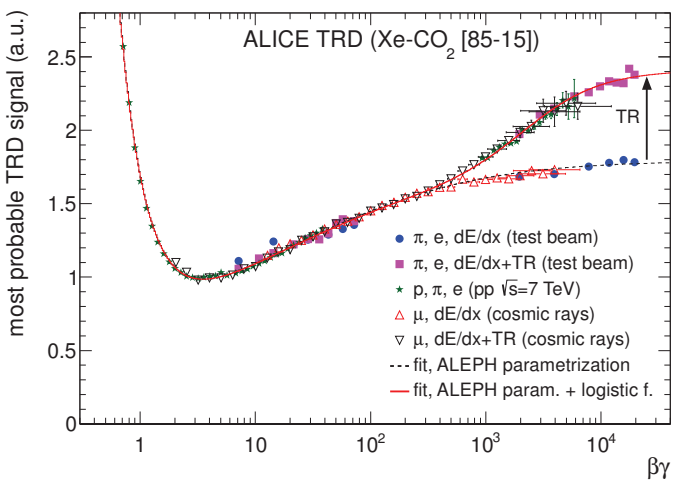

Fig. 56. The most probable TRD signal as a function of $\beta\gamma$. Measurements performed in test beam runs, pp collisions at $\sqrt{s} = 7$ TeV, and cosmic rays are compared.

test beam runs at CERN PS, performed with and without the radiator;[76] protons, pions, and electrons in pp collisions at $\sqrt{s} = 7$ TeV;[77] and cosmic muons triggered by subdetectors of the ALICE setup.[78] With cosmic muons, the selection of the flight direction allows one to measure only the specific energy loss ($\mathrm{d}E/\mathrm{d}x$) or the summed signal ($\mathrm{d}E/\mathrm{d}x + \mathrm{TR}$). The onset of TR production is visible for $\beta\gamma \gtrsim 800$, both for electrons and high-energy (TeV scale) cosmic muons. Also note that the muon signal is consistent with that from electrons at the same $\beta\gamma$.

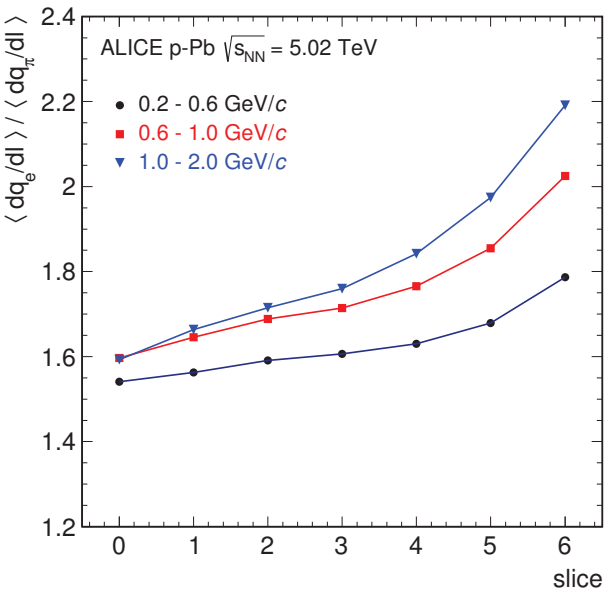

Fig. 57. The ratio of the average signal of electrons to that of pions as a function of the depth in the detector (slice number; the lowest slice number is farthest away from the radiator).

For particle identification, the signal of each chamber is divided into seven slices (starting the numbering at the read-out end farthest away from the radiator), each integrating the sampled signal in about 5 mm of detector thickness. Figure 57 shows the ratio of the average signal for electrons to that of pions as a function of slice number. The TR contribution is visible at large slice numbers (corresponding to long drift times) because the TR is predominantly absorbed at the entrance of the detector.

The above plot was produced using data collected in the recent p–Pb run at $\sqrt{s_{\rm NN}} = 5.02$ TeV. The same data are used to quantify the TRD identification performance. Clean samples of electrons from γ conversions and pions from $K^0_{\rm S}$ decays[77] are selected using topological cuts and TPC and TOF particle identification. The performance of the detector is expressed in terms of the pion efficiency, which is the fraction of pions that are incorrectly identified as electrons. The pion rejection factor is the inverse of the pion efficiency. We employ the following methods: (i) truncated mean;[65,79] (ii) one-dimensional likelihood on the total integrated charge (LQ1D);[77] (iii) two-dimensional likelihood on integrated charge (LQ2D);[80] and (iv) neural networks (NN).[81] The results are compared in Fig. 58, where the pion efficiency is shown as a function of the electron efficiency and as a function of the number of layers providing signals. The truncated mean and the LQ1D are simple and robust methods which provide reasonable pion rejection. The LQ2D and NN methods also make use of the temporal distribution of the signal, which provides about a factor of two improvement of the pion rejection compared to the truncated mean and LQ1D

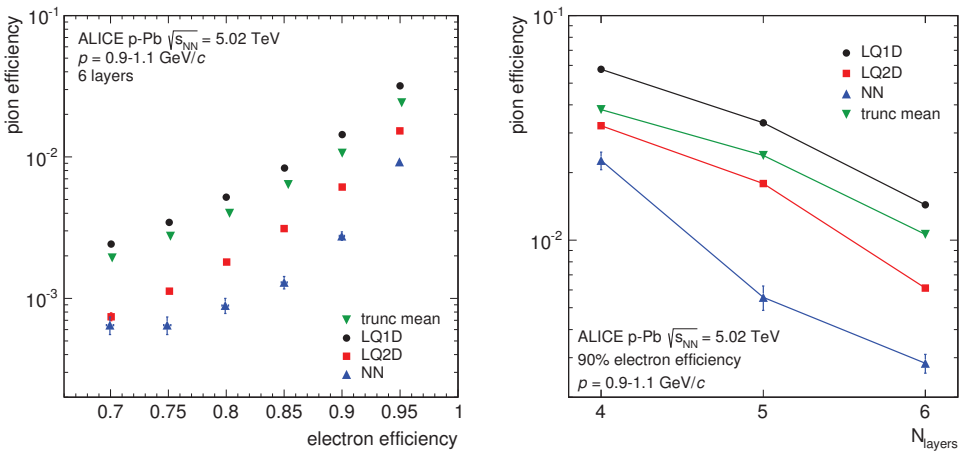

Fig. 58. Pion efficiency as a function of electron efficiency (left panel, for 6 layers) and as a function of the number of layers (right panel, for 90% electron efficiency) for the momentum range 0.9–1.1 GeV/c. The results are compared for the truncated mean, LQ1D, LQ2D, and NN methods.

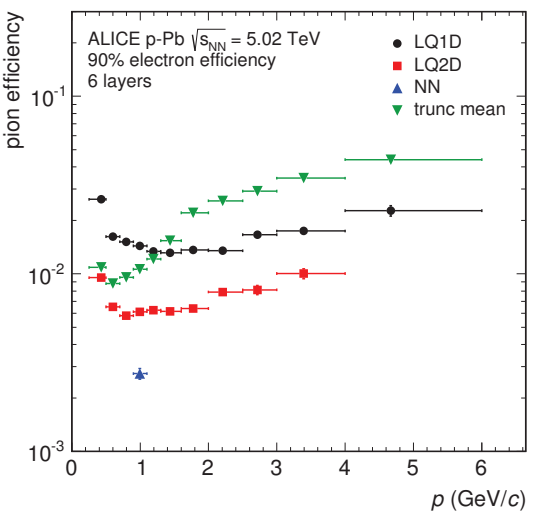

Fig. 59. Momentum dependence of the pion efficiency for the truncated mean, LQ1D, LQ2D, and NN methods. The results are for 90% electron efficiency and for tracks with signals in six layers.

methods. The present pion rejection factors obtained from collision data confirm the design value found in test beams with prototypes.[76]

The momentum dependence of the pion efficiency is shown in Fig. 59. The pion rejection with the LQ1D and LQ2D methods first improves with increasing momentum because of the onset of the transition radiation. Starting from 1–2 GeV/c, the saturation of the TR production and the relativistic rise of the specific energy

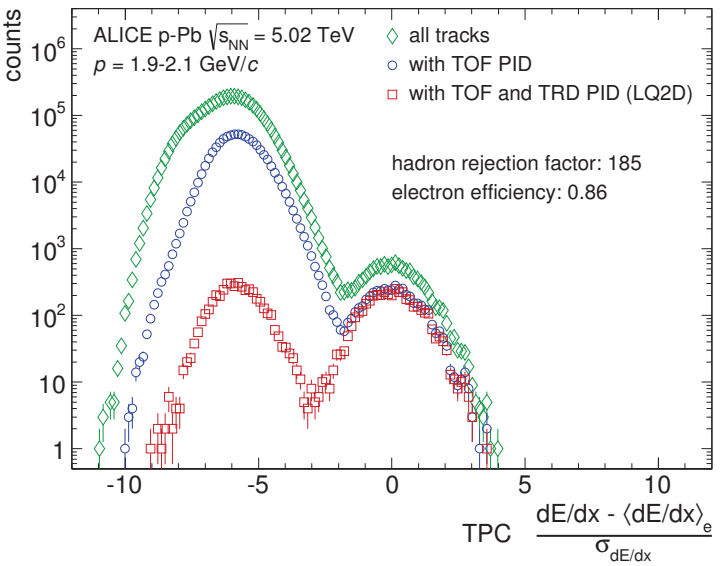

Fig. 60. dE/dx distribution of electron candidate tracks, with TOF and TRD selections (using 6 tracklets in the TRD) in pp collisions. Only tracks with six TRD tracklets are included.

loss of pions lead to a gradual reduction of the electron–pion separation power. The LQ2D method lacks necessary references for momenta above 4 GeV/c. Studies with parametrizations of the respective charge-deposit distributions are ongoing and the first results look promising. The truncated-mean method shows very good pion rejection at low momenta where the energy loss dominates the signal. At higher momenta, the rejection power decreases because the TR contribution, yielding higher charge deposits, is likely to be removed in the truncation.

In addition to the identification efficiency, there is a finite matching efficiency between TPC tracks and TRD clusters, which is $\geq 85\%$ for $p_{\mathrm{T}} > 0.8$ in the azimuthal area covered by the TRD. Losses are mostly due to chamber boundaries.

8.3. *Electron identification in physics analysis*

One of the important uses of electron identification in physics analysis is the measurement of the electron spectrum from semileptonic decays of heavy-flavor hadrons. For this measurement, a very pure electron sample is selected, using a combination of various detectors, such as ITS+TPC+TOF+TRD, or EMCal+TPC.

To illustrate the strength of combined PID for electrons, we show in Fig. 60 the TPC dE/dx distribution of tracks with $p = 2$ GeV/c and compare with track samples where cuts are applied on TOF and TRD to select electrons. It can be seen in the figure that the TOF and TRD cuts reduce the hadron contamination in the track sample, allowing the selection of a very pure electron sample when combined with TPC dE/dx. For details, we refer to the corresponding publication.[82]

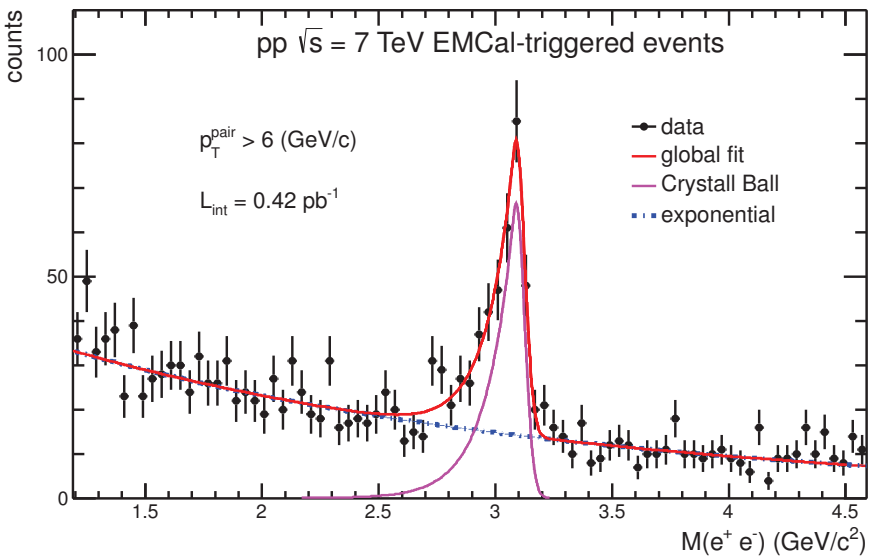

Fig. 61. Invariant mass distribution for J/ψ candidates from EMCal-triggered events in pp collisions at $\sqrt{s} = 7$ TeV ($\mathcal{L} \approx 0.4$ pb^{-1}, 8M events). Electrons are identified by their energy loss in the TPC ($\mathrm{d}E/\mathrm{d}x > 70$) and the E/p ratio in the EMCal ($0.9 < E/p < 1.1$) for both legs. A fit to the signal (Crystal Ball[50]) and the background (exponential) is shown in addition.

Another illustrative case for the application of electron identification is the reconstruction of the decay of the J/ψ meson into an electron and a positron. In this case, rather loose selection cuts are applied on electrons, since the hadronic contamination only enters in the combinatorial background in the invariant mass distribution.

Figure 61 shows the invariant mass distribution of J/ψ candidates decaying into $\mathrm{e}^+\mathrm{e}^-$, identified using the EMCal. In this analysis, electrons from EMCal-triggered events are identified by a combination of TPC energy loss and the E/p ratio. This allows the extension of the p_T interval and leads to a better S/B ratio. More analysis details and results can be found in Refs. 29 and 83.

In Fig. 62 we show the effect of the TRD electron identification for the J/ψ measurement in the 40% most central Pb–Pb collisions at $\sqrt{s_\mathrm{NN}} = 2.76$ TeV. In both the TPC-only and the TPC+TRD combined analysis, electrons were identified through their specific energy loss in the TPC, applying a $(-1.5\sigma, +3\sigma)$ inclusion cut. Pions and protons are rejected via $\pm 3.5\sigma$ and $\pm 4\sigma$ exclusion cuts, respectively. For the TPC-only analysis, the total number of candidates after background subtraction is 4956 ± 482 J/ψ in the invariant mass region 2.92–3.16 GeV/c^2, with a signal-to-background ratio of 0.022 ± 0.002 and a significance of ~ 10.

In the TPC+TRD combined analysis, the LQ2D method was applied, requiring an electron likelihood of at least 0.7. For the data shown here, collected in year 2011, the TRD had only partial coverage (10 out of the 18 TRD supermodules were

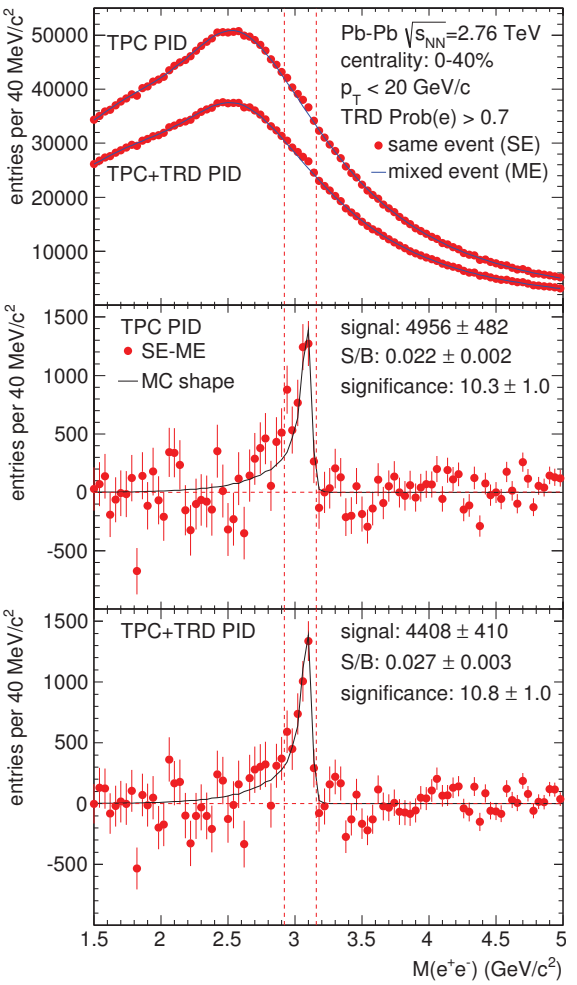

Fig. 62. e^+e^- invariant-mass distribution with TPC-only as well as TPC and TRD particle identification in 0–40% centrality in Pb–Pb collisions at $\sqrt{s_{NN}} = 2.76$ TeV.

installed). Thus the TRD particle identification was used whenever a candidate J/ψ leg had a signal in at least four TRD layers. Despite reduced coverage, the signal to background ratio improved by roughly 20% compared to the TPC-only analysis. The impact of TRD on the significance of the J/ψ yield is small but will increase once all 18 TRD supermodules have been installed.

To significantly enrich the quarkonium sample, the TRD detector was used to select events with electrons at the trigger level 1 (see Sec. 3). For this, track segments (tracklets) were reconstructed locally in the front-end electronics mounted on each chamber. The tracklets were calculated as a straight line fit through the positions of the clusters, determined taking into account the pad response function. The tracklets from different TRD layers are combined using again a straight line fit

and the transverse momentum was determined for tracks which were detected in at least four TRD layers. The p_{T} resolution was better than 20% over the target p_{T} range of 2–8 GeV/c. For the particle identification, the total charge of each tracklet was translated into an electron probability by a look-up table based on reference data with clean electron and pion samples. Pad-by-pad gain variations were corrected for in the front-end electronics, based on Kr calibration. To ensure stable drift velocity and gas amplification, a feedback system was implemented to compensate for environmental changes (mostly of the pressure) by high voltage adjustments. A global electron probability was calculated by averaging over the contributing tracklets. For an electron efficiency of 40%, a pion rejection factor of 200 was achieved in pp collisions. The dominant background was from (low-p_{T}) photons, which convert into $\mathrm{e}^+\mathrm{e}^-$ at large radii and thus produce electrons with small apparent deflection. For an overview of the TRD trigger see Ref. 74.

9. Photons

Photon identification at midrapidity in ALICE is performed either by reconstructing the electromagnetic shower developed in the PHOS and EMCal calorimeters, or by reconstructing electron–positron pairs originating from photons converted in the material of the inner detector ("conversion electrons") with the ITS and TPC using the Photon Conversion Method (PCM).

9.1. *Photon reconstruction with calorimeters*

The central barrel of the ALICE setup contains two calorimeters for photon detection: the Photon Spectrometer (PHOS)[84,85] and the Electromagnetic Calorimeter (EMCal).[86] Both calorimeters have cellular structure with square cells with a transverse size of 2.2×2.2 cm in PHOS ("crystals") and 6×6 cm in EMCal ("towers"), which is roughly equal to (or slightly larger than) the Molière radius. With this choice of cell size, the electromagnetic showers produced by photons and electrons cover groups of adjacent cells (clusters). The material budget of the cells along the particle path is $20X_0$ which is sufficient for photons, electrons, and positrons with about 100 GeV/c to deposit their full energy. For hadronic interactions, the thickness of the cells is about one nuclear radiation length, i.e. the calorimeters are rather transparent for hadrons. The energy deposited by hadrons is small compared with their full energy (see Fig. 53).

The cells of the calorimeters are packed into rectangular matrices called modules in PHOS and supermodules in EMCal. As of 2012, the PHOS detector consists of three modules of 64×56 cells each ($|\eta| < 0.12$, $260^\circ < \phi < 320^\circ$), and the EMCal contains 10 supermodules of 48×24 cells and two supermodules of 48×8 cells ($|\eta| < 0.7$, $80^\circ < \phi < 187^\circ$).

Below, we briefly discuss the cluster finding methods and the photon reconstruction performance of EMCal and PHOS. The electron identification capabilities of the two calorimeters are described in Sec. 8.

9.1.1. *Cluster finder in PHOS*

In PHOS, the cluster finding algorithm starts from any cell with a measured amplitude above some threshold, referred to as the seed energy, E_{seed}.[2] The choice of this seed energy depends on the event environment. In pp collisions the occupancy of the PHOS detector is low, and thus the probability of showers overlapping is small. The seed energy is set to $E_{\text{seed}} = 0.2$ GeV, slightly below the MIP threshold. In the high-multiplicity environment of Pb–Pb collisions, the overlap probability becomes significant. In order to suppress the hadronic background the seed energy is set to $E_{\text{seed}} = 0.4$ GeV. Cells with an energy above the noise level, which share a common edge with the seed cell, are added to the cluster. Subsequently, further cells above the noise level are added if they are adjacent to cells that have already been added.

Clusters can be produced either by a single electromagnetic or hadronic shower, or by several overlapping showers. In the latter case, the cluster may have distinct local maxima, i.e. cells with large energy separated by at least one cell with smaller energy. The presence of such local maxima in a cluster initiates cluster unfolding, which is a procedure that separates the cells of the primary cluster from several clusters corresponding to individual particles. The cluster unfolding algorithm is based on the knowledge of the transverse profile of electromagnetic showers.

9.1.2. *Cluster finder in EMCal*

Due to the larger cell size in EMCal compared to PHOS, the cluster finding algorithm in EMCal varies depending on the event environment.[2] The default algorithm is the same as that implemented in PHOS, used with a seed energy of $E_{\text{seed}} = 0.3$ GeV, slightly above the MIP threshold. At pion transverse momenta $p_{\text{T}} > 6$ GeV/c, showers from decay photons of π^0 start to overlap, thus reducing the performance of the π^0 reconstruction. For such overlapping clusters, a slightly modified version of the cluster finding algorithm stops adding cells at the first local minimum to avoid shower merging from the two decay photons. An alternative algorithm, originally developed for heavy-ion collisions where the cell occupancy of the EMCal detectors is high, uses a fixed shape of 3×3 cells centered around the seed cell.

9.1.3. *Cluster parameters*

Clusters found in the calorimeters are characterized by several parameters. Since photons and electrons are expected to deposit their full energy in the PHOS and EMCal, the sum of cell energies e_i is used as the estimator of the photon or electron energy $E = \sum_{i=1}^{N} e_i$. The photon coordinate $\bar{x}$ in the reference system of the module can be determined as the first moment of the coordinates x_i of the cells contributing to the cluster, weighted by the logarithms of the cell energies $w_i = \max[0, w_0 + \log(e_i/E)]$ with $w_0 = 4.5$. For inclined photons, the center of

gravity of the shower is displaced towards the inclination direction. As the actual incidence angle of photons is not known, one assumes that all detected photons are produced in the primary vertex, meaning that the incidence angle is determined geometrically from the photon hit coordinate. The shape of showers which develop in the calorimeters can be characterized by the eigenvalues λ_0, λ_1 of the covariance matrix built from the cell coordinates and weights w_i,[2] and may be used to differentiate between different incident particle species. A cluster can be further characterized by the time of flight of a particle from the interaction point to the calorimeter, which is selected as the shortest time among the digits making up the cluster.

For PHOS, another cluster parameter defined for high-multiplicity environments using the cluster cell content is the core energy. The core energy is given by the sum of cell energies within a circle of radius $R = 3.5$ cm around the cluster coordinate, where R is defined such that 98% of the electromagnetic shower energy is deposited within this circle.

9.1.4. *Photon identification in calorimeters*

Photon identification in the calorimeters is based on three complementary criteria:

(1) Since photons cannot be traced by the tracking system, a cluster with no reconstructed tracks in the vicinity (as propagated to the calorimeter surface) is considered as a neutral particle candidate.
(2) Showers produced in the active calorimeter medium by photons and hadrons differ by the transverse profile. Shower shape parameters λ_0, λ_1, E_{core} are used to discriminate electromagnetic showers from hadronic ones.
(3) The time-of-flight information of the cluster can be used to identify fast particles and suppress clusters produced by nucleons.

Neutral particle identification is based on the distance between the cluster center and the nearest charged particle track at the face of the calorimeter. As the calorimeter signal for charged hadrons is generated at a finite depth, the centroids of the cluster–track matching distributions are systematically shifted as shown in the left panel of Fig. 63 for PHOS. Knowing the positions and widths (right panel of Fig. 63) of these distributions, one can recognize and suppress clusters produced by charged hadrons. The selection parameters for PHOS and EMCal depend on the cluster energy and the purity of the photon sample required for particular analyses. Typical values for the selection are 0.005 in the azimuthal and 0.003 in pseudorapidity direction.

The shower shape helps in distinguishing between showers produced by single photons, hadrons, and photons from the decay of high-momentum π^0. The latter is more relevant for EMCal, in which photons from the π^0 decay start overlapping from $p_{\mathrm{T}} > 6$ GeV/c. Single photons tend to have spherically shaped showers, while the clusters with merged showers from high-p_{T} π^0 decays are elongated. The elongation

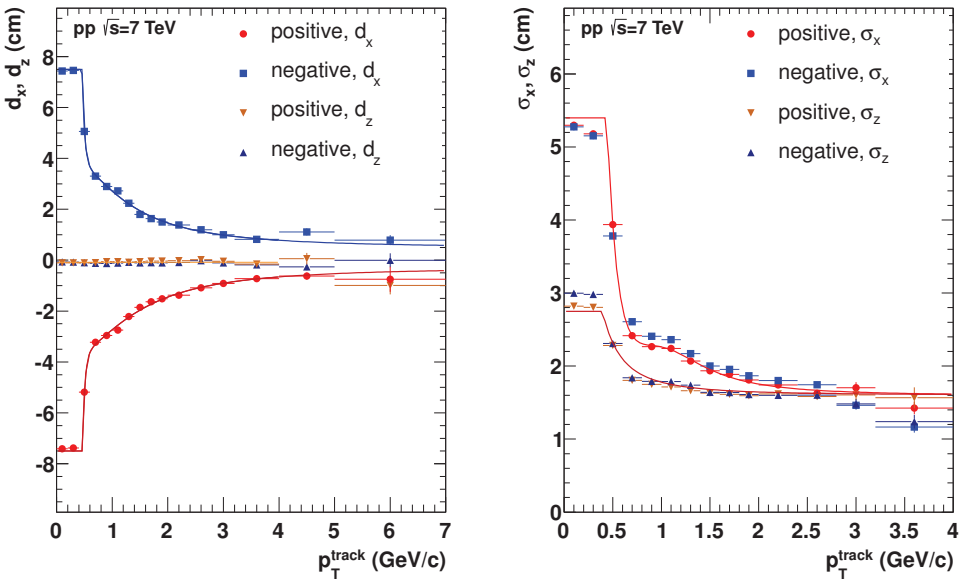

Fig. 63. Mean track matching distance (left) and RMS of the track matching distance distribution (right) for PHOS. The lines are fits to phenomenological parametrizations.

is quantified by the parameter λ_0^2, which is the weighted RMS of the shower energy along the major ellipse axis. For photons the typical value of this shower shape parameter λ_0^2 is around 0.25 independent of the cluster energy, while for π^0 it has a value of $\lambda_0^2 \approx 2.0$ for $p_{\mathrm{T}} \sim 6$ GeV/c and decreases to $\lambda_0^2 \approx 0.4$ at $p_{\mathrm{T}} \sim 30$ GeV/c, allowing for good discrimination between these two kinds of clusters. This feature is especially interesting for the identification of high-momentum π^0's because the invariant mass method (see Subsec. 9.3) has low efficiency above $p_{\mathrm{T}} > 20$ GeV/c for EMCal and $p_{\mathrm{T}} > 60$ GeV/c for PHOS.

To test the quality of the photon identification with the EMCal, π^0's with one of the decay photons converting in the inner material of the experiment (see Subsec. 9.2) and the other decay photon reaching the EMCal (semi-converted π^0) are used to select a photon-enriched sample of clusters. This is achieved by reconstructing the invariant mass of the cluster-conversion pairs and selecting those clusters whose pair masses lie in the π^0 mass range. The λ_0^2 distribution of these clusters is compared to Monte Carlo simulations in Fig. 64. In this simulation, Pythia[87] events are fully reconstructed in the ALICE experiment and subject to standard analysis cuts. The two distributions show satisfactory agreement. The application of these criteria depends on the specific physics analysis being undertaken. For processes with a high signal-to-background ratio, one of the criteria may be sufficient to reach an adequate purity, while in other cases it may become necessary to combine all three photon identification methods.

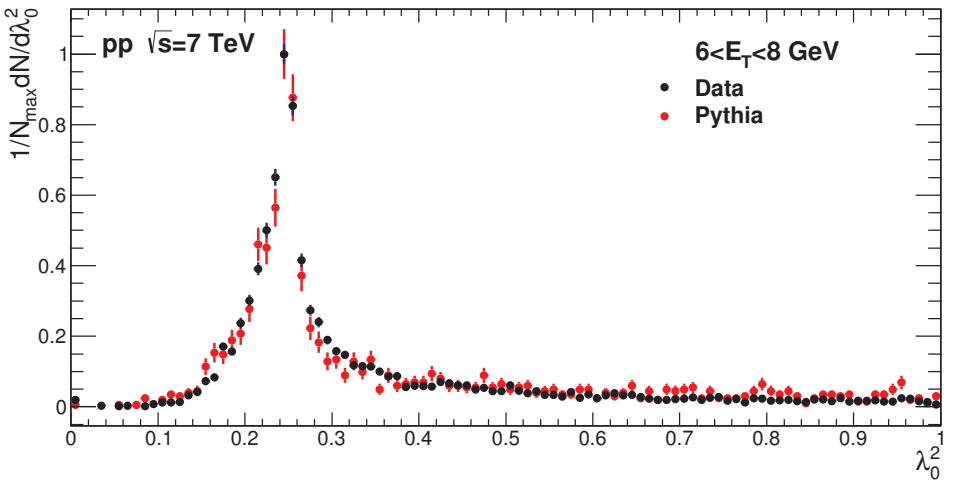

Fig. 64. λ_0^2 distribution of photon clusters in the EMCal with transverse energy of 6 GeV/c < E_{T} < 8 GeV/c originating from "semi-converted" π^0's in pp collisions at 7 TeV compared to Monte Carlo simulation.

9.2. *Photon conversion method*

At energies above 5 MeV, the interaction of photons with detector material is dominated by the creation of positron–electron ($\mathrm{e^+e^-}$) pairs.[2] The converted photon and its conversion point can be reliably measured by reconstructing the electron and positron with the ITS and TPC for conversions within 180 cm from the beam axis. Within the fiducial acceptance ($|\eta| < 0.9$) the main sources for conversions are the beam pipe, the 6 layers of the ITS, the TPC vessels, and part of the TPC drift gas. Outside the fiducial acceptance, the ITS services and the ITS and TPC support structures lead to additional contributions. The photon conversion probability is very sensitive to the amount, geometry, and chemical composition of the traversed material. Therefore, it is vital to have accurate knowledge of the material budget before photon production can be assessed quantitatively.

The converted photons are obtained by employing a secondary vertex algorithm ($\mathrm{V^0}$ finder), as explained in Subsec. 6.4. The same algorithm is used to reconstruct K^0_{S}, Λ, $\bar{\Lambda}$, and γ conversions from reconstructed tracks. In order to obtain a clean photon sample, the PID capabilities of the TPC and TOF are exploited as described in Sec. 8. Electron and positron track candidates are selected by requiring the specific energy loss $\mathrm{d}E/\mathrm{d}x$ in the TPC and the time of flight in TOF to be within $(-4\sigma_{\mathrm{d}E/\mathrm{d}x}, +5\sigma_{\mathrm{d}E/\mathrm{d}x})$ and $(-2\sigma_{\mathrm{TOF}}, +3\sigma_{\mathrm{TOF}})$, respectively, from the values expected for electrons. Tracks close to the pion line in Fig. 34 — within $(-0.5\sigma_{\mathrm{d}E/\mathrm{d}x}, +0.5\sigma_{\mathrm{d}E/\mathrm{d}x})$ and $(-\infty, +0.5\sigma_{\mathrm{d}E/\mathrm{d}x})$ for momenta below and above 0.3 GeV/c, respectively — are rejected. The precision of the photon conversion point estimate can be improved with respect to the one obtained from the $\mathrm{V^0}$ algorithm by requiring that the momentum vectors of the $\mathrm{e^+e^-}$ pair are almost parallel

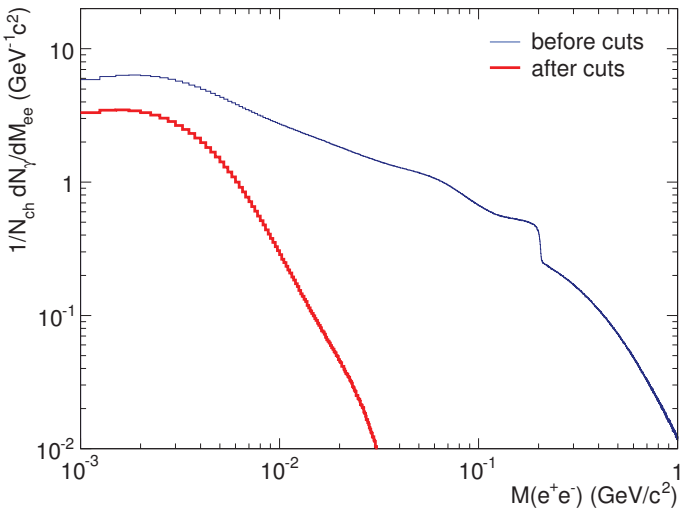

Fig. 65. (Color online) Invariant mass distribution of all reconstructed secondaries (blue) and of the selected photon candidates (red) after all cuts were applied.

at the conversion point. The final photons are selected by a cut of the $\chi^2(\gamma)$/ndf after applying constraints on the photon candidate mass and on the opening angle between the reconstructed photon momentum and the vector joining the collision vertex and the conversion point. The invariant mass distributions of all V^0's calculated with the electron mass hypothesis before and after all selection criteria are shown in Fig. 65.

The distribution of the reconstructed photon conversion points, shown in Figs. 66 and 67 for $|\eta| < 0.9$, represents a precise γ-ray tomography of the ALICE inner barrel detectors. Different layers of the ITS and the TPC are clearly separated. The radial distribution is compared to Monte Carlo (MC) simulations generated with PHOJET.[88] The integrated detector material for $R < 180$ cm and $|\eta| < 0.9$ amounts to a radiation thickness of $11.4 \pm 0.5\%$ X_0, and results in a conversion probability of about 8.5%. The differences between the measured and simulated distributions (apparent mainly at $R = 50$ cm) are taken into account when estimating systematic uncertainties in the analyses that rely on the knowledge of the material. Further details relating to the analysis of the ALICE material distribution, the photon conversion probability and reconstruction efficiency in the inner parts of the detector are discussed in Ref. 89.

9.3. π^0 *and* η *reconstruction*

The detection of light neutral mesons like π^0 and η is a benchmark for photon detectors. The mesons are identified via the invariant mass of photon candidate pairs.[90] For the calorimeters, rather loose photon identification criteria are sufficient to extract the π^0 peak from invariant-mass spectra in pp collisions. In particular,

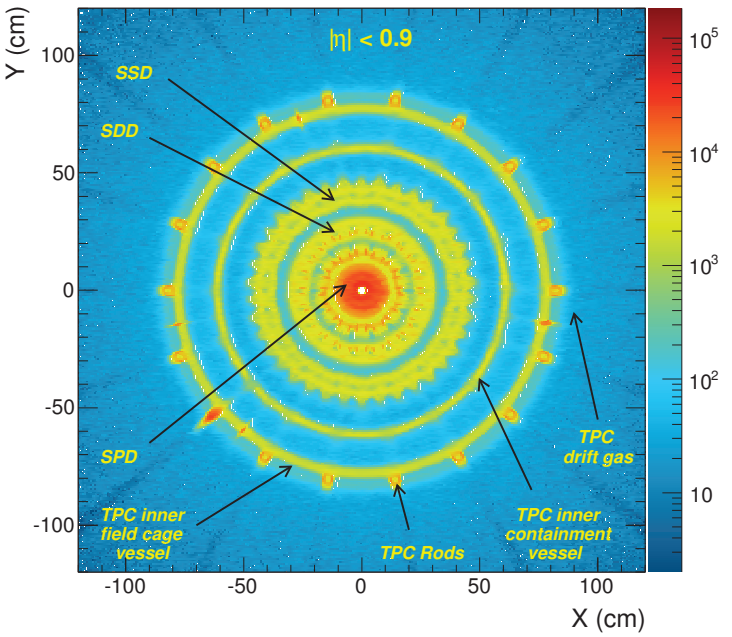

Fig. 66. Transverse distribution of the reconstructed photon conversion points for $|\eta| < 0.9$.

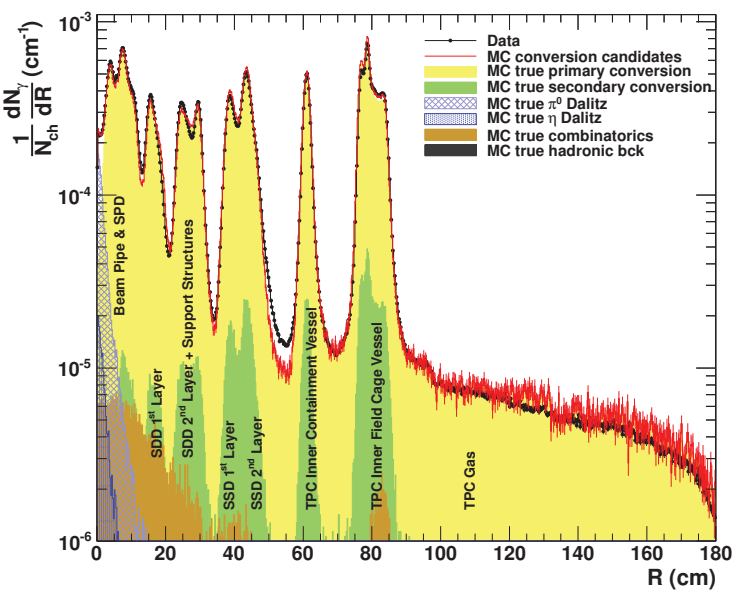

Fig. 67. (Color online) Radial distribution of the reconstructed photon conversion points for $|\eta| < 0.9$ (black) compared to MC simulations performed with PHOJET (red). Distributions for true converted photons are shown in yellow. Physics contamination from true π^0 and η Dalitz decays, where the primary e^+e^- are reconstructed as photon conversions, are shown as dashed blue histograms. Random combinatorics and true hadronic background are also shown.

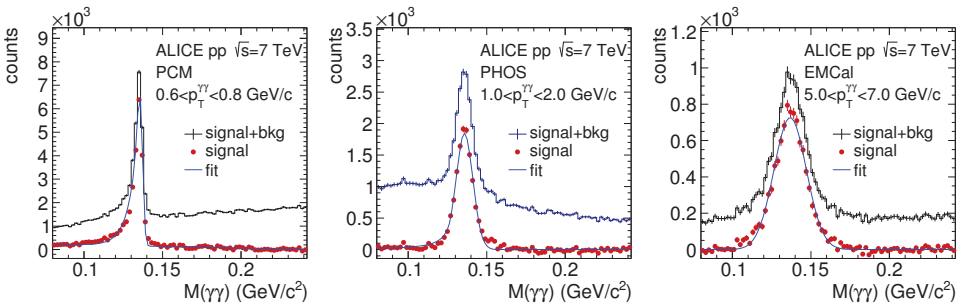

Fig. 68. Invariant mass spectra of photon candidate pairs for pp collisions at 7 TeV by PCM, PHOS and EMCal.

all clusters with an energy $E > 0.3$ GeV (and with three or more cells in PHOS) are considered as photon candidates for π^0 measurement. Figure 68 shows the invariant mass spectra of photon pairs in the mass range around the π^0 peak measured in pp collisions at $\sqrt{s} = 7$ TeV for $0.6 < p_{\mathrm{T}}^{\gamma\gamma} < 0.8$, $1.0 < p_{\mathrm{T}}^{\gamma\gamma} < 2.0$, and $5 < p_{\mathrm{T}}^{\gamma\gamma} < 7$ GeV/c by PCM, PHOS, and EMCal, respectively. The invariant mass distributions are fitted using a Gaussian distribution, leading to a mass position of 135.8 and 136.8 MeV/c^2 with a width of 5.3 and 10.3 MeV/c^2 for PHOS and EMCal, respectively. In the case of PCM, the peak is asymmetric, but nevertheless is fitted by a pure Gaussian to the right of the mass peak, leading to a mass position of 135.8 with a width of 1.5 MeV/c^2. The background is estimated using first-order polynomials after the uncorrelated contribution estimated using the event mixing technique has been subtracted. To contrast the low occupancy environment present in pp collisions, Fig. 69 shows similar invariant mass distributions in the 0–10% most central Pb–Pb collisions at $\sqrt{s_{\mathrm{NN}}} = 2.76$ TeV for $1.4 < p_{\mathrm{T}}^{\gamma\gamma} < 1.6$, $2.0 < p_{\mathrm{T}}^{\gamma\gamma} < 3.0$, and $5 < p_{\mathrm{T}}^{\gamma\gamma} < 7$ GeV/c by PCM, PHOS, and EMCal. For the PHOS and PCM, we show a low p_{T} range illustrating how the S/B worsens in the high-multiplicity environment of central Pb–Pb collisions, while for the EMCal the focus is on higher p_{T} values. To cope with the large occupancy in the calorimeters, the cluster energy is approximated with the core energy E_{core} for PHOS, while for EMCal the minimum

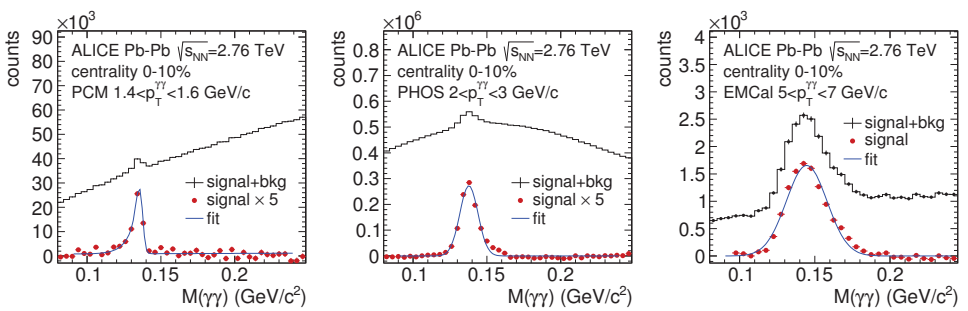

Fig. 69. Invariant mass spectra of photon candidate pairs for 0–10% central Pb–Pb collisions at $\sqrt{s_{\mathrm{NN}}} = 2.76$ TeV by PCM, PHOS and EMCal.

cluster energy is increased to $E > 2$ GeV and a mild cut on the shower shape of $\lambda_0^2 < 0.5$ is required. The mass position and width obtained from the Gaussian fits are 135.6, 137.8, and 144.6 MeV/c^2 for the position, and 1.9, 6.1, and 13.4 MeV/c^2 for the width in PCM, PHOS, and EMCal, respectively. The dependence of the pion mass position and width on the transverse momentum shown in Figs. 70 and 71 is used for tuning the Monte Carlo simulations.

The increasing difference in the mass position between the data and simulation, which gets apparent for the EMCal at momenta above 10 GeV/c in pp collisions, may be improved with a cluster unfolding algorithm based on a model of the transverse profile of the shower in the EMCal. Compared to the calorimeters, the PCM method can be used to measure the π^0 down to very low momentum, but with a rather small efficiency due to the small probability of about 0.7% for both photons to convert. Compared with PHOS, the EMCal has a worse π^0 resolution, but a ~ 10 times larger acceptance. This is illustrated in Fig. 72, which compares the total correction (product of efficiency and acceptance) for $|y| < 0.5$ for PCM, PHOS, and EMCal in pp collisions at $\sqrt{s} = 7$ TeV (left panel) and in 0–10% central Pb–Pb collisions at 2.76 TeV (right panel). The π^0 reconstruction efficiency for the EMCal decreases at around 10 GeV/c due to the fact that the showers from the two decay photons start to overlap significantly. For PHOS, the π^0 reconstruction efficiency is affected by the shower merging only above 25 GeV/c (not shown).

10. Jets

Jet measurements in relativistic nuclear collisions are of particular interest due to the phenomenon of "jet quenching" (Ref. 91 and references therein), in which an energetic parton interacts with the color-charged, hot and dense matter prior to its fragmentation into hadrons. This interaction modifies the hadronic structure and transverse momentum of jets generated in the medium relative to those in vacuum, producing a variety of phenomena that are observable experimentally and can be calculated theoretically.[91] Measurements of jet quenching thus provide unique information on the properties of hot QCD matter.

Operationally, a jet is specified in terms of a reconstruction algorithm[92] that clusters hadrons within a specified distance R in angular space, i.e. $\sqrt{(\Delta\eta)^2 + (\Delta\phi)^2} < R$. The algorithm should be applicable in comparable fashion to both experimental data and theoretical calculations based on perturbative QCD, dictating that it be both infrared safe (jet measurement stable against additional soft radiation) and colinear-safe (independent of the details of fragmentation of the parton shower into final-state hadrons).[92]

Jet reconstruction in nuclear collisions is especially challenging, owing to the large and inhomogeneous background in such events. The accurate measurement of jets in heavy-ion collisions requires careful accounting of both the overall level of underlying event background, and the influence of its region-to-region fluctuations.[93–95]

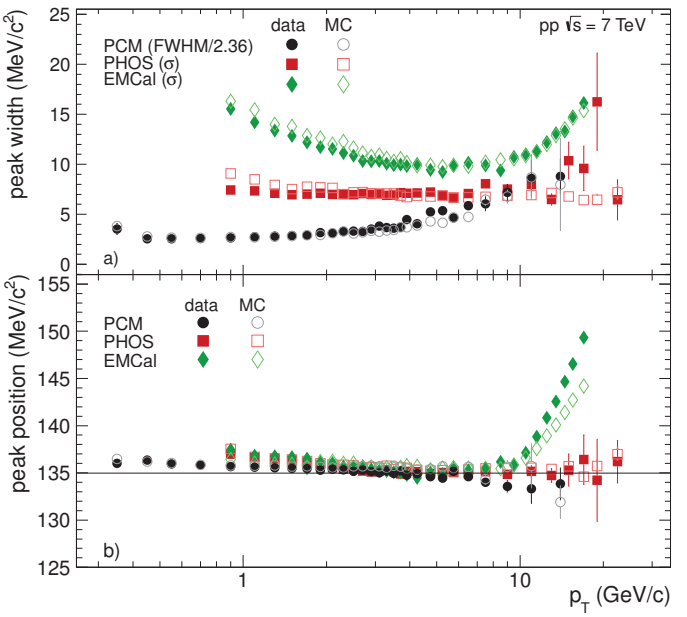

Fig. 70. Reconstructed π^0 peak width (a) and position (b) in pp collisions at $\sqrt{s} = 7$ TeV for PCM, PHOS, and EMCal compared to Monte Carlo simulations (Pythia for PCM and PHOS, and embedding of clusters from single π^0 in data for EMCal).

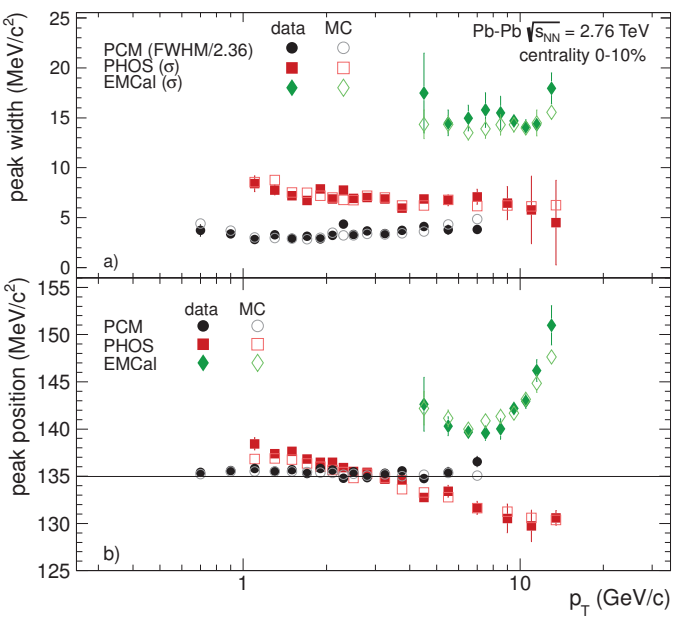

Fig. 71. Reconstructed π^0 peak width (a) and position (b) in 0–10% central Pb–Pb collisions at $\sqrt{s_{\rm NN}} = 2.76$ TeV for PCM, PHOS, and EMCal compared to Monte Carlo simulations (Hijing for PCM, and embedding of clusters from single π^0 in data for PHOS and EMCal).

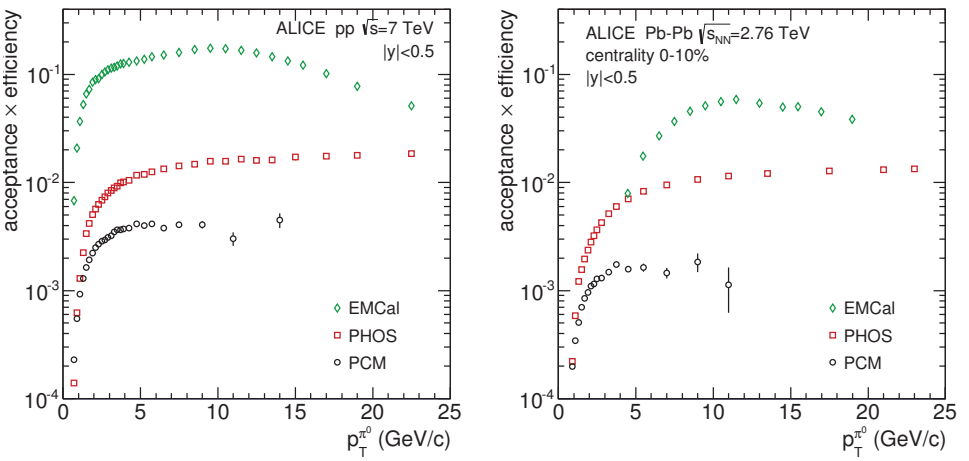

Fig. 72. Total correction (efficiency and acceptance) for $|y| < 0.5$ for π^0 reconstruction via two-photon invariant mass determination in pp collisions at $\sqrt{s} = 7$ TeV (left panel) and in 0–10% central Pb–Pb collisions at $\sqrt{s_{NN}} = 2.76$ TeV (right panel) for PCM, PHOS, and EMCal.

Jets are measured within ALICE in the central detector, utilizing charged particle tracking in ITS and TPC (see Sec. 1) for the charged hadronic energy and electromagnetic (EM) calorimetry to measure the neutral hadronic energy carried by photons (π^0, $\eta, \ldots$).[86] This approach is closely related to "Particle Flow" methods[96] and enables detailed control of the constituent particles used in the jet reconstruction. This is of especial importance in the complex heavy-ion collision environment. The inclusive jet cross section, measured using this technique in pp collisions at $\sqrt{s} = 2.76$ TeV, has been reported by ALICE.[34] Jet measurements using a similar approach have also been reported for pp collisions at RHIC.[97–99]

In this section we present the current performance of ALICE jet reconstruction. The emphasis is on the recently completed measurement of the inclusive jet cross section in pp collisions at $\sqrt{s} = 2.76$ TeV,[34] together with considerations for ongoing heavy-ion jet analyses.

10.1. *EMCal jet trigger*

The ALICE EMCal,[86] a lead-scintillator electromagnetic calorimeter covering 107 degrees in azimuth and $|\eta| < 0.7$, is used to trigger on jets. The jet trigger in Ref. 34 is based on the EMCal single shower (SSh) trigger, labeled E0 in Table 8, which utilizes the fast hardware sum of transverse energy (E_{T}) in groups of 4×4 adjacent EMCal towers, implemented as a sliding window. An SSh trigger accept is issued if the threshold is exceeded by at least one EMCal tower group. The nominal threshold was 3.0 GeV for the data recorded in pp collisions at $\sqrt{s} = 2.76$ TeV. An event is accepted if it also passes the minimum bias (MB) trigger requirements.

The EMCal Jet Patch (JP) trigger (EJE and EJE2 in Table 8) sums tower energies within a sliding window of 32 by 32 adjacent EMCal towers, corresponding

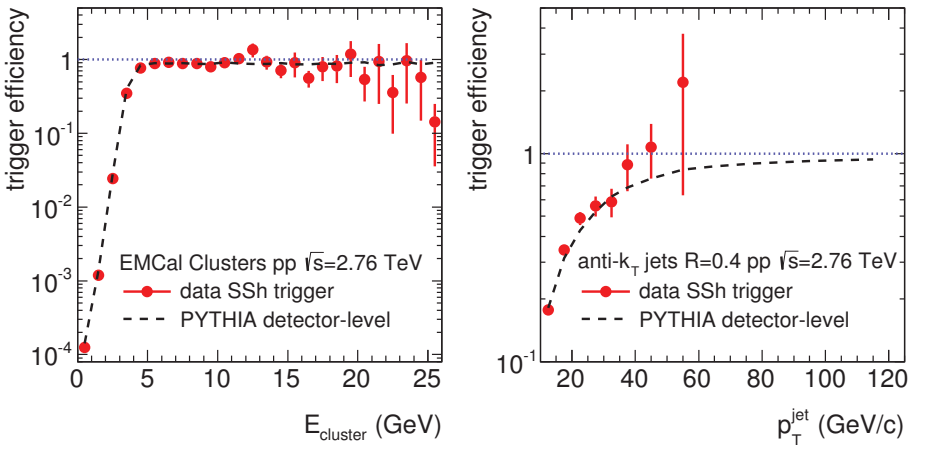

Fig. 73. (Color online) SSh trigger efficiency in pp collisions at $\sqrt{s} = 2.76$ TeV. Efficiency for single EM clusters (left panel) and reconstructed jets (anti-kT, $R = 0.4$, right panel) for data (red points) is well reproduced in simulation (black dashed line). See text for details.

to $\Delta\eta \times \Delta\phi \approx 0.46 \times 0.46$. For heavy-ion running, the JP integrated energy is corrected for the underlying event in the collision prior to comparison to the trigger threshold. This correction is based on the analog charge sum in the V0 detectors at forward rapidity (see Table 1), which is observed to be highly correlated with the transverse energy measured in the EMCal acceptance. The V0 signal provides a centrality estimator that is used by the programmable logic of the EMCal Summable Trigger Unit to adjust the JP trigger threshold on an event-wise basis.[86]

Figure 73, left panel, represents the SSh trigger efficiency for single EM clusters in pp collisions at $\sqrt{s} = 2.76$ TeV, measured by comparing to MB data. Also shown is a calculation of the SSh trigger efficiency from a detailed, detector-level simulation based on the PYTHIA event generator (Perugia 2010 tune) and GEANT3. The distribution of data is normalized to the simulated distribution in the region $p_{\mathrm{T}} > 5$ GeV/c. Good agreement is observed between measurement and simulation in the turn-on region of the trigger.

Figure 73, right panel, shows the efficiency of the SSh trigger for jets in pp collisions at $\sqrt{s} = 2.76$ TeV. Jets are reconstructed offline using the anti-kT algorithm,[100] $R = 0.4$. The red points show the trigger efficiency measured in data as the ratio of jet yields in SSh-triggered and MB data. Since the kinematic reach of the MB dataset is limited, we also assess the jet trigger bias by a data-driven simulation, shown by the black dashed line. This calculation utilizes the measured EM cluster trigger efficiency (left panel, red points), together with the detailed detector-level simulation (PYTHIA6 + GEANT3) to model the jet response. The simulation and data differ in the trigger turn-on region by $\sim$18% in yield, corresponding to a shift in Jet Energy Scale of $\sim$1–2 GeV. This shift is within the precision of the simulation, and is accounted for in the systematic uncertainties of the corresponding cross-section measurement.[34]

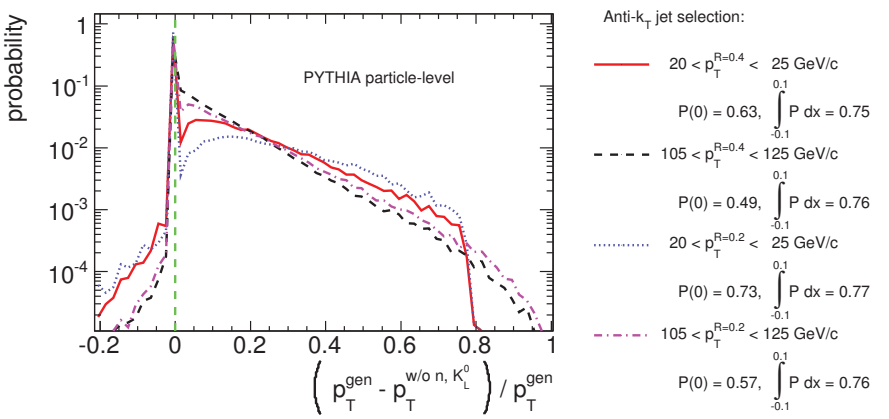

Fig. 74. PYTHIA particle-level simulation of jet-by-jet energy shift due to unobserved contributions from neutrons and K_L^0.

10.2. *Jets in pp collisions*

Instrumental corrections and systematic uncertainties of jet measurements depend on the jet observable under consideration. In this section we discuss the main instrumental corrections for measurement of the inclusive jet cross section in pp collisions at $\sqrt{s} = 2.76$ TeV, with more detail found in Ref. 34.

10.2.1. *Undetected hadronic energy*

Long-lived neutral hadrons (principally, neutrons and K_L^0), will not be detected by the tracking system and will most often deposit only a small fraction of their energy in the EMCal. Correction for this unobserved component of jet energy is based on simulations. PYTHIA predictions for high-p_{T} identified particle production have been compared with ALICE inclusive measurements of high-p_{T} protons and charged kaons in 2.76 TeV pp collisions, with good agreement observed. The systematic uncertainty in the jet energy correction arising from this comparison of simulations and measurement is negligible.[34]

Figure 74 shows a PYTHIA particle-level simulation of the shift in jet energy due to unobserved neutral hadronic energy, calculated on a jet-by-jet basis. Jet reconstruction (anti-kT, $R = 0.2$ and 0.4) was carried out twice on each simulated event: first including all stable particles except neutrinos, and then excluding the neutron and K_L^0 component. The distribution of the relative difference in reconstructed jet energy is shown for various intervals in jet p_{T}, where the difference is normalized by the jet energy calculated without contribution from neutrons and K_L^0. The calculation exhibits no shift in jet energy for between 50% and 70% of the jet population, corresponding to the probability for jets not to contain an energetic neutron or K_L^0 among its fragments. A tail to positive momentum shift Δp_{T} is observed, corresponding to energy lost due to the unobserved energy. A small tail to

negative Δp_{T} is also observed, corresponding to rare cases in which the exclusion of a neutron or K_L^0 shifts the jet centroid significantly, causing the jet reconstruction algorithm to include additional hadrons from the event. For jets reconstructed with anti-kT, $R = 0.4$, the Jet Energy Scale correction and systematic uncertainty due to this effect is $(4 \pm 0.2)\%$ for jet $p_{\mathrm{T}} = 20$ GeV/c, and $(6 \pm 0.5)\%$ at 100 GeV/c.[34]

10.2.2. *Charged particle energy deposition in EMCal*

Charged hadrons and electrons shower in the EMCal, and are also measured by the ALICE tracking system. Their contribution to EMCal cluster energy must be accounted for, in order not to double-count a fraction of their energy in the measured jet energy. The correction procedure minimizes dependence on the simulation of hadronic and EM showers.

Charged-particle trajectories are propagated to a depth of $10X_0$ in the EMCal, with each track then matched to the nearest EMCal cluster falling within $\Delta\eta = 0.015$ and $\Delta\phi = 0.03$. Multiple charged tracks can be matched to a single cluster, though the probability for multiple matches is less than 0.5% for pp collisions. We then define Σ_{p} to be the sum of the 3-momentum magnitude of all matched tracks. For measured cluster energy E_{clust}, the corrected cluster energy E_{corr} is set to zero if $E_{\mathrm{clust}} < f_{\mathrm{sub}} \cdot \Sigma_{\mathrm{p}} c$; otherwise, $E_{\mathrm{corr}} = E_{\mathrm{clust}} - f_{\mathrm{sub}} \cdot \Sigma_{\mathrm{p}} c$, where $f_{\mathrm{sub}} = 1$ for the primary analysis and is varied for systematic checks. The correction to the cluster energy, $\Delta E_{\mathrm{corr}} = E_{\mathrm{clust}} - E_{\mathrm{corr}}$, takes the following values:

$$\Delta E_{\mathrm{corr}} = \begin{cases} E_{\mathrm{clust}} & \text{for} \quad E_{\mathrm{clust}} < f_{\mathrm{sub}} \cdot \Sigma_{\mathrm{p}} c\,, \\ f_{\mathrm{sub}} \cdot \Sigma_{\mathrm{p}} & \text{for} \quad E_{\mathrm{clust}} > f_{\mathrm{sub}} \cdot \Sigma_{\mathrm{p}} c\,. \end{cases} \tag{17}$$

To examine the distribution of ΔE_{corr}, we specify $f_{\mathrm{sub}} = 1$ and consider the following ratio, which is calculated on a cluster-by-cluster basis:

$$R_{\mathrm{corr}} = \frac{\Delta E_{\mathrm{corr}}}{\Sigma_{\mathrm{p}} c}\,. \tag{18}$$

Figure 75 shows the normalized probability distribution of R_{corr} measured in four different bins of Σ_{p} for MB and EMCal-triggered pp collisions, each compared to a detector-level simulation (PYTHIA6). For a cluster whose energy arises solely from matched charged tracks, i.e. which does not contain photons or untracked charged particles, the ratio $R_{\mathrm{corr}} = E/pc$, where E is the EMCal shower energy and p is the momentum of the charged tracks contributing to the shower. The probability per cluster for pileup from photons or untracked charged particles in pp collisions is less than 0.5%, so that Fig. 75 represents, to good accuracy, the *in-situ* measurement of E/p for the EMCal.

The peak at unity in Fig. 75 corresponds to 100% of the matched track momenta being subtracted from the cluster energy. Full containment of a hadronic shower in the EMCal is unlikely, and the peak at unity originates in part from over-subtraction from pileup due to neutral particles and unmeasured charged particles.

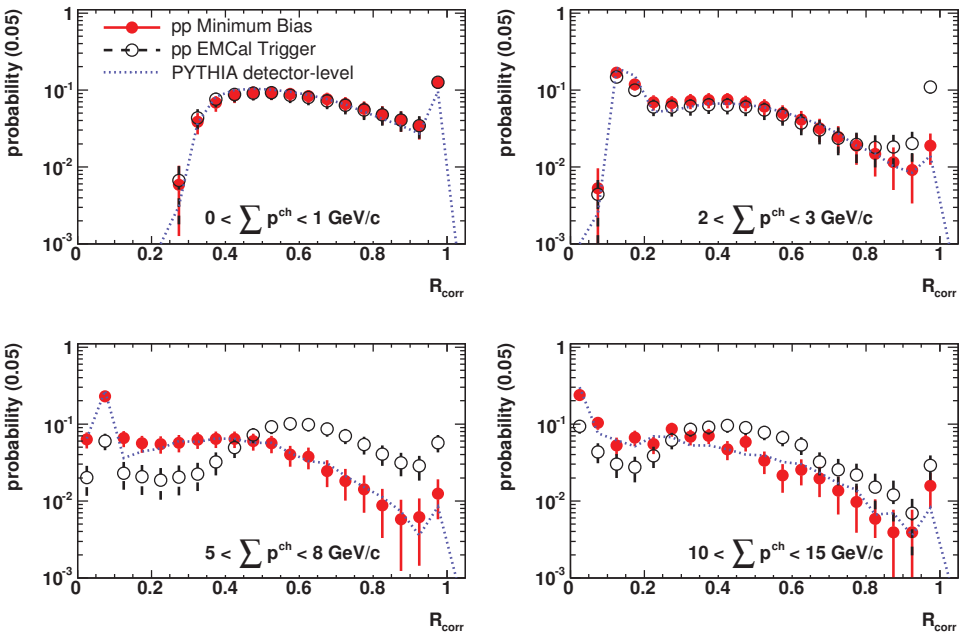

Fig. 75. Probability distribution of R_{corr} (Eq. (18)) for various intervals of Σ_{p}, measured in MB and EMCal-triggered pp collisions, compared to detector-level simulations based on PYTHIA.

The figure shows that the distribution of R_{corr} for the MB trigger is modeled well by a PYTHIA-based detector-level calculation. The variation in the distribution for the EMCal-triggered data is due to the trigger bias: the EMCal trigger at threshold favors highly abundant low p_{T} charged hadrons that deposit above-average energy in the EMCal.

Detector-level simulations show that the above procedure corrects the Jet Energy Scale to within 1–2% in pp collisions, for choices of f_{sub} between 0.7 and 1.0. The contribution of this correction to the Jet Energy Resolution is about 5% at $p_{\mathrm{T}}^{\mathrm{jet}} = 40$ GeV/c, and 8% at $p_{\mathrm{T}}^{\mathrm{jet}} = 100$ GeV/c.

10.2.3. *Other corrections*

Other significant corrections to the inclusive jet cross-section measurement are due to the tracking efficiency and track momentum resolution. A brief discussion of these effects is found below; for further details see Ref. 34.

Jets in pp collisions are made up of a limited number of particles, with large jet-to-jet fluctuations in both the p_{T} distribution of the constituents and the relative fraction of jet energy carried by neutral or charged particles. The effect of tracking efficiency on measured jet p_{T} is therefore not modeled well by a Gaussian distribution, but has a more complex form. This distribution has been studied using PYTHIA-based simulations, which show that for 74% of jets with particle-level p_{T}

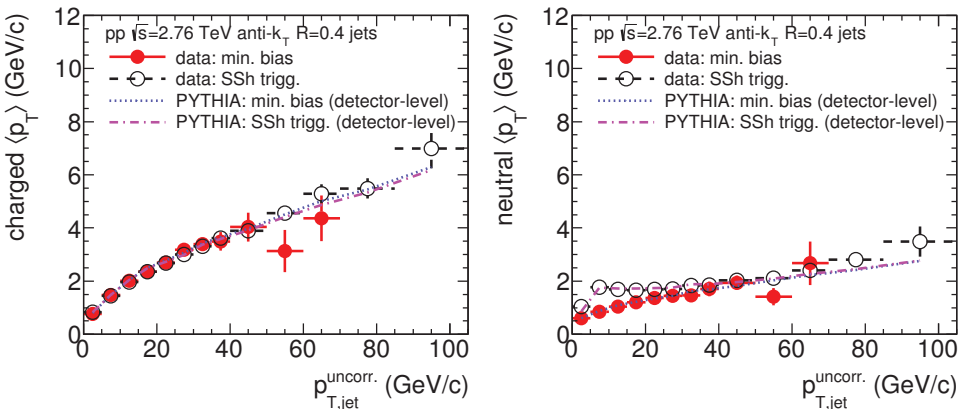

Fig. 76. Mean transverse momentum, $\langle p_{\mathrm{T}} \rangle$, of constituents measured in reconstructed jets in 2.76 TeV pp collisions (anti-kT, $R = 0.4$) versus jet p_{T}. Left: charged tracks; Right: neutral clusters. Data are shown for MB and SSh triggers, and are compared to detector-level simulations.

in the range 105–125 GeV/c (anti-kT, $R = 0.4$) the p_{T} shift due to tracking efficiency is below 10%. For 30% of the population, the shift is negligible. For pp collisions at $\sqrt{s} = 2.76$ TeV, tracking efficiency generates a Jet Energy Scale uncertainty of 2.4% and a multiplicative correction to the inclusive jet cross section of a factor of 1.37 ± 0.12.[34]

The p_{T} resolution of tracking and the energy resolution of the EMCal contribute an uncertainty in Jet Energy Scale of 1–2%, generating a systematic uncertainty in the inclusive jet cross section that is small compared to other contributions.[34] This arises because jets are multi-hadron objects whose energy is carried to a significant extent by a number of relatively low p_{T} constituents, with average constituent p_{T} increasing only gradually with jet p_{T}.

10.2.4. *Jet structure*

We next compare specific features of reconstructed jet structure in data and PYTHIA-based detector-level simulations. Figure 76 shows the jet p_{T} dependence of the mean hadron p_{T} within the jet, $\langle p_{\mathrm{T}} \rangle$, for charged tracks (left) and neutral clusters (right), for both MB and SSh-triggered event populations. The value of $\langle p_{\mathrm{T}} \rangle$ rises slowly with jet p_{T}, and is well described by the detector-level PYTHIA simulation over the full measured range.

Figure 77, left panel, shows the mean number of jet constituents (total number of charged tracks and neutral clusters), while the right panel shows the mean Neutral Energy Fraction (NEF). Both distributions are presented as a function of jet p_{T}. PYTHIA detector-level simulations describe both distributions accurately, for both the MB and SSh-triggered datasets. The NEF distributions are discussed in more detail in Ref. 34.

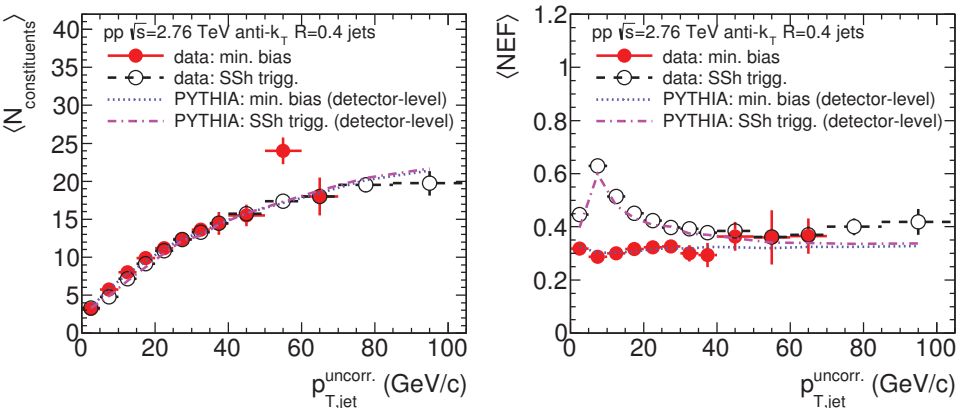

Fig. 77. Mean total number of constituents (left) and mean neutral energy fraction (right) measured in reconstructed jets in 2.76 TeV pp collisions (anti-kT, $R = 0.4$), versus jet p_{T}. Data are shown for MB and SSh triggers, and are compared to detector-level simulations.

10.2.5. *Jet energy resolution*

Jet Energy Resolution is calculated using simulations, with all significant components of the simulation validated against data (e.g. Figs. 76 and 77; see further discussion in Ref. 34). Jet reconstruction is carried out on each generated event at both particle and detector level. Reconstructed jets whose centroids lie close in (η, ϕ) at the particle and detector level are identified, and their relative difference in reconstructed jet energy is calculated according to:

$$\Delta p_{\mathrm{T}} = \frac{p_{\mathrm{T}}^{\mathrm{det}} - p_{\mathrm{T}}^{\mathrm{part}}}{p_{\mathrm{T}}^{\mathrm{part}}} \,. \tag{19}$$

Figure 78, upper panel, shows the distribution of Δp_{T} for three ranges of jet p_{T}. The distributions are weighted towards negative values, corresponding to lower energy at the detector level. The lower panels show the median and mean (left) and RMS (right) of the upper distributions, as a function of particle-level p_{T}. The mean relative energy shift (Jet Energy Scale, or JES, correction) is seen to be p_{T}-dependent, ranging between 17% and 22%. The RMS, corresponding to the Jet Energy Resolution (JER), is seen to be a weak function of jet p_{T} in the range 40–100 GeV, varying between 18% and 20%.

10.3. *Jets in heavy-ion collisions*

Full jet reconstruction in heavy-ion collisions offers the possibility to measure jet quenching effects at the partonic level, without the biases intrinsic to measurements based on high p_{T} single hadrons, which suppress direct observation of the structure of quenched jets. While hard jets are clearly visible in event displays of single heavy-ion collisions (see Fig. 79), accurate measurement of the energy of such jets on an event-by-event basis is challenging, due to the large and inhomogeneous

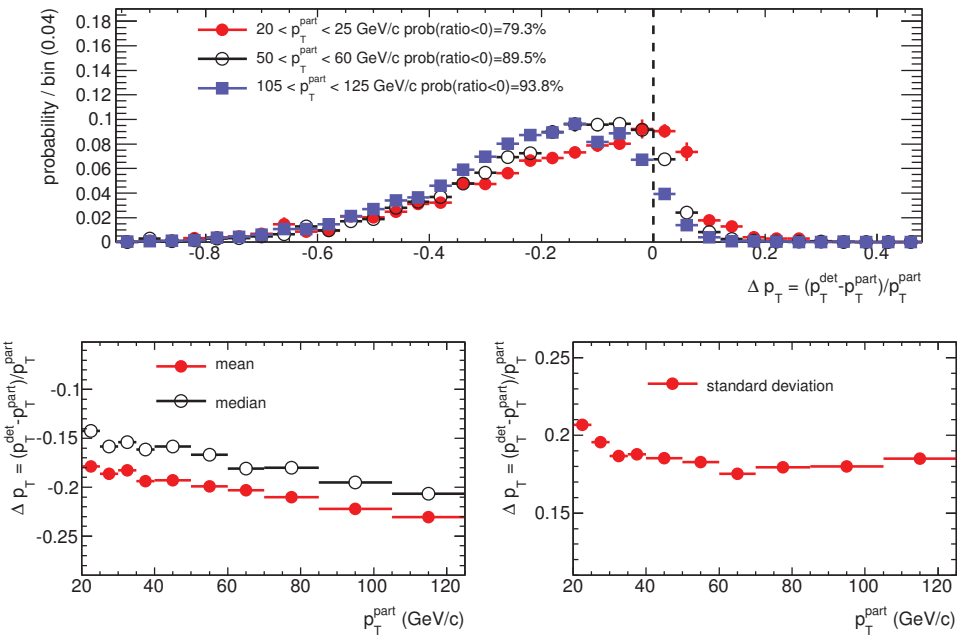

Fig. 78. Instrumental effects on jet energy measurement (Eq. (19)). Upper panel: jet-by-jet distribution for various intervals in jet p_{T}. Lower panels: Mean and median (left) and standard deviation (right) of these distributions.

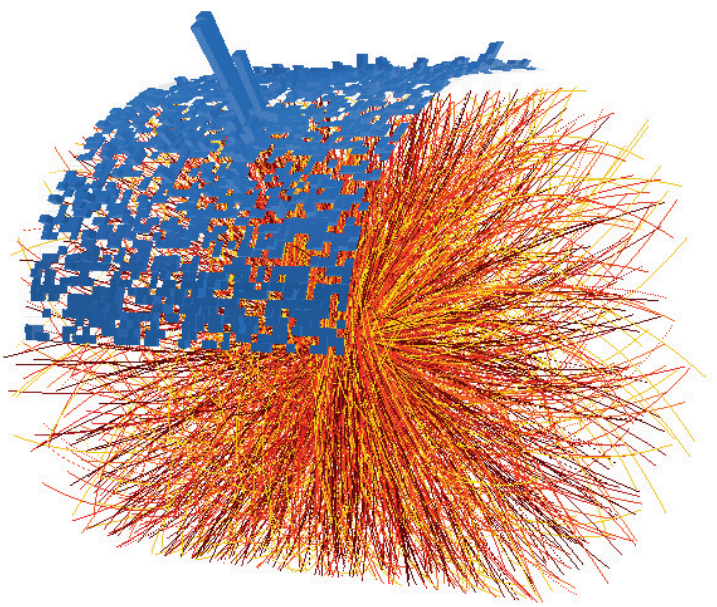

Fig. 79. Event display of a central Pb–Pb collision containing a high p_{T} jet in the EMCal acceptance. The event was triggered using the EMCal SSh trigger.

underlying background. The mean background energy in a cone of radius $R = 0.4$ is about 60 GeV in a central Pb–Pb collision, though the distribution of this quantity has a large tail to much higher values. It is not possible to discriminate the hadronic component of a hard jet from that of the background on a rigorous basis, and any jet reconstruction algorithm applied to such events will therefore incorporate hadrons arising from multiple incoherent sources (hard jets, mini-jets, soft production) into the same jet. This results in a significant distortion ("smearing") of the hard jet energy distribution, together with generation of a large population of "combinatorial" jets comprising solely hadrons generated in soft processes. The latter population has no distinct physical origin, and is experimental noise.

Since jet quenching is generically expected both to soften and to broaden the fragmentation pattern of jets in medium relative to jets in vacuum, care must be taken in the choice of instrumentation and algorithm to preserve the soft component of jets in heavy-ion measurements. ALICE's unique capabilities to measure hadrons efficiently down to very low p_{T} raise the possibility of jet reconstruction with very low infrared cutoff (~ 0.2 GeV/c), even in heavy-ion collisions. Techniques to remove the combinatorial component from the measured jet population and to correct the remaining hard-jet distribution for the effects of background, while preserving the low infrared cutoff, are outlined in Refs. 93, 101 and 102. These techniques have recently been applied to ALICE data to measure the inclusive jet cross section[102,103] and hadron-jet coincidences[104] in Pb–Pb collisions. Full analyses of jets in heavy-ion collisions will be reported in forthcoming ALICE publications. Correction for background depends upon the physics observable under consideration, and we do not consider it further here.

The remainder of this section discusses instrumental corrections for heavy-ion jet measurements, which are similar to those applied in pp collisions (see Ref. 34 and discussion above). The main difference arises in the correction for charged particle energy deposition in the EMCal, due to the greater pileup contribution of photons and untracked charged particle energy to EMCal clusters, arising from the high multiplicity in heavy-ion events. For pp collisions, the cluster pileup probability is less than 0.5%, whereas in central Pb–Pb collisions the probability of having two or more particles contributing above noise threshold to the cluster energy is about 5%.

We utilize the probability distribution of R_{corr} (Eq. (18)), which corresponds to the EMCal E/p distribution in the absence of cluster pileup, to assess the effects of pileup in the heavy-ion environment. The R_{corr} probability distribution is shown in Fig. 75 for pp collisions, and in Fig. 80 for central (0–10%) and peripheral (70–80%) Pb–Pb collisions, in two different intervals of Σ_{p}. Figure 80 also shows two different detector-level simulations: the PYTHIA distribution is the same as that shown in Fig. 75, which accurately describes the R_{corr} distribution for MB pp collisions, while Hijing is used to model the R_{corr} probability distribution for 0–10% central Pb–Pb collisions.

All data and simulated distributions in Fig. 80 are qualitatively similar: the most probable value of R_{corr} (≈ 0.15) matches within 10% and the medians are

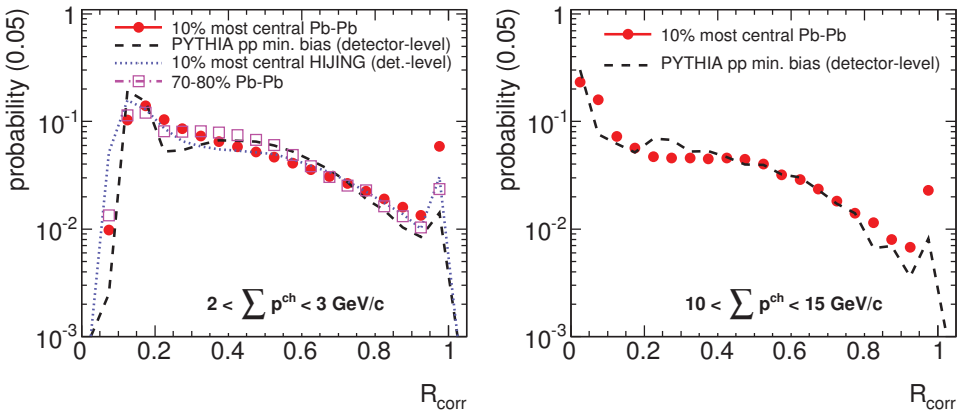

Fig. 80. Probability distribution of R_{corr} (Eq. (18)) in two different intervals of Σ_{p}, measured in central (0–10%) and peripheral (70–80%, left panel only) Pb–Pb collisions. Also shown are detector-level simulations for MB pp collisions based on PYTHIA (same distributions as Fig. 75), and for central Pb–Pb collisions based on HIJING (left panel only).

compatible within 4%. In the left panel, for $2 < \Sigma_{\mathrm{p}} < 3$ GeV, the peripheral Pb–Pb distribution does not match that for pp in detail at (and slightly above) the minimum ionizing particle (MIP) peak. The probability at the saturation peak, $R_{\mathrm{corr}} = 1$, is largest for central Pb–Pb, with lower probability for peripheral Pb–Pb, and even lower for pp. This is due to a larger contribution from cluster pileup, which increases the probability for large cluster energy. However, the increase in probability for the saturation peak from peripheral to central collisions is seen to be only 3%. Since the probability is normalized to unity, this difference between the systems at $R_{\mathrm{corr}} = 1$ must be accompanied by differences for $R_{\mathrm{corr}} < 1$, which are visible but are of moderate magnitude. The Hijing simulation models the R_{corr} distribution for central collisions reasonably well, though its estimate of the probability for $R_{\mathrm{corr}} = 1$ is lower than seen in data, and it undershoots the data slightly in the region just above the MIP peak.

The right panel in Fig. 80, for $10 < \Sigma_{\mathrm{p}} < 15$ GeV (and correspondingly for more energetic EMCal clusters), also exhibits minor differences between R_{corr} distributions in central Pb–Pb and pp. Since the magnitude of cluster pileup energy is independent of the true cluster energy, its relative effect on the R_{corr} probability distribution is expected to be smaller for larger cluster energy.

The above observations indicate that the magnitude of cluster pileup effects in central Pb–Pb collisions due to neutral particles and unmeasured charged particles is modest. While the pileup contribution cannot be measured explicitly on a cluster-by-cluster basis, its average magnitude can be estimated, based on the distributions in Fig. 80, to correspond to about 50 MeV of additional energy per EMCal tower for central Pb–Pb relative to pp collisions. However, subtraction of this average value from each tower in a cluster does not improve the overall agreement of the distributions in Fig. 80, and such a correction is not applied in the physics analysis

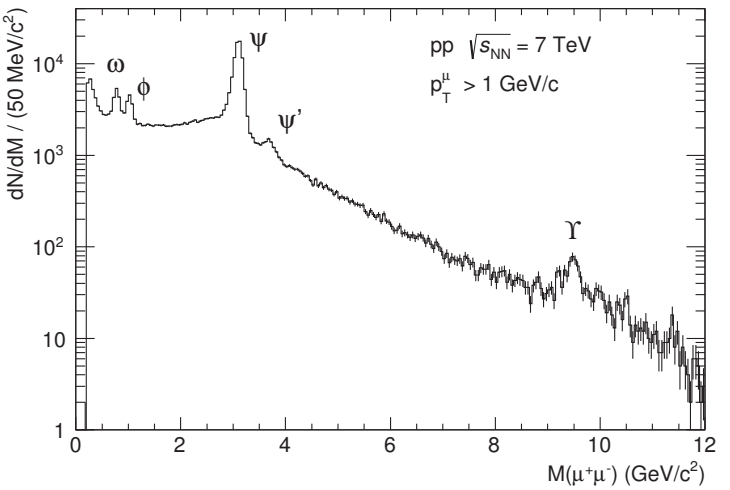

Fig. 81. Invariant mass distribution of $\mu^+\mu^-$ pairs measured by ALICE for pp collisions at $\sqrt{s} = 7$ TeV ($\mathcal{L} = 1.35$ pb^{-1}, corresponding to the full 2011 dimuon-triggered data sample).

of jets. Rather, the difference between the distributions is incorporated into the systematic uncertainty of the measurement.

11. Muons

Light (ω and ϕ) and heavy (J/ψ and Υ families) vector mesons are measured in ALICE in their $\mu^+\mu^-$ decay channel using the muon spectrometer. The invariant mass reach with the statistics collected in one year of running with pp collisions is illustrated in Fig. 81. The spectrometer is also used to measure the production of single muons from decays of heavy-flavor hadrons[105] and W$^\pm$ bosons. Below we discuss the performance of the spectrometer, with an emphasis on the J/ψ measurement.

The muon spectrometer covers $-4.0 < \eta < -2.5$ and consists of the following components: a passive front absorber (4.13 m, $\sim 10\ \lambda_{\rm int}$, $\sim 60\ X_0$) suppressing charged hadrons and muons from π/K decays; a high-granularity tracking system of ten detection planes (five stations, two Cathode Pad Chambers each); a large dipole magnet ($\int B\,{\rm d}z = 3$ Tm, bending tracks vertically); a passive muon-filter wall (1.2 m thick, $\sim 7.2\ \lambda_{\rm int}$) followed by four planes of Resistive Plate Chambers for triggering; and inner beam shielding to protect the detection chambers from the primary and secondary particles produced at large rapidities.

The key features of the muon spectrometer are good J/ψ acceptance down to $p_{\rm T} = 0$ and high readout granularity resulting in an occupancy of 2% in central Pb–Pb collisions. The combined effect of the front absorber (which stops primary hadrons) and of the muon-filter wall (which suppresses the low-momentum muons from pion and kaon decays) leads to a detection threshold of $p \gtrsim 4$ GeV/c for tracks matching the trigger.

During the heavy-ion run in 2011, about 20% of the electronic channels in the tracking chambers had to be discarded because of faulty electronics or high voltage instabilities. In a similar way, the noisy strips in the trigger chambers (0.3%)[106] have also been excluded from data taking.

The clusters of charge deposited by the particles crossing the muon tracking chambers are unfolded using the Maximum Likelihood Expectation Maximization (MLEM) algorithm[107] and fitted with a 2D Mathieson[108] function to determine their spatial location. A tracking algorithm based on the Kalman filter reconstructs the trajectory of the particles across the five tracking stations. These tracks are then extrapolated to the vertex position measured by the ITS (SPD only in most cases) and their kinematic parameters are further corrected for multiple scattering and energy loss of muons in the front absorber.[109]

While the actual detector occupancy measured in real Pb–Pb collisions, 2%, is well below the design value (5%), it was still important to fine tune the reconstruction parameters to keep the fraction of fake tracks as low as possible. The size of the roads (defined in the tracking algorithm that searches for new clusters to be attached to the track candidates) is limited by the intrinsic cluster resolution and the precision of the alignment of the apparatus.

Since the background in Pb–Pb collisions is large, tight selection criteria have to be imposed on single muon tracks in order to preserve the purity of the muon sample. Tracks reconstructed in the tracking chambers are required to match a trigger track, they must lie within the pseudorapidity range $-4 < \eta < -2.5$, and their transverse radius coordinate at the end of the front absorber must be in the range 17.6 cm $< R_{\rm abs} <$ 89 cm. An additional cut on $p \times$ DCA, the product of the track momentum and the distance between the vertex and the track extrapolated to the vertex transverse plane, may also be applied to further reduce residual contamination. With such cuts, a large fraction of the remaining fake tracks are removed.

11.1. *Reconstruction efficiency*

The track reconstruction efficiency (Fig. 82) is determined with experimental data using a method that takes advantage of the redundancy of the detector, i.e. the fact that a subset of all chambers is sufficient for a track to be reconstructed. The tracking algorithm requires at least one cluster in each of the first three stations and at least three clusters in three different chambers in the last two stations in order to validate a track. As a result, the efficiency of a given chamber can be determined by the ratio of the number of reconstructed tracks detected in that chamber over the total number of reconstructed tracks. In order to avoid any bias that may be introduced by the reconstruction criteria themselves, only tracks that still satisfy these criteria when that chamber is not taken into account must be considered when computing the ratio. For instance, in the first station, the efficiency of one of the two chambers is determined by dividing the number of tracks detected in both

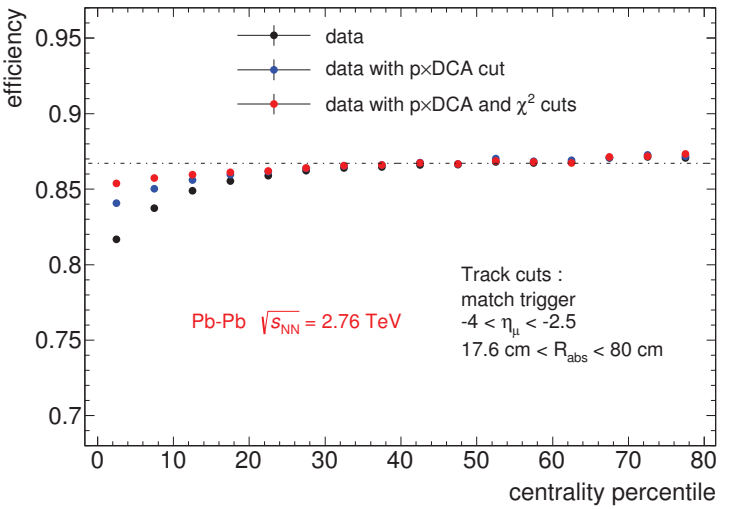

Fig. 82. (Color online) Measured muon track reconstruction efficiency in Pb–Pb collisions as a function of the collision centrality.

chambers by the number of tracks detected by the other chamber. By combining the individual chamber efficiencies according to the reconstruction criteria, one can determine the overall reconstruction efficiency.

The resulting efficiency (black points in Fig. 82) exhibits a drop for central Pb–Pb collisions. This drop can, however, be largely ascribed to the remaining fake tracks, which inherently contain less clusters than the others. To cure this problem, the $p \times \mathrm{DCA}$ cut is applied first, strongly reducing this contamination (blue points in Fig. 82). Then a second cut on the normalized χ^2 of the tracks ($\chi^2 < 3.5$) is added to further cut the remaining contamination at very low p_{T} (< 1–2 GeV/c), where the $p \times \mathrm{DCA}$ cut is not 100% efficient (red points on the figure). After all these cuts have been applied, the relative loss of efficiency as a function of centrality is very low (of the order of 1.5% in the centrality bin 0–10%).

The product of acceptance A and efficiency ϵ for measuring J/ψ mesons emitted within $-4.0 < y < -2.5$, obtained from Monte Carlo (MC) simulations of pure J/ψ signal with input y and p_{T} distributions tuned to the measured ones, is sizable down to $p_{\mathrm{T}} = 0$. The transverse momentum dependence (for J/ψ within $-4.0 < y < -2.5$) and the rapidity dependence (for a realistic p_{T} distribution) of this quantity are shown in Fig. 83.

11.2. *Trigger efficiency*

While it has been verified with data that the efficiency of the trigger chambers themselves does not vary with the centrality of the collision, the overall reconstruction efficiency of the trigger tracks can do so. The reason is that the trigger algorithm can only produce one trigger track per local board, and the detector is divided into

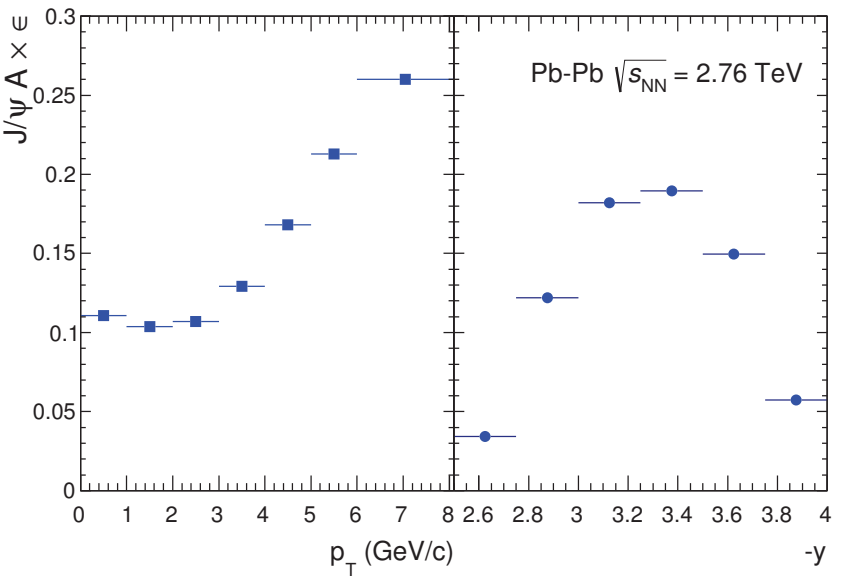

Fig. 83. Muon spectrometer acceptance times efficiency for J/ψ within $-4.0 < y < -2.5$ during the Pb–Pb 2011 campaign, as a function of the J/ψ transverse momentum (left) or rapidity (right).

234 local boards. So even if the occupancy in the trigger system is small, the probability that two tracks are close enough to interfere in the trigger response can be sizable. The response of the algorithm, taking this effect into account, is nevertheless well reproduced in simulations using the embedding technique (see below). In these simulations we observe a relative loss of trigger track reconstruction efficiency of 3.5% in the most central collisions.

The trigger used for J/ψ measurements[110] in the 2011 Pb–Pb run was an unlike-sign dimuon trigger (MUL) with a p_{T} threshold of 1 GeV/c for each muon. The centrality-integrated efficiency of this trigger for J/ψ is shown in Fig. 84 as a function of the J/ψ transverse momentum. The trigger efficiency is evaluated via a MC simulation having as input the trigger chamber efficiency, determined from experimental data.[106] In order to separate the detector efficiency from acceptance effects, the simulation was also run assuming a chamber efficiency of 100%. The effect of the trigger chamber inefficiencies is smaller than 5%, with weak (if any) p_{T} dependence.

11.3. *Invariant-mass resolution*

The momentum resolution of the muon spectrometer crucially depends on the detector alignment. Each of the 156 detection elements of the muon spectrometer's tracking chambers has six spatial degrees of freedom, three translations and three rotations. In addition, since the detection elements are mounted in independent support structures, six further degrees of freedom per half-chamber need to be considered. The initial position of the (half-)chambers was measured by the CERN

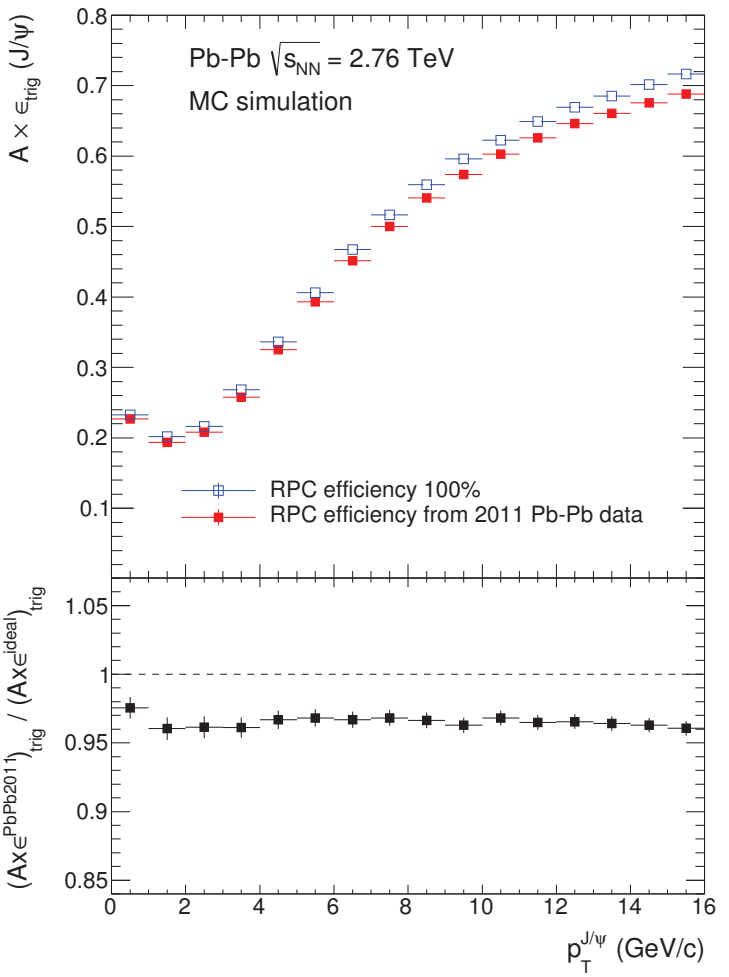

Fig. 84. Unlike-sign dimuon trigger efficiency for J/ψ, calculated using a realistic (filled squares) and ideal (open squares) chamber efficiency. The ratio of the two curves is shown in the bottom panel.

survey group with about 1 mm resolution in three directions. The displacements of the (half-)chambers relative to a reference chamber has been monitored by the Geometry Monitoring System (GMS)[43] with about 40 μm resolution in three directions. The optimal method for aligning the tracking detectors is to use reconstructed tracks taken with and without magnetic field and perform a least-square minimization of the cluster-to-track residuals with respect to the alignment and the track parameters simultaneously. A special computation-efficient implementation[111] allowed the minimization to be performed on a sample of 500000 tracks, which corresponded to a few hours of data taking. The resulting alignment resolution was ~ 100 μm.

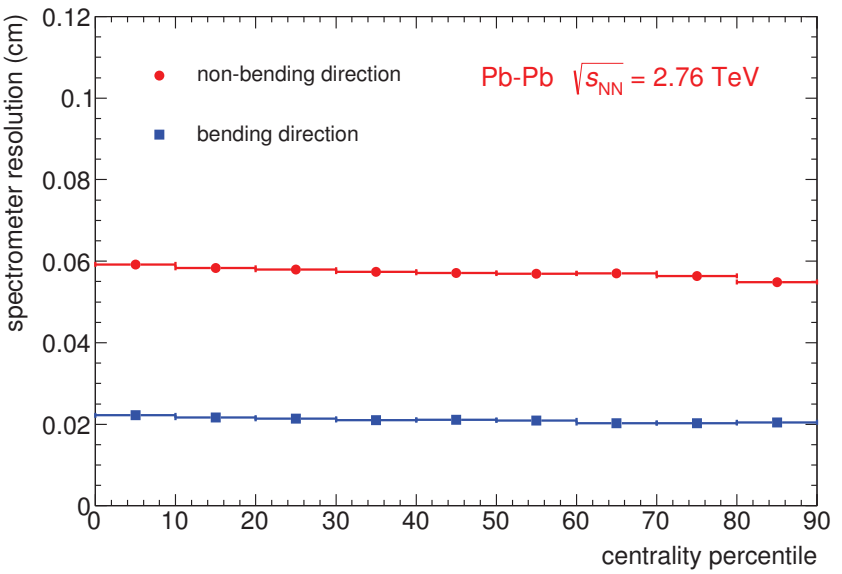

Fig. 85. Muon spectrometer resolution measured as a function of the centrality of the collision. The main contributions come from the cluster resolution and the residual misalignment of the tracking chambers.

The overall detector resolution, including the cluster resolution and the residual misalignment, can be measured using the distance between the position of the clusters and the position of the reconstructed tracks they belong to. Within chambers it ranges between 450 and 800 μm in the nonbending direction, and between 100 and 400 μm in the bending direction. The degradation in resolution due to the large occupancy in central heavy ion collisions is less than 5% (Fig. 85).

To extract the invariant mass distributions of muon pairs in Pb–Pb collisions, the standard track cuts previously described (trigger matching, $R_{\rm abs}$ and pseudo-rapidity cuts) are applied to both muon tracks. The J/ψ peak in the $\mu^+\mu^-$ invariant mass spectra can be fitted by an extended Crystal Ball function[50] (Fig. 86). The mass resolution at the J/ψ peak in central Pb–Pb collisions, $\sim$73 MeV/c^2, is in agreement with the design value. An analogous fit of the Υ peak in minimum-bias Pb–Pb collisions yields a mass resolution of 147 ± 27 MeV/c^2. This is shown in Fig. 87, representing the full statistics of the 2011 run. The mass resolution, in general, is determined by multiple scattering and energy loss in the front absorber, intrinsic spatial resolution of the chambers, and alignment. At the J/ψ and Υ peaks the resolution is dominated by multiple scattering in the front absorber and the overall detector resolution, respectively.

The aforementioned increase of the detector occupancy with the centrality of the collision could alter the shape of the J/ψ mass peak. This effect has been studied using a Monte Carlo embedding procedure, in which a simulated signal particle (a J/ψ in our case) is embedded into a real raw-data event. The embedded event is

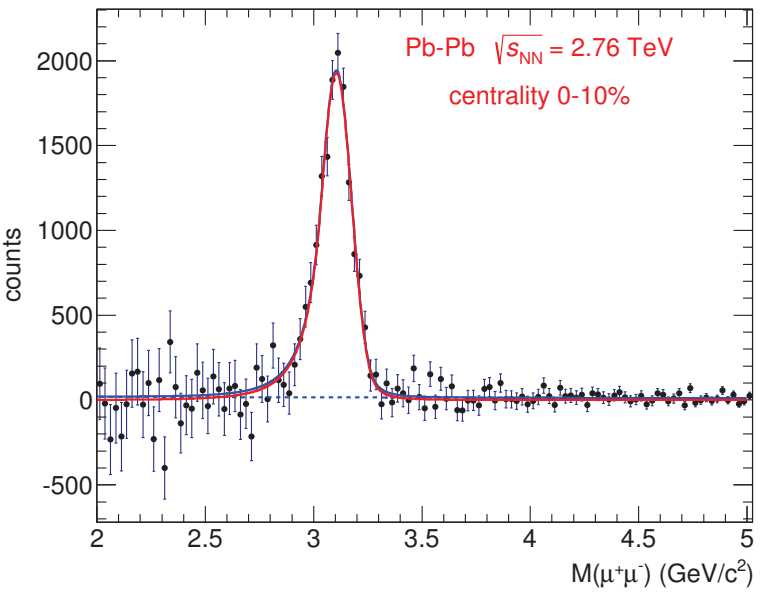

Fig. 86. Invariant-mass distribution of $\mu^+\mu^-$ pairs in 0–10% most central Pb–Pb collisions at $\sqrt{s_{\rm NN}} = 2.76$ TeV with the J/ψ peak fitted by an extended Crystal Ball function. The combinatorial background was determined by the event mixing method and subtracted.

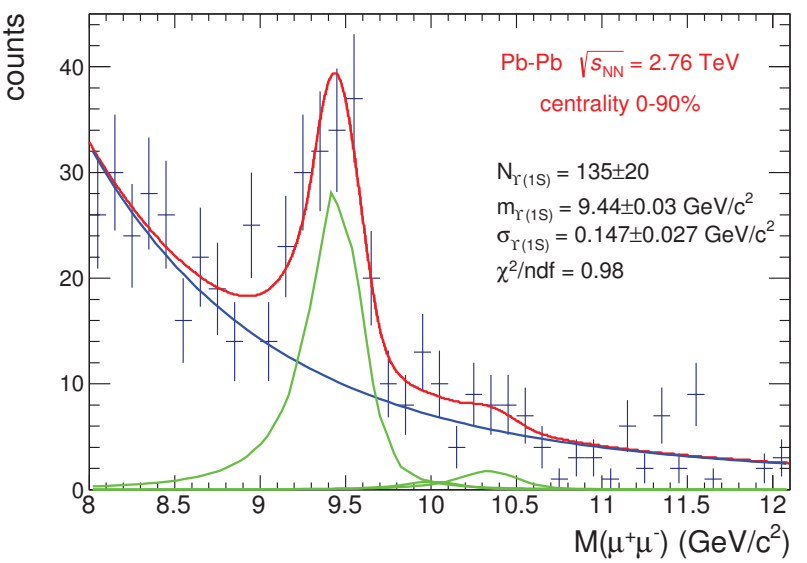

Fig. 87. Invariant-mass distribution of $\mu^+\mu^-$ pairs in Pb–Pb collisions at $\sqrt{s_{\rm NN}} = 2.76$ TeV with the $\Upsilon(1S)$, $\Upsilon(2S)$, and $\Upsilon(3S)$ peaks fitted by the sum of three extended Crystal Ball functions with identical relative widths and identical relative displacements from the PDG mass values. The tail shape is fixed by the embedding-MC simulation and the combinatorial background is parametrized by an exponential.

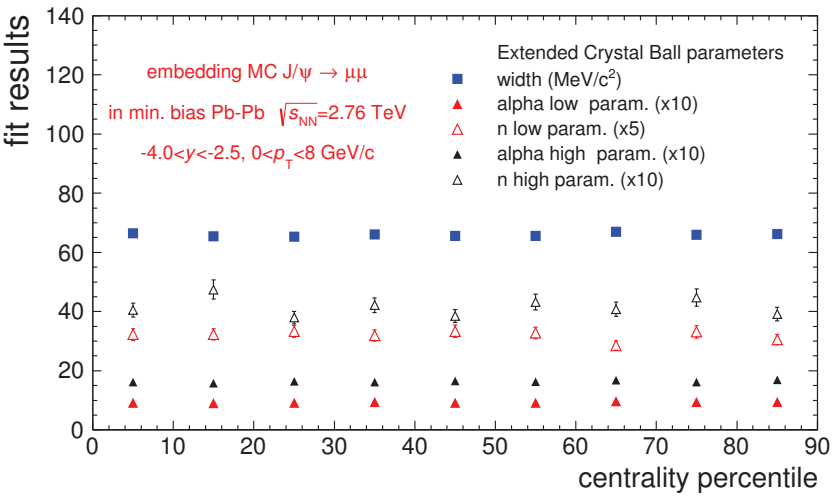

Fig. 88. Centrality dependence of J/ψ invariant mass fit parameters.

then reconstructed as if it were a real event. This technique has the advantage of providing the most realistic background conditions. With such a technique it was shown (Fig. 88) that the J/ψ signal fit parameters do not depend on centrality. The peak widths obtained from the simulation agree within errors (from 3% for central collisions to 10% for the most peripheral ones) with those observed in experimental data. The same embedding technique has also been used to confirm the small drop in the track reconstruction efficiency for the most central collisions mentioned above.

12. Conclusion and Outlook

ALICE recorded data for all collision systems and energies offered by the Large Hadron Collider in its first running period from 2009 to 2013. The performance of the experiment was in good agreement with expectations. This is shown in Table 11 where, for selected parameters, the achieved performance is compared to the expectations contained in the ALICE Physics Performance Report from 2006.[2]

ALICE measurements during the full-energy LHC Run 2 (2015–2017) will, on one hand, focus on low-p_{T} observables where triggering is not possible. The goal here is to increase the statistics to $\sim$500 million minimum bias Pb–Pb events. Concerning rare probes, it is planned to inspect 1 nb^{-1} Pb–Pb interactions in the rare-trigger running mode. This requires increasing the collision rates to 10–20 kHz, for which consolidation work is ongoing. The TPC electronics will be upgraded and the maximum readout rate of this detector will be doubled. The completion of TRD and PHOS, and extension of EMCal by adding calorimeter modules on the opposite side (Di-Jet Calorimeter, DCal)[112] are other important ingredients of the preparation for Run 2.

Table 11. Selection of parameters characterizing the performance of the ALICE experiment in Run 1 of the LHC. The expectations published in 2006 in the ALICE PPR[2] (column 2) and the achieved performance (column 3) are compared. For the vertex resolution, the approximation $\mathrm{d}N_{\mathrm{ch}}/\mathrm{d}y \equiv \mathrm{d}N_{\mathrm{ch}}/\mathrm{d}\eta$ is used.

Parameter	Expected	Achieved
Event vertex resolution with ITS–TPC tracks		
vertex resolution at $\mathrm{d}N_{\mathrm{ch}}/\mathrm{d}\eta = 5$, transverse	85 μm	97 μm
vertex resolution at $\mathrm{d}N_{\mathrm{ch}}/\mathrm{d}\eta = 25$, transverse	35 μm	32 μm
DCA resolution of ITS–TPC tracks in central Pb–Pb collisions		
transverse DCA resolution at $p_{\mathrm{T}} = 0.3$ GeV/c	200 μm	200 μm
transverse DCA resolution at $p_{\mathrm{T}} = 3$ GeV/c	30 μm	30 μm
transverse DCA resolution at $p_{\mathrm{T}} = 20$ GeV/c	15 μm	15 μm
DCA resolution of ITS–TPC tracks in pp collisions (*including vertex resolution*)		
transverse DCA resolution at $p_{\mathrm{T}} = 0.2$ GeV/c	300 μm	300 μm
transverse DCA resolution at $p_{\mathrm{T}} = 3$ GeV/c	50 μm	45 μm
transverse DCA resolution at $p_{\mathrm{T}} = 30$ GeV/c	25 μm	20 μm
Barrel tracking efficiency in central Pb–Pb collisions		
TPC track finding efficiency at $p_{\mathrm{T}} > 0.2$ GeV/c	$> 78\%$ [a]	$> 70\%$
TPC track finding efficiency at $p_{\mathrm{T}} > 1.0$ GeV/c	$> 90\%$ [a]	$> 78\%$
ITS matching efficiency at $p_{\mathrm{T}} > 0.2$ GeV/c	$> 95\%$	$> 92\%$
Barrel p_{T} resolution		
$\Delta p_{\mathrm{T}}/p_{\mathrm{T}}$ of TPC tracks at $p_{\mathrm{T}} = 10$ GeV/c	4–6%	6%
$\Delta p_{\mathrm{T}}/p_{\mathrm{T}}$ of TPC tracks at $p_{\mathrm{T}} = 30$ GeV/c	10–15%	18%
$\Delta p_{\mathrm{T}}/p_{\mathrm{T}}$ of ITS–TPC tracks at $p_{\mathrm{T}} = 10$ GeV/c	1–2%	1.5%
$\Delta p_{\mathrm{T}}/p_{\mathrm{T}}$ of ITS–TPC tracks at $p_{\mathrm{T}} = 30$ GeV/c	2–3%	2.5%
Barrel particle identification		
TPC $\mathrm{d}E/\mathrm{d}x$ resolution in pp	5.4%	5.2%
TPC $\mathrm{d}E/\mathrm{d}x$ resolution in central Pb–Pb	6.8%	6.5%
TOF resolution	60–110 ps	80 ps
T0 resolution	15–50 ps	21 ps
Muon spectrometer		
MUON track finding efficiency	95%	85–87%
invariant mass resolution at J/ψ peak in central Pb–Pb	70–74 MeV/c^2	73 MeV/c^2
invariant mass resolution at Υ peak in central Pb–Pb	99–115 MeV/c^2	147 (27) MeV/c^2

[a]Without track quality cuts.

In Run 3 (after 2018), the LHC will provide Pb–Pb collisions at a rate of 50 kHz. With the planned continuous readout of the ALICE TPC, the statistics available for data analysis could be increased compared to Run 2 by two orders of magnitude. To achieve this, the ALICE Collaboration has presented a plan to upgrade its detector systems. The current ITS will be replaced and the overall rate capabilities of the experiment will be enhanced. The goal is to have sampled, by the mid-2020s, an integrated luminosity of 10 nb^{-1}. In addition, three new detectors have been proposed. For more information, the reader is referred to the upgrade documents cited in Table 12.

Table 12. ALICE upgrades considered for the time after Run 2.

System	Upgrade	Documents
ITS	Reduced material, improved resolution, topological trigger at L2	CDR,[113] LoI,[114] TDR[115]
TPC	Faster gas, GEM readout chambers, new readout electronics, continuous readout	LoI,[114] TDR[116]
Trigger/readout	Fast readout of ITS, TPC, TRD, TOF, EMCal, PHOS, MTR, MCH, and ZDC; replacing T0/V0/FMT with a new detector FIT; new trigger system	LoI,[114] TDR[117]
O^2	New combined DAQ, HLT, and offline computing system for high-rate and continuous readout	LoI[114]
MFT	Muon Forward Tracker, pixel Si before absorber, $-4 < \eta < -2.5$, better resolution and S/B for heavy flavors	Addendum to LoI[118]
VHMPID	Very High Momentum PID, gas Cherenkov, π/K/p separation in $5 < p < 25$ GeV/c	Ref. 119
FoCal	Forward EM Calorimeter, W+Si $2.5 < \eta < 4.5$, γ/π discrimination	Ref. 120

Acknowledgments

The ALICE Collaboration would like to thank all its engineers and technicians for their invaluable contributions to the construction of the experiment and the CERN accelerator teams for the outstanding performance of the LHC complex. The ALICE Collaboration gratefully acknowledges the resources and support provided by all Grid centres and the Worldwide LHC Computing Grid (WLCG) collaboration. The ALICE Collaboration acknowledges the following funding agencies for their support in building and running the ALICE detector: State Committee of Science, World Federation of Scientists (WFS) and Swiss Fonds Kidagan, Armenia, Conselho Nacional de Desenvolvimento Científico e Tecnológico (CNPq), Financiadora de Estudos e Projetos (FINEP), Fundação de Amparo à Pesquisa do Estado de São Paulo (FAPESP); National Natural Science Foundation of China (NSFC), the Chinese Ministry of Education (CMOE) and the Ministry of Science and Technology of China (MSTC); Ministry of Education and Youth of the Czech Republic; Danish Natural Science Research Council, the Carlsberg Foundation and the Danish National Research Foundation; The European Research Council under the European Community's Seventh Framework Programme; Helsinki Institute of Physics and the Academy of Finland; French CNRS-IN2P3, the "Region Pays de Loire," "Region Alsace," "Region Auvergne" and CEA, France; German BMBF and the Helmholtz Association; General Secretariat for Research and Technology, Ministry of Development, Greece; Hungarian OTKA and National Office for Research and Technology (NKTH); Department of Atomic Energy and Department of Science and Technology of the Government of India; Istituto Nazionale di Fisica Nucleare (INFN) and Centro Fermi — Museo Storico della Fisica e Centro

Studi e Ricerche "Enrico Fermi," Italy; MEXT Grant-in-Aid for Specially Promoted Research, Japan; Joint Institute for Nuclear Research, Dubna; National Research Foundation of Korea (NRF); CONACYT, DGAPA, México, ALFA-EC and the EPLANET Program (European Particle Physics Latin American Network) Stichting voor Fundamenteel Onderzoek der Materie (FOM) and the Nederlandse Organisatie voor Wetenschappelijk Onderzoek (NWO), Netherlands; Research Council of Norway (NFR); Polish Ministry of Science and Higher Education; National Science Centre, Poland; Ministry of National Education/Institute for Atomic Physics and CNCS-UEFISCDI — Romania; Ministry of Education and Science of Russian Federation, Russian Academy of Sciences, Russian Federal Agency of Atomic Energy, Russian Federal Agency for Science and Innovations and The Russian Foundation for Basic Research; Ministry of Education of Slovakia; Department of Science and Technology, South Africa; CIEMAT, EELA, Ministerio de Economía y Competitividad (MINECO) of Spain, Xunta de Galicia (Consellería de Educación), CEADEN, Cubaenergía, Cuba, and IAEA (International Atomic Energy Agency); Swedish Research Council (VR) and Knut & Alice Wallenberg Foundation (KAW); Ukraine Ministry of Education and Science; United Kingdom Science and Technology Facilities Council (STFC); The United States Department of Energy, the United States National Science Foundation, the State of Texas, and the State of Ohio.

Appendix A. The ALICE Collaboration

B. Abelev,[71] A. Abramyan,[1] J. Adam,[37] D. Adamová,[79] M. M. Aggarwal,[83] M. Agnello,[90,107] A. Agostinelli,[26] N. Agrawal,[44] Z. Ahammed,[126] N. Ahmad,[18] A. Ahmad Masoodi,[18] I. Ahmed,[15] S. U. Ahn,[64] S. A. Ahn,[64] I. Aimo,[90,107] S. Aiola,[131] M. Ajaz,[15] A. Akindinov,[54] D. Aleksandrov,[96] B. Alessandro,[107] D. Alexandre,[98] A. Alici,[101,12] A. Alkin,[3] J. Alme,[35] T. Alt,[39] V. Altini,[31] S. Altinpinar,[17] I. Altsybeev,[125] C. Alves Garcia Prado,[115] C. Andrei,[74] A. Andronic,[93] V. Anguelov,[89] J. Anielski,[50] T. Antičić,[94] F. Antinori,[104] P. Antonioli,[101] L. Aphecetche,[109] H. Appelshäuser,[49] N. Arbor,[67] S. Arcelli,[26] N. Armesto,[16] R. Arnaldi,[107] T. Aronsson,[131] I. C. Arsene,[21,93] M. Arslandok,[49] A. Augustinus,[34] R. Averbeck,[93] T. C. Awes,[80] M. D. Azmi,[18,85] M. Bach,[39] A. Badalà,[103] Y. W. Baek,[40,66] S. Bagnasco,[107] R. Bailhache,[49] R. Bala,[86] A. Baldisseri,[14] F. Baltasar Dos Santos Pedrosa,[34] R. C. Baral,[57] R. Barbera,[27] F. Barile,[31] G. G. Barnaföldi,[130] L. S. Barnby,[98] V. Barret,[66] J. Bartke,[112] M. Basile,[26] N. Bastid,[66] S. Basu,[126] B. Bathen,[50] G. Batigne,[109] B. Batyunya,[62] P. C. Batzing,[21] C. Baumann,[49] I. G. Bearden,[76] H. Beck,[49] C. Bedda,[90] N. K. Behera,[44] I. Belikov,[51] F. Bellini,[26] R. Bellwied,[117] E. Belmont-Moreno,[60] G. Bencedi,[130] S. Beole,[25] I. Berceanu,[74] A. Bercuci,[74] Y. Berdnikov,[ii,81] D. Berenyi,[130] M. E. Berger,[88] R. A. Bertens,[53] D. Berzano,[25] L. Betev,[34] A. Bhasin,[86] A. K. Bhati,[83] B. Bhattacharjee,[41] J. Bhom,[122] L. Bianchi,[25] N. Bianchi,[68] C. Bianchin,[53] J. Bielčík,[37] J. Bielčíková,[79] A. Bilandzic,[76] S. Bjelogrlic,[53] F. Blanco,[10] D. Blau,[96] C. Blume,[49] F. Bock,[89,70]

A. Bogdanov,[72] H. Bøggild,[76] M. Bogolyubsky,[108] F. V. Böhmer,[88]
L. Boldizsár,[130] M. Bombara,[38] J. Book,[49] H. Borel,[14] A. Borissov,[129,92]
F. Bossú,[61] M. Botje,[77] E. Botta,[25] S. Böttger,[48] P. Braun-Munzinger,[93]
M. Bregant,[115] T. Breitner,[48] T. A. Broker,[49] T. A. Browning,[91] M. Broz,[37,36]
E. Bruna,[107] G. E. Bruno,[31] D. Budnikov,[95] H. Buesching,[49] S. Bufalino,[107]
P. Buncic,[34] O. Busch,[89] Z. Buthelezi,[61] D. Caffarri,[28] X. Cai,[7] H. Caines,[131]
A. Caliva,[53] E. Calvo Villar,[99] P. Camerini,[24] V. Canoa Roman,[34] F. Carena,[34]
W. Carena,[34] J. Castillo Castellanos,[14] E. A. R. Casula,[23] V. Catanescu,[74]
C. Cavicchioli,[34] C. Ceballos Sanchez,[9] J. Cepila,[37] P. Cerello,[107] B. Chang,[118]
S. Chapeland,[34] J. L. Charvet,[14] S. Chattopadhyay,[126] S. Chattopadhyay,[97]
M. Cherney,[82] C. Cheshkov,[124] B. Cheynis,[124] V. Chibante Barroso,[34]
D. D. Chinellato,[117,116] P. Chochula,[34] M. Chojnacki,[76] S. Choudhury,[126]
P. Christakoglou,[77] C. H. Christensen,[76] P. Christiansen,[32] T. Chujo,[122]
S. U. Chung,[92] C. Cicalo,[102] L. Cifarelli,[12,26] F. Cindolo,[101] J. Cleymans,[85]
F. Colamaria,[31] D. Colella,[31] A. Collu,[23] M. Colocci,[26] G. Conesa Balbastre,[67]
Z. Conesa del Valle,[47] M. E. Connors,[131] J. G. Contreras,[11] T. M. Cormier,[80,129]
Y. Corrales Morales,[25] P. Cortese,[30] I. Cortés Maldonado,[2]
M. R. Cosentino,[115,70] F. Costa,[34] P. Crochet,[66] R. Cruz Albino,[11]
E. Cuautle,[59] L. Cunqueiro,[68,34] A. Dainese,[104] R. Dang,[7] A. Danu,[58] D. Das,[97]
I. Das,[47] K. Das,[97] S. Das,[4] A. Dash,[116] S. Dash,[44] S. De,[126] H. Delagrange,[109,i]
A. Deloff,[73] E. Dénes,[130] G. D'Erasmo,[31] A. De Caro,[29,12] G. de Cataldo,[100]
J. de Cuveland,[39] A. De Falco,[23] D. De Gruttola,[29,12] N. De Marco,[107]
S. De Pasquale,[29] R. de Rooij,[53] M. A. Diaz Corchero,[10] T. Dietel,[50,85]
R. Divià,[34] D. Di Bari,[31] S. Di Liberto,[105] A. Di Mauro,[34] P. Di Nezza,[68]
Ø. Djuvsland,[17] A. Dobrin,[53] T. Dobrowolski,[73] D. Domenicis Gimenez,[115]
B. Dönigus,[49] O. Dordic,[21] S. Dørheim,[88] A. K. Dubey,[126] A. Dubla,[53]
L. Ducroux,[124] P. Dupieux,[66] A. K. Dutta Majumdar,[97] R. J. Ehlers,[131]
D. Elia,[100] H. Engel,[48] B. Erazmus,[34,109] H. A. Erdal,[35] D. Eschweiler,[39]
B. Espagnon,[47] M. Esposito,[34] M. Estienne,[109] S. Esumi,[122] D. Evans,[98]
S. Evdokimov,[108] D. Fabris,[104] J. Faivre,[67] D. Falchieri,[26] A. Fantoni,[68]
M. Fasel,[89] D. Fehlker,[17] L. Feldkamp,[50] D. Felea,[58] A. Feliciello,[107]
G. Feofilov,[125] J. Ferencei,[79] A. Fernández Téllez,[2] E. G. Ferreiro,[16]
A. Ferretti,[25] A. Festanti,[28] J. Figiel,[112] M. A. S. Figueredo,[119] S. Filchagin,[95]
D. Finogeev,[52] F. M. Fionda,[31,100] E. M. Fiore,[31] E. Floratos,[84] M. Floris,[34]
S. Foertsch,[61] P. Foka,[93] S. Fokin,[96] E. Fragiacomo,[106] A. Francescon,[28,34]
U. Frankenfeld,[93] U. Fuchs,[34] C. Furget,[67] M. Fusco Girard,[29] J. J. Gaardhøje,[76]
M. Gagliardi,[25] A. M. Gago,[99] M. Gallio,[25] D. R. Gangadharan,[19,70]
P. Ganoti,[84,80] C. Garabatos,[93] E. Garcia-Solis,[13] C. Gargiulo,[34] I. Garishvili,[71]
J. Gerhard,[39] M. Germain,[109] A. Gheata,[34] M. Gheata,[34,58] B. Ghidini,[31]
P. Ghosh,[126] S. K. Ghosh,[4] P. Gianotti,[68] P. Giubellino,[34]
E. Gladysz-Dziadus,[112] P. Glässel,[89] R. Gomez,[11] A. Gomez Ramirez,[48]
P. González-Zamora,[10] S. Gorbunov,[39] L. Görlich,[112] S. Gotovac,[111]
L. K. Graczykowski,[128] R. Grajcarek,[89] A. Grelli,[53] A. Grigoras,[34]

C. Grigoras,[34] V. Grigoriev,[72] A. Grigoryan,[1] S. Grigoryan,[62] B. Grinyov,[3]
N. Grion,[106] J. F. Grosse-Oetringhaus,[34] J.-Y. Grossiord,[124] R. Grosso,[34]
F. Guber,[52] R. Guernane,[67] B. Guerzoni,[26] M. Guilbaud,[124] K. Gulbrandsen,[76]
H. Gulkanyan,[1] T. Gunji,[121] A. Gupta,[86] R. Gupta,[86] K. H. Khan,[15]
R. Haake,[50] Ø. Haaland,[17] C. Hadjidakis,[47] M. Haiduc,[58] H. Hamagaki,[121]
G. Hamar,[130] L. D. Hanratty,[98] A. Hansen,[76] J. W. Harris,[131] H. Hartmann,[39]
A. Harton,[13] D. Hatzifotiadou,[101] S. Hayashi,[121] S. T. Heckel,[49] M. Heide,[50]
H. Helstrup,[35] A. Herghelegiu,[74] G. Herrera Corral,[11] B. A. Hess,[33]
K. F. Hetland,[35] B. Hicks,[131] B. Hippolyte,[51] J. Hladky,[56] P. Hristov,[34]
M. Huang,[17] T. J. Humanic,[19] D. Hutter,[39] D. S. Hwang,[20] R. Ilkaev,[95]
I. Ilkiv,[73] M. Inaba,[122] G. M. Innocenti,[25] C. Ionita,[34] M. Ippolitov,[96]
M. Irfan,[18] M. Ivanov,[93] V. Ivanov,[81] O. Ivanytskyi,[3] A. Jachołkowski,[27]
P. M. Jacobs,[70] C. Jahnke,[115] H. J. Jang,[64] M. A. Janik,[128]
P. H. S. Y. Jayarathna,[117] S. Jena,[117] R. T. Jimenez Bustamante,[59]
P. G. Jones,[98] H. Jung,[40] A. Jusko,[98] S. Kalcher,[39] P. Kalinak,[55] A. Kalweit,[34]
J. Kamin,[49] J. H. Kang,[132] V. Kaplin,[72] S. Kar,[126] A. Karasu Uysal,[65]
O. Karavichev,[52] T. Karavicheva,[52] E. Karpechev,[52] U. Kebschull,[48]
R. Keidel,[133] B. Ketzer,[88] M. M. Khan,[iii,18] P. Khan,[97] S. A. Khan,[126]
A. Khanzadeev,[81] Y. Kharlov,[108] B. Kileng,[35] B. Kim,[132] D. W. Kim,[64,40]
D. J. Kim,[118] J. S. Kim,[40] M. Kim,[40] M. Kim,[132] S. Kim,[20] T. Kim,[132]
S. Kirsch,[39] I. Kisel,[39] S. Kiselev,[54] A. Kisiel,[128] G. Kiss,[130] J. L. Klay,[6]
J. Klein,[89] C. Klein-Bösing,[50] A. Kluge,[34] M. L. Knichel,[93,89] A. G. Knospe,[113]
C. Kobdaj,[34,110] M. Kofarago,[34] M. K. Köhler,[93] T. Kollegger,[39]
A. Kolojvari,[125] V. Kondratiev,[125] N. Kondratyeva,[72] A. Konevskikh,[52]
V. Kovalenko,[125] M. Kowalski,[34,112] S. Kox,[67] G. Koyithatta Meethaleveedu,[44]
J. Kral,[118] I. Králik,[55] F. Kramer,[49] A. Kravčáková,[38] M. Krelina,[37] M. Kretz,[39]
M. Krivda,[98,55] F. Krizek,[79] M. Krus,[37] E. Kryshen,[81,34] M. Krzewicki,[93]
V. Kučera,[79] Y. Kucheriaev,[96,i] T. Kugathasan,[34] C. Kuhn,[51] P. G. Kuijer,[77]
I. Kulakov,[39,49] J. Kumar,[44] P. Kurashvili,[73] A. Kurepin,[52] A. B. Kurepin,[52]
A. Kuryakin,[95] S. Kushpil,[79] M. J. Kweon,[89,46] Y. Kwon,[132]
P. Ladron de Guevara,[59] C. Lagana Fernandes,[115] I. Lakomov,[47] R. Langoy,[127]
C. Lara,[48] A. Lardeux,[109] A. Lattuca,[25] S. L. La Pointe,[53,107] P. La Rocca,[27]
R. Lea,[24] G. R. Lee,[98] I. Legrand,[34] J. Lehnert,[49] R. C. Lemmon,[78]
M. Lenhardt,[93] V. Lenti,[100] E. Leogrande,[53] M. Leoncino,[25] I. León Monzón,[114]
P. Lévai,[130] S. Li,[66,7] J. Lien,[127] R. Lietava,[98] S. Lindal,[21] V. Lindenstruth,[39]
C. Lippmann,[93] M. A. Lisa,[19] H. M. Ljunggren,[32] D. F. Lodato,[53]
P. I. Loenne,[17] V. R. Loggins,[129] V. Loginov,[72] D. Lohner,[89] C. Loizides,[70]
X. Lopez,[66] E. López Torres,[9] X.-G. Lu,[89] P. Luettig,[49] M. Lunardon,[28]
J. Luo,[7] G. Luparello,[53] C. Luzzi,[34] R. Ma,[131] A. Maevskaya,[52] M. Mager,[34]
D. P. Mahapatra,[57] A. Maire,[51,89] R. D. Majka,[131] M. Malaev,[81]
I. Maldonado Cervantes,[59] L. Malinina,[iv,62] D. Mal'Kevich,[54] P. Malzacher,[93]
A. Mamonov,[95] L. Manceau,[107] V. Manko,[96] F. Manso,[66] V. Manzari,[100,34]
M. Marchisone,[25,66] J. Mareš,[56] G. V. Margagliotti,[24] A. Margotti,[101]

A. Marín,[93] C. Markert,[113,34] M. Marquard,[49] I. Martashvili,[120] N. A. Martin,[93]
P. Martinengo,[34] M. I. Martínez,[2] G. Martínez García,[109] J. Martin Blanco,[109]
Y. Martynov,[3] A. Mas,[109] S. Masciocchi,[93] M. Masera,[25] A. Masoni,[102]
L. Massacrier,[109] A. Mastroserio,[31] A. Matyja,[112] C. Mayer,[112] J. Mazer,[120]
M. A. Mazzoni,[105] F. Meddi,[22] A. Menchaca-Rocha,[60] E. Meninno,[29]
J. Mercado Pérez,[89] M. Meres,[36] Y. Miake,[122] K. Mikhaylov,[54,62] L. Milano,[34]
J. Milosevic,[v,21] A. Mischke,[53] A. N. Mishra,[45] D. Miśkowiec,[93] C. M. Mitu,[58]
J. Mlynarz,[129] B. Mohanty,[126,75] L. Molnar,[51] L. Montaño Zetina,[11]
E. Montes,[10] M. Morando,[28] D. A. Moreira De Godoy,[115] S. Moretto,[28]
A. Morreale,[109,118] A. Morsch,[34] V. Muccifora,[68] E. Mudnic,[111] S. Muhuri,[126]
M. Mukherjee,[126] H. Müller,[34] M. G. Munhoz,[115] S. Murray,[85] L. Musa,[34]
J. Musinsky,[55] B. K. Nandi,[44] R. Nania,[101] E. Nappi,[100] C. Nattrass,[120]
T. K. Nayak,[126] S. Nazarenko,[95] A. Nedosekin,[54] M. Nicassio,[93]
M. Niculescu,[58,34] B. S. Nielsen,[76] S. Nikolaev,[96] S. Nikulin,[96] V. Nikulin,[81]
B. S. Nilsen,[82] F. Noferini,[12,101] P. Nomokonov,[62] G. Nooren,[53] A. Nyanin,[96]
J. Nystrand,[17] H. Oeschler,[89] S. Oh,[131] S. K. Oh,[vi,63,40] A. Okatan,[65]
L. Olah,[130] J. Oleniacz,[128] A. C. Oliveira Da Silva,[115] J. Onderwaater,[93]
C. Oppedisano,[107] A. Ortiz Velasquez,[59,32] A. Oskarsson,[32] J. Otwinowski,[93]
K. Oyama,[89] P. Sahoo,[45] Y. Pachmayer,[89] M. Pachr,[37] P. Pagano,[29] G. Paić,[59]
F. Painke,[39] C. Pajares,[16] S. K. Pal,[126] A. Palmeri,[103] D. Pant,[44] V. Papikyan,[1]
G. S. Pappalardo,[103] P. Pareek,[45] W. J. Park,[93] S. Parmar,[83] A. Passfeld,[50]
D. I. Patalakha,[108] V. Paticchio,[100] B. Paul,[97] T. Pawlak,[128] T. Peitzmann,[53]
H. Pereira Da Costa,[14] E. Pereira De Oliveira Filho,[115] D. Peresunko,[96]
C. E. Pérez Lara,[77] A. Pesci,[101] Y. Pestov,[5] V. Petráček,[37] M. Petran,[37]
M. Petris,[74] M. Petrovici,[74] C. Petta,[27] S. Piano,[106] M. Pikna,[36] P. Pillot,[109]
O. Pinazza,[34,101] L. Pinsky,[117] D. B. Piyarathna,[117] M. Płoskoń,[70]
M. Planinic,[123,94] J. Pluta,[128] S. Pochybova,[130] P. L. M. Podesta-Lerma,[114]
M. G. Poghosyan,[34,82] E. H. O. Pohjoisaho,[42] B. Polichtchouk,[108]
N. Poljak,[123,94] A. Pop,[74] S. Porteboeuf-Houssais,[66] J. Porter,[70] V. Pospisil,[37]
B. Potukuchi,[86] S. K. Prasad,[4,129] R. Preghenella,[12,101] F. Prino,[107]
C. A. Pruneau,[129] I. Pshenichnov,[52] M. Puccio,[107] G. Puddu,[23] V. Punin,[95]
J. Putschke,[129] H. Qvigstad,[21] A. Rachevski,[106] S. Raha,[4] J. Rak,[118]
A. Rakotozafindrabe,[14] L. Ramello,[30] R. Raniwala,[87] S. Raniwala,[87]
S. S. Räsänen,[42] B. T. Rascanu,[49] D. Rathee,[83] A. W. Rauf,[15] V. Razazi,[23]
K. F. Read,[120] J. S. Real,[67] K. Redlich,[vii,73] R. J. Reed,[131,129] A. Rehman,[17]
P. Reichelt,[49] M. Reicher,[53] F. Reidt,[34,89] R. Renfordt,[49] A. R. Reolon,[68]
A. Reshetin,[52] F. Rettig,[39] J.-P. Revol,[34] K. Reygers,[89] V. Riabov,[81]
R. A. Ricci,[69] T. Richert,[32] M. Richter,[21] P. Riedler,[34] W. Riegler,[34] F. Riggi,[27]
A. Rivetti,[107] E. Rocco,[53] M. Rodríguez Cahuantzi,[2] A. Rodriguez Manso,[77]
K. Røed,[21] E. Rogochaya,[62] S. Rohni,[86] D. Rohr,[39] D. Röhrich,[17]
R. Romita,[119,78] F. Ronchetti,[68] L. Ronflette,[109] P. Rosnet,[66] S. Rossegger,[34]
A. Rossi,[34] F. Roukoutakis,[34,84] A. Roy,[45] C. Roy,[51] P. Roy,[97]
A. J. Rubio Montero,[10] R. Rui,[24] R. Russo,[25] E. Ryabinkin,[96] Y. Ryabov,[81]

A. Rybicki,[112] S. Sadovsky,[108] K. Šafařík,[34] B. Sahlmuller,[49] R. Sahoo,[45]
P. K. Sahu,[57] J. Saini,[126] C. A. Salgado,[16] J. Salzwedel,[19] S. Sambyal,[86]
V. Samsonov,[81] X. Sanchez Castro,[51,59] F. J. Sánchez Rodríguez,[114] L. Šándor,[55]
A. Sandoval,[60] M. Sano,[122] G. Santagati,[27] D. Sarkar,[126] E. Scapparone,[101]
F. Scarlassara,[28] R. P. Scharenberg,[91] C. Schiaua,[74] R. Schicker,[89] C. Schmidt,[93]
H. R. Schmidt,[33] S. Schuchmann,[49] J. Schukraft,[34] M. Schulc,[37] T. Schuster,[131]
Y. Schutz,[34,109] K. Schwarz,[93] K. Schweda,[93] G. Scioli,[26] E. Scomparin,[107]
P. A. Scott,[98] R. Scott,[120] G. Segato,[28] J. E. Seger,[82] I. Selyuzhenkov,[93]
J. Seo,[92] E. Serradilla,[10,60] A. Sevcenco,[58] A. Shabetai,[109] G. Shabratova,[62]
R. Shahoyan,[34] A. Shangaraev,[108] N. Sharma,[120,57] S. Sharma,[86] K. Shigaki,[43]
K. Shtejer,[25] Y. Sibiriak,[96] S. Siddhanta,[102] T. Siemiarczuk,[73] D. Silvermyr,[80]
C. Silvestre,[67] G. Simatovic,[123] R. Singaraju,[126] R. Singh,[86] S. Singha,[75,126]
V. Singhal,[126] B. C. Sinha,[126] T. Sinha,[97] B. Sitar,[36] M. Sitta,[30] T. B. Skaali,[21]
K. Skjerdal,[17] R. Smakal,[37] N. Smirnov,[131] R. J. M. Snellings,[53] C. Søgaard,[32]
R. Soltz,[71] J. Song,[92] M. Song,[132] F. Soramel,[28] S. Sorensen,[120] M. Spacek,[37]
I. Sputowska,[112] M. Spyropoulou-Stassinaki,[84] B. K. Srivastava,[91] J. Stachel,[89]
I. Stan,[58] G. Stefanek,[73] M. Steinpreis,[19] E. Stenlund,[32] G. Steyn,[61]
J. H. Stiller,[89] D. Stocco,[109] M. Stolpovskiy,[108] P. Strmen,[36] A. A. P. Suaide,[115]
M. A. Subieta Vasquez,[25] T. Sugitate,[43] C. Suire,[47] M. Suleymanov,[15]
R. Sultanov,[54] M. Šumbera,[79] T. Susa,[94] T. J. M. Symons,[70]
A. Szanto de Toledo,[115] I. Szarka,[36] A. Szczepankiewicz,[34] M. Szymanski,[128]
J. Takahashi,[116] M. A. Tangaro,[31] J. D. Tapia Takaki,[viii,47]
A. Tarantola Peloni,[49] A. Tarazona Martinez,[34] M. G. Tarzila,[74] A. Tauro,[34]
G. Tejeda Muñoz,[2] A. Telesca,[34] C. Terrevoli,[23] A. Ter Minasyan,[72] J. Thäder,[93]
D. Thomas,[53] R. Tieulent,[124] A. R. Timmins,[117] A. Toia,[104,49] H. Torii,[121]
V. Trubnikov,[3] W. H. Trzaska,[118] T. Tsuji,[121] A. Tumkin,[95] R. Turrisi,[104]
T. S. Tveter,[21] J. Ulery,[49] K. Ullaland,[17] A. Uras,[124] G. L. Usai,[23] M. Vajzer,[79]
M. Vala,[55,62] L. Valencia Palomo,[66,47] S. Vallero,[25,89] P. Vande Vyvre,[34]
L. Vannucci,[69] J. Van Der Maarel,[53] J. W. Van Hoorne,[34] M. van Leeuwen,[53]
A. Vargas,[2] R. Varma,[44] M. Vasileiou,[84] A. Vasiliev,[96] V. Vechernin,[125]
M. Veldhoen,[53] A. Velure,[17] M. Venaruzzo,[69,24] E. Vercellin,[25]
S. Vergara Limón,[2] R. Vernet,[8] M. Verweij,[129] L. Vickovic,[111] G. Viesti,[28]
J. Viinikainen,[118] Z. Vilakazi,[61] O. Villalobos Baillie,[98] A. Vinogradov,[96]
L. Vinogradov,[125] Y. Vinogradov,[95] T. Virgili,[29] V. Vislavicius,[32]
Y. P. Viyogi,[126] A. Vodopyanov,[62] M. A. Völkl,[89] K. Voloshin,[54]
S. A. Voloshin,[129] G. Volpe,[34] B. von Haller,[34] I. Vorobyev,[125] D. Vranic,[93,34]
J. Vrláková,[38] B. Vulpescu,[66] A. Vyushin,[95] B. Wagner,[17] J. Wagner,[93]
V. Wagner,[37] M. Wang,[7,109] Y. Wang,[89] D. Watanabe,[122] M. Weber,[117]
S. G. Weber,[93] J. P. Wessels,[50] U. Westerhoff,[50] J. Wiechula,[33] J. Wikne,[21]
M. Wilde,[50] G. Wilk,[73] J. Wilkinson,[89] M. C. S. Williams,[101] B. Windelband,[89]
M. Winn,[89] C. Xiang,[7] C. G. Yaldo,[129] Y. Yamaguchi,[121] H. Yang,[53] P. Yang,[7]
S. Yang,[17] S. Yano,[43] S. Yasnopolskiy,[96] J. Yi,[92] Z. Yin,[7] I.-K. Yoo,[92]
I. Yushmanov,[96] V. Zaccolo,[76] C. Zach,[37] A. Zaman,[15] C. Zampolli,[101]

S. Zaporozhets,[62] A. Zarochentsev,[125] P. Závada,[56] N. Zaviyalov,[95] H. Zbroszczyk,[128] I. S. Zgura,[58] M. Zhalov,[81] H. Zhang,[7] X. Zhang,[70,7] Y. Zhang,[7] C. Zhao,[21] N. Zhigareva,[54] D. Zhou,[7] F. Zhou,[7] Y. Zhou,[53] H. Zhu,[7] J. Zhu,[7,109] X. Zhu,[7] A. Zichichi,[26,12] A. Zimmermann,[89] M. B. Zimmermann,[34,50] G. Zinovjev,[3] Y. Zoccarato,[124] M. Zynovyev,[3] M. Zyzak,[49,39]

Affiliation notes

[i] Deceased
[ii] Also at: St. Petersburg State Polytechnical University
[iii] Also at: Department of Applied Physics, Aligarh Muslim University, Aligarh, India
[iv] Also at: M.V. Lomonosov Moscow State University, D.V. Skobeltsyn Institute of Nuclear Physics, Moscow, Russia
[v] Also at: University of Belgrade, Faculty of Physics and "Vinča" Institute of Nuclear Sciences, Belgrade, Serbia
[vi] Permanent Address: Permanent Address: Konkuk University, Seoul, Korea
[vii] Also at: Institute of Theoretical Physics, University of Wroclaw, Wroclaw, Poland
[viii] Also at: University of Kansas, Lawrence, KS, United States

Collaboration Institutes

[1] A.I. Alikhanyan National Science Laboratory (Yerevan Physics Institute) Foundation, Yerevan, Armenia
[2] Benemérita Universidad Autónoma de Puebla, Puebla, Mexico
[3] Bogolyubov Institute for Theoretical Physics, Kiev, Ukraine
[4] Bose Institute, Department of Physics and Centre for Astroparticle Physics and Space Science (CAPSS), Kolkata, India
[5] Budker Institute for Nuclear Physics, Novosibirsk, Russia
[6] California Polytechnic State University, San Luis Obispo, CA, United States
[7] Central China Normal University, Wuhan, China
[8] Centre de Calcul de l'IN2P3, Villeurbanne, France
[9] Centro de Aplicaciones Tecnológicas y Desarrollo Nuclear (CEADEN), Havana, Cuba
[10] Centro de Investigaciones Energéticas Medioambientales y Tecnológicas (CIEMAT), Madrid, Spain
[11] Centro de Investigación y de Estudios Avanzados (CINVESTAV), Mexico City and Mérida, Mexico
[12] Centro Fermi – Museo Storico della Fisica e Centro Studi e Ricerche "Enrico Fermi", Rome, Italy
[13] Chicago State University, Chicago, USA

[14] Commissariat à l'Energie Atomique, IRFU, Saclay, France
[15] COMSATS Institute of Information Technology (CIIT), Islamabad, Pakistan
[16] Departamento de Física de Partículas and IGFAE, Universidad de Santiago de Compostela, Santiago de Compostela, Spain
[17] Department of Physics and Technology, University of Bergen, Bergen, Norway
[18] Department of Physics, Aligarh Muslim University, Aligarh, India
[19] Department of Physics, Ohio State University, Columbus, OH, United States
[20] Department of Physics, Sejong University, Seoul, South Korea
[21] Department of Physics, University of Oslo, Oslo, Norway
[22] Dipartimento di Fisica dell'Università 'La Sapienza' and Sezione INFN Rome, Italy
[23] Dipartimento di Fisica dell'Università and Sezione INFN, Cagliari, Italy
[24] Dipartimento di Fisica dell'Università and Sezione INFN, Trieste, Italy
[25] Dipartimento di Fisica dell'Università and Sezione INFN, Turin, Italy
[26] Dipartimento di Fisica e Astronomia dell'Università and Sezione INFN, Bologna, Italy
[27] Dipartimento di Fisica e Astronomia dell'Università and Sezione INFN, Catania, Italy
[28] Dipartimento di Fisica e Astronomia dell'Università and Sezione INFN, Padova, Italy
[29] Dipartimento di Fisica 'E.R. Caianiello' dell'Università and Gruppo Collegato INFN, Salerno, Italy
[30] Dipartimento di Scienze e Innovazione Tecnologica dell'Università del Piemonte Orientale and Gruppo Collegato INFN, Alessandria, Italy
[31] Dipartimento Interateneo di Fisica 'M. Merlin' and Sezione INFN, Bari, Italy
[32] Division of Experimental High Energy Physics, University of Lund, Lund, Sweden
[33] Eberhard Karls Universität Tübingen, Tübingen, Germany
[34] European Organization for Nuclear Research (CERN), Geneva, Switzerland
[35] Faculty of Engineering, Bergen University College, Bergen, Norway
[36] Faculty of Mathematics, Physics and Informatics, Comenius University, Bratislava, Slovakia
[37] Faculty of Nuclear Sciences and Physical Engineering, Czech Technical University in Prague, Prague, Czech Republic
[38] Faculty of Science, P. J. Šafárik University, Košice, Slovakia
[39] Frankfurt Institute for Advanced Studies, Johann Wolfgang Goethe-Universität Frankfurt, Frankfurt, Germany
[40] Gangneung-Wonju National University, Gangneung, South Korea
[41] Gauhati University, Department of Physics, Guwahati, India
[42] Helsinki Institute of Physics (HIP), Helsinki, Finland
[43] Hiroshima University, Hiroshima, Japan

[44] Indian Institute of Technology Bombay (IIT), Mumbai, India
[45] Indian Institute of Technology Indore, Indore (IITI), India
[46] Inha University, Incheon, South Korea
[47] Institut de Physique Nucléaire d'Orsay (IPNO), Université Paris-Sud, CNRS-IN2P3, Orsay, France
[48] Institut für Informatik, Johann Wolfgang Goethe-Universität Frankfurt, Frankfurt, Germany
[49] Institut für Kernphysik, Johann Wolfgang Goethe-Universität Frankfurt, Frankfurt, Germany
[50] Institut für Kernphysik, Westfälische Wilhelms-Universität Münster, Münster, Germany
[51] Institut Pluridisciplinaire Hubert Curien (IPHC), Université de Strasbourg, CNRS-IN2P3, Strasbourg, France
[52] Institute for Nuclear Research, Academy of Sciences, Moscow, Russia
[53] Institute for Subatomic Physics of Utrecht University, Utrecht, Netherlands
[54] Institute for Theoretical and Experimental Physics, Moscow, Russia
[55] Institute of Experimental Physics, Slovak Academy of Sciences, Košice, Slovakia
[56] Institute of Physics, Academy of Sciences of the Czech Republic, Prague, Czech Republic
[57] Institute of Physics, Bhubaneswar, India
[58] Institute of Space Science (ISS), Bucharest, Romania
[59] Instituto de Ciencias Nucleares, Universidad Nacional Autónoma de México, Mexico City, Mexico
[60] Instituto de Física, Universidad Nacional Autónoma de México, Mexico City, Mexico
[61] iThemba LABS, National Research Foundation, Somerset West, South Africa
[62] Joint Institute for Nuclear Research (JINR), Dubna, Russia
[63] Konkuk University, Seoul, South Korea
[64] Korea Institute of Science and Technology Information, Daejeon, South Korea
[65] KTO Karatay University, Konya, Turkey
[66] Laboratoire de Physique Corpusculaire (LPC), Clermont Université, Université Blaise Pascal, CNRS–IN2P3, Clermont-Ferrand, France
[67] Laboratoire de Physique Subatomique et de Cosmologie (LPSC), Université Joseph Fourier, CNRS-IN2P3, Institut Polytechnique de Grenoble, Grenoble, France
[68] Laboratori Nazionali di Frascati, INFN, Frascati, Italy
[69] Laboratori Nazionali di Legnaro, INFN, Legnaro, Italy
[70] Lawrence Berkeley National Laboratory, Berkeley, CA, United States
[71] Lawrence Livermore National Laboratory, Livermore, CA, United States
[72] Moscow Engineering Physics Institute, Moscow, Russia

[73] National Centre for Nuclear Studies, Warsaw, Poland
[74] National Institute for Physics and Nuclear Engineering, Bucharest, Romania
[75] National Institute of Science Education and Research, Bhubaneswar, India
[76] Niels Bohr Institute, University of Copenhagen, Copenhagen, Denmark
[77] Nikhef, National Institute for Subatomic Physics, Amsterdam, Netherlands
[78] Nuclear Physics Group, STFC Daresbury Laboratory, Daresbury, United Kingdom
[79] Nuclear Physics Institute, Academy of Sciences of the Czech Republic, Řež u Prahy, Czech Republic
[80] Oak Ridge National Laboratory, Oak Ridge, TN, United States
[81] Petersburg Nuclear Physics Institute, Gatchina, Russia
[82] Physics Department, Creighton University, Omaha, NE, United States
[83] Physics Department, Panjab University, Chandigarh, India
[84] Physics Department, University of Athens, Athens, Greece
[85] Physics Department, University of Cape Town, Cape Town, South Africa
[86] Physics Department, University of Jammu, Jammu, India
[87] Physics Department, University of Rajasthan, Jaipur, India
[88] Physik Department, Technische Universität München, Munich, Germany
[89] Physikalisches Institut, Ruprecht-Karls-Universität Heidelberg, Heidelberg, Germany
[90] Politecnico di Torino, Turin, Italy
[91] Purdue University, West Lafayette, IN, United States
[92] Pusan National University, Pusan, South Korea
[93] Research Division and ExtreMe Matter Institute EMMI, GSI Helmholtzzentrum für Schwerionenforschung, Darmstadt, Germany
[94] Rudjer Bošković Institute, Zagreb, Croatia
[95] Russian Federal Nuclear Center (VNIIEF), Sarov, Russia
[96] Russian Research Centre Kurchatov Institute, Moscow, Russia
[97] Saha Institute of Nuclear Physics, Kolkata, India
[98] School of Physics and Astronomy, University of Birmingham, Birmingham, United Kingdom
[99] Sección Física, Departamento de Ciencias, Pontificia Universidad Católica del Perú, Lima, Peru
[100] Sezione INFN, Bari, Italy
[101] Sezione INFN, Bologna, Italy
[102] Sezione INFN, Cagliari, Italy
[103] Sezione INFN, Catania, Italy
[104] Sezione INFN, Padova, Italy
[105] Sezione INFN, Rome, Italy
[106] Sezione INFN, Trieste, Italy
[107] Sezione INFN, Turin, Italy

[108] SSC IHEP of NRC "Kurchatov institute", Protvino, Russia
[109] SUBATECH, Ecole des Mines de Nantes, Université de Nantes, CNRS-IN2P3, Nantes, France
[110] Suranaree University of Technology, Nakhon Ratchasima, Thailand
[111] Technical University of Split FESB, Split, Croatia
[112] The Henryk Niewodniczanski Institute of Nuclear Physics, Polish Academy of Sciences, Cracow, Poland
[113] The University of Texas at Austin, Physics Department, Austin, TX, USA
[114] Universidad Autónoma de Sinaloa, Culiacán, Mexico
[115] Universidade de São Paulo (USP), São Paulo, Brazil
[116] Universidade Estadual de Campinas (UNICAMP), Campinas, Brazil
[117] University of Houston, Houston, TX, United States
[118] University of Jyväskylä, Jyväskylä, Finland
[119] University of Liverpool, Liverpool, United Kingdom
[120] University of Tennessee, Knoxville, TN, United States
[121] University of Tokyo, Tokyo, Japan
[122] University of Tsukuba, Tsukuba, Japan
[123] University of Zagreb, Zagreb, Croatia
[124] Université de Lyon, Université Lyon 1, CNRS/IN2P3, IPN-Lyon, Villeurbanne, France
[125] V. Fock Institute for Physics, St. Petersburg State University, St. Petersburg, Russia
[126] Variable Energy Cyclotron Centre, Kolkata, India
[127] Vestfold University College, Tonsberg, Norway
[128] Warsaw University of Technology, Warsaw, Poland
[129] Wayne State University, Detroit, MI, United States
[130] Wigner Research Centre for Physics, Hungarian Academy of Sciences, Budapest, Hungary
[131] Yale University, New Haven, CT, United States
[132] Yonsei University, Seoul, South Korea
[133] Zentrum für Technologietransfer und Telekommunikation (ZTT), Fachhochschule Worms, Worms, Germany

References

1. ALICE Collab. (F. Carminati *et al.*), *J. Phys. G* **30**, 1517 (2004).
2. ALICE Collab. (B. Alessandro *et al.*), *J. Phys. G* **32**, 1295 (2006).
3. ALICE Collab. (K. Aamodt *et al.*), *J. Instrum.* **3**, S08002 (2008).
4. P. Braun-Munzinger and J. Wambach, *Rev. Mod. Phys.* **81**, 1031 (2009), arXiv:0801.4256 [hep-ph].
5. http://aliceinfo.cern.ch/ArtSubmission/publications.
6. ALICE Collab. (E. Abbas *et al.*), *J. Instrum.* **8**, P10016 (2013), arXiv:1306.3130 [nucl-ex].

7. L. Betev *et al.*, ALICE-INT-2003-038, http://edms.cern.ch/document/406391.
8. H. Wiedemann, *Particle Accelerator Physics*, 3rd edn. (Springer, 2007).
9. D. Macina and N. De Marco, LHC-LJ-EC-0025, https://edms.cern.ch/document/1153295.
10. A. Morsch and B. Pastircak, ALICE-INT-2002-028, http://edms.cern.ch/document/358706.
11. V. Baglin, G. Bregliozzi, J. Jimenez and G. Lanza, *Conf. Proc.* **C110904**, 1563 (2011).
12. H. Neupert, A. Kuzucan, M. Taborelli and H. Stoeri, *Conf. Proc.* **C110904**, 1575 (2011).
13. B. Salvant, O. Aberle, G. Arduini, R. Assmann, V. Baglin, M. Barnes, W. Bartmann, P. Baudrenghien, O. Berrig, C. Bracco, E. Bravin, G. Bregliozzi, R. Bruce, A. Bertarelli, F. Carra, G. Cattenoz, F. Caspers, S. Claudet, H. Day, M. Garlasche, L. Gentini, B. Goddard, A. Grudiev, B. Henrist, R. Jones, O. Kononenko, G. Lanza, L. Lari, T. Mastoridis, V. Mertens, E. Metral, N. Mounet, J. Muller, A. Nosych, J. Nougaret, S. Persichelli, A. Piguiet, S. Redaelli, F. Roncarolo, G. Rumolo, B. Salvachua, M. Sapinski, R. Schmidt, E. Shaposhnikova, L. Tavian, M. Timmins, J. Uythoven, A. Vidal, J. Wenninger, D. Wollmann, M. Zerlauth, P. Fassnacht, S. Jakobsen and M. Deile, CERN-ACC-2013-0041, http://cds.cern.ch/record/1569436.
14. G. Lanza, V. Baglin, G. Bregliozzi and J. M. Jimenez, CERN-ATS-2012-229 http://cds.cern.ch/record/1470601.
15. G. Iadarola, G. Arduini, V. Baglin, H. Bartosik, J. Esteban Muller, G. Rumolo, E. Shaposhnikova, L. Tavian, F. Zimmermann, O. Dominguez and G. Maury Cuna, CERN-ACC-2013-0054, http://cds.cern.ch/record/1572988.
16. B. Salvant, A. Grudiev, V. Baglin, B. Goddard, E. Metral and M. Timmins, CERN-ATS-2012-185, http://cds.cern.ch/record/1470298.
17. S. van der Meer, CERN-ISR-PO-68-31, http://cds.cern.ch/record/296752.
18. ALICE Collab. (K. Oyama *et al.*), *Proc. LHC Lumi Days 2012*, arXiv:1305.7044 [nucl-ex].
19. A. Alici *et al.*, CERN-ATS-Note-2011-016 PERF (BCNWG note2), http://cds.cern.ch/record/1333997.
20. G. Anders *et al.*, CERN-ATS-Note-2011-004 PERF (BCNWG note1), http://cds.cern.ch/record/1325370.
21. C. Barschel *et al.*, CERN-ATS-Note-2012-026 PERF, http://cds.cern.ch/record/1425904.
22. G. Anders *et al.*, CERN-ATS-Note-2012-028 PERF (BCNWG note3), http://cds.cern.ch/record/1427726.
23. A. Alici *et al.*, CERN-ATS-Note-2012-029 PERF (BCNWG note4), http://cds.cern.ch/record/1427728.
24. B. Heinemann, CERN-Proceedings-2011-001, http://cds.cern.ch/record/1357858.
25. ALICE Collab. (B. Abelev *et al.*), *Phys. Rev. Lett.* **109**, 252302 (2012), arXiv:1203.2436 [nucl-ex].
26. ALICE Collab. (B. Abelev *et al.*), *Eur. Phys. J. C* **73**, 2456 (2013).
27. ALICE Collab. (B. Abelev *et al.*), *Phys. Lett. B* **718**, 1273 (2013), arXiv:1209.3715 [nucl-ex].
28. ALICE Collab. (K. Aamodt *et al.*), *Phys. Lett. B* **704**, 442 (2011), arXiv:1105.0380 [hep-ex]

29. ALICE Collab. (B. Abelev *et al.*), *Phys. Lett. B* **718**, 295 (2012), arXiv:1203.3641 [hep-ex].
30. ALICE Collab. (B. Abelev *et al.*), *Eur. Phys. J. C* **73**, 2617 (2013).
31. ALICE Collab. (B. Alessandro *et al.*), *Nucl. Instrum. Methods A* **617**, 57 (2010).
32. C. W. Fabjan, L. Jirden, V. Lindestruth, L. Riccati, D. Rorich, P. Van de Vyvre, O. Villalobos Baillie and H. de Groot, ALICE Technical Design Report on Trigger, Data Acquisition, High Level Trigger and Control System (Jan 2004), CERN-LHCC-2003-062, http://cds.cern.ch/record/684651.
33. The ALICE Central Trigger Processor web site http://www.ep.ph.bham.ac.uk/user/pedja/alice/.
34. ALICE Collab. (B. Abelev *et al.*), *Phys. Lett. B* **722**, 262 (2013), arXiv:1301.3475 [nucl-ex].
35. S. Baron *et al.*, The TTC System, http://ttc.web.cern.ch/ttc/.
36. ALICE Collab. (T. Kollegger), *Proc. 18th Real-Time Conference* (*RT2012*), Berkeley, USA, 11–15 June 2012, http://dx.doi.org/10.1109/RTC.2012.6418366.
37. ALICE Collab. (M. Richter), *J. Phys. Conf. Ser.* **396**, 012043 (2012).
38. D. A. Huffman, A method for the construction of minimum-redundancy codes, in *Proc. IRE*, Sept. 1952, pp. 1098–1102.
39. ALICE Collab. (S. Chapeland *et al.*), *J. Phys. Conf. Ser.* **219**, 022004 (2010).
40. ALICE Collab. (A. Colla and J. Grosse-Oetringhaus), ALICE-INT-2008-011, https://edms.cern.ch/document/924807.
41. V. Blobel and C. Kleinwort, arXiv:hep-ex/0208021 [hep-ex].
42. ALICE Collab. (K. Aamodt *et al.*), *J. Instrum.* **5**, P03003 (2010), arXiv:1001.0502 [physics.ins-det].
43. A. Grigorian *et al.*, ALICE-INT-2005-009, http://cds.cern.ch/record/960453, https://edms.cern.ch/document/588193.
44. J. Grossiord, V. Kakoyan and R. Tieulent, ALICE-INT-2005-020 (2005), http://cds.cern.ch/record/960453, https://edms.cern.ch/document/652635.
45. ALICE Collab. (B. Abelev *et al.*), *Phys. Rev. C* **88**, 044909 (2013), arXiv:1301.4361 [nucl-ex].
46. S. A. Voloshin, A. M. Poskanzer and R. Snellings, arXiv:0809.2949 [nucl-ex].
47. R. Fruhwirth, *Nucl. Instrum. Methods A* **262**, 444 (1987).
48. M. Ivanov, I. Belikov, P. Hristov, T. Kuhr and K. Safarik, *Nucl. Instrum. Methods A* **566**, 70 (2006).
49. Y. Belikov, M. Ivanov, K. Safarik and J. Bracinik, *eConf* **C0303241**, TULT011 (2003), arXiv:physics/0306108 [physics].
50. J. Gaiser, Charmonium spectroscopy from radiative decays of the J/ψ and ψ, Ph.D. thesis, Calif. Univ. Stanford (Stanford, CA, 1983), SLAC-R-255, http://cds.cern.ch/record/144456, http://search.proquest.com//docview/303269954.
51. ALICE Collab. (K. Aamodt *et al.*), *Phys. Lett. B* **696**, 328 (2011), arXiv:1012.4035 [nucl-ex].
52. CMS Collab. (V. Karimäki), CMS Note 1997/051 (1997).
53. G. Agakishiev *et al.*, *Nucl. Instrum. Methods A* **394**, 225 (1997).
54. A. Beaton and J. W. Tukey, *Technometrics* **16**, 147 (1974).
55. ALICE Collab. (B. Abelev *et al.*), *J. High Energy Phys.* **9**, 112 (2012), arXiv:1203.2160 [nucl-ex].
56. ALICE Collab. (K. Aamodt *et al.*), *Eur. Phys. J. C* **71**, 1655 (2011), arXiv:1101.4110 [hep-ex].

57. ALICE Collab. (B. Abelev *et al.*), *Phys. Rev. Lett.* **109**, 252301 (2012), arXiv:1208.1974 [hep-ex].
58. ALICE Collab. (B. Abelev *et al.*), *Phys. Rev. C* **88**, 044910 (2013), arXiv:1303.0737 [hep-ex].
59. ALICE Collab. (K. Aamodt *et al.*), *Phys. Rev. D* **82**, 052001 (2010), arXiv:1007.0516 [hep-ex].
60. ALICE Collab. (K. Aamodt *et al.*), *Phys. Rev. D* **84**, 112004 (2011), arXiv:1101.3665 [hep-ex].
61. ALICE Collab. (B. Abelev *et al.*), *Phys. Lett. B* **717**, 151 (2012), arXiv:1206.2056 [hep-ex].
62. ALICE Collab. (B. Abelev *et al.*), *Phys. Rev. D* **87**, 052016 (2013).
63. ALICE Collab. (B. Abelev *et al.*), *Eur. Phys. J. C* **72**, 2183 (2012).
64. J. Alme *et al.*, *Nucl. Instrum. Methods A* **622**, 316 (2010), arXiv:1001.1950 [physics.ins-det].
65. W. Blum, W. Riegler and L. Rolandi, *Particle Detection with Drift Chambers*, 2nd edn. (Springer-Verlag, 2008), http://www.springer.com/physics/elementary/book/978-3-540-76683-4.
66. ALICE Collab. (A. Ortiz Velasquez), *Nucl. Phys. A* **904-905**, 763c (2013), arXiv:1210.6995 [hep-ex].
67. A. Akindinov *et al.*, *Nuovo Cimento B* **124**, 235 (2009).
68. A. Akindinov *et al.*, *Eur. Phys. J. Plus* **128**, 44 (2013).
69. M. Bondila *et al.*, *IEEE Trans. Nucl. Sci.* **52**, 1705 (2005).
70. ALICE Collab. (M. Veldhoen *et al.*), arXiv:1207.7195 [nucl-ex].
71. ALICE Collab. (B. Abelev *et al.*), *J. High Energy Phys.* **1201**, 128 (2012), arXiv:1111.1553 [hep-ex].
72. ALICE Collab. (B. Abelev *et al.*), *J. High Energy Phys.* **1207**, 191 (2012), arXiv:1205.4007 [hep-ex].
73. ALICE Collab. (Y. Pachmayer), *Nucl. Instrum. Methods A* **706**, 6 (2013), arXiv:1112.2098 [nucl-ex].
74. ALICE Collab. (J. Klein), *Nucl. Instrum. Methods A* **706**, 23 (2013), arXiv:1112.5110 [nucl-ex].
75. A. Andronic and J. Wessels, *Nucl. Instrum. Methods A* **666**, 130 (2012), arXiv:1111.4188 [physics.ins-det].
76. ALICE TRD Collab. (R. Bailhache and C. Lippmann), *Nucl. Instrum. Methods A* **563**, 310 (2006).
77. M. Fasel, Single-electron analysis and open charm cross section in proton–proton collisions at $\sqrt{s} = 7$ TeV, Doctoral Thesis, Technische Universität Darmstadt, Germany (2012).
78. ALICE Collab. (X.-G. Lu), *Nucl. Instrum. Methods A* **706**, 16 (2013), arXiv:1204.1218 [physics.ins-det].
79. X. Lu, Exploring the performance limits of the ALICE Time Projection Chamber and the Transition Radiation Detector for measuring identified hadron production at the LHC, Doctoral Thesis, Universität Heidelberg, Germany (2013).
80. D. Lohner, Anisotropic flow of direct photons in Pb–Pb collisions at $\sqrt{s_{\rm NN}} = 2.76$ TeV, Doctoral Thesis, Universität Heidelberg, Germany (2013).
81. ALICE Collab. (C. Adler *et al.*), *Nucl. Instrum. Methods A* **552**, 364 (2005).
82. ALICE Collab. (B. Abelev *et al.*), *Phys. Rev. D* **86**, 112007 (2012), arXiv:1205.5423 [hep-ex].
83. ALICE Collab. (B. Abelev *et al.*), *J. High Energy Phys.* **1211**, 065 (2012), arXiv:1205.5880 [hep-ex].

84. ALICE Collab. (G. Dellacasa *et al.*), ALICE Technical Design Report of the photon spectrometer (PHOS), CERN-LHCC-99-04 (1999).
85. ALICE Collab. (D. Zhou *et al.*), *J. Phys. G* **34**, S719 (2007).
86. ALICE EMCal Collab. (U. Abeysekara *et al.*), arXiv:1008.0413 [physics.ins-det].
87. T. Sjostrand, S. Mrenna and P. Z. Skands, *J. High Energy Phys.* **0605**, 026 (2006), arXiv:hep-ph/0603175 [hep-ph].
88. R. Engel and J. Ranft, *Phys. Rev. D* **54**, 4244 (1996), arXiv:hep-ph/9509373 [hep-ph].
89. ALICE Collab. (B. Abelev *et al.*), in preparation.
90. ALICE Collab. (B. Abelev *et al.*), *Phys. Lett. B* **717**, 162 (2012), arXiv:1205.5724 [hep-ex].
91. A. Majumder and M. Van Leeuwen, *Prog. Part. Nucl. Phys. A* **66**, 41 (2011), arXiv:1002.2206 [hep-ph].
92. M. Cacciari, G. Salam and G. Soyez, *Eur. Phys. J. C* **72**, 1896 (2012).
93. ALICE Collab. (B. Abelev *et al.*), *J. High Energy Phys.* **1203**, 053 (2012), arXiv:1201.2423 [hep-ex].
94. M. Cacciari, J. Rojo, G. P. Salam and G. Soyez, *Eur. Phys. J. C* **71**, 1539 (2011), arXiv:1010.1759 [hep-ph].
95. M. Cacciari, G. P. Salam and G. Soyez, *Eur. Phys. J. C* **71**, 1692 (2011), arXiv:1101.2878 [hep-ph].
96. CMS Collab., CMS-PAS-PFT-10-002, https://cds.cern.ch/record/1279341.
97. STAR Collab. (B. I. Abelev *et al.*), *Phys. Rev. Lett.* **97**, 252001 (2006), arXiv:hep-ex/0608030.
98. STAR Collab. (B. I. Abelev *et al.*), *Phys. Rev. Lett.* **100**, 232003 (2008), arXiv:0710.2048 [hep-ex].
99. STAR Collab. (L. Adamczyk *et al.*), *Phys. Rev. D* **86**, 032006 (2012), arXiv:1205.2735 [nucl-ex].
100. M. Cacciari, G. P. Salam and G. Soyez, *J. High Energy Phys.* **0804**, 063 (2008), arXiv:0802.1189 [hep-ph].
101. G. de Barros, B. Fenton Olsen, P. Jacobs and M. Ploskon, arXiv:1208.1518 [hep-ex].
102. ALICE Collab. (M. Verweij), *Nucl. Phys. A* **904-905**, 1015c (2013), arXiv:1210.8264 [nucl-ex].
103. ALICE Collab. (R. J. Reed), *Nucl. Phys. A* **904-905**, 721c (2013), arXiv:1211.5016 [nucl-ex].
104. ALICE Collab. (L. Cunqueiro), *Nucl. Phys. A* **904-905**, 728c (2013), arXiv:1210.7610 [nucl-ex].
105. ALICE Collab. (B. Abelev *et al.*), *Phys. Rev. Lett.* **109**, 112301 (2012), arXiv:1205.6443 [hep-ex].
106. ALICE Collab. (F. Bossu, M. Gagliardi and M. Marchisone), *J. Instrum.* **7**, T12002 (2012), arXiv:1211.1948 [physics.ins-det].
107. ALICE Collab. (A. Zinchenko and G. Shabratova), *Nucl. Instrum. Methods A* **502**, 778 (2003).
108. E. Mathieson, *Nucl. Instrum. Methods A* **270**, 602 (1988).
109. L. Aphecetche *et al.* ALICE-INT-2009-044, https://edms.cern.ch/document/1054937.
110. ALICE Collab. (B. Abelev *et al.*), arXiv:1311.0214 [nucl-ex].
111. J. A. C. Castillo, CERN Yellow Report 004, 127 (2007).

112. J. Allen, C. Bernard, O. Bourrion, M. Chala, M. Del Franio, O. Driga, F. Fichera, N. Giudice, A. Grimaldi, P. Laloux, Q. Li, F. Librizzi, G. Liu, C. Loizides, G. Marcotte, S. Muggeo, J. F. Muraz, F. Noto, A. Orlandi, V. Petrov, F. Pompei, W. Qian, J. Rasson, S. Sakai, M. Salemi, M. Sharma, V. Sparti, J. S. Stutzmann, A. Timmons, A. Viticchie, M. Wang, X. Xiang, F. Zhang, J. Zhou and X. Zhu, ALICE DCal: An Addendum to the EMCal Technical Design Report Di-Jet and Hadron-Jet correlation measurements in ALICE (Jun 2010), CERN-LHCC-2010-011, ALICE-TDR-14-add-1.
113. ALICE Collab. (B. Abelev *et al.*), Conceptual Design Report for the Upgrade of the ALICE ITS (Mar 2012), CERN-LHCC-2012-005. LHCC-G-159, http://cds.cern.ch/record/1431539.
114. ALICE Collab. (B. Abelev *et al.*), Letter of Intent for the Upgrade of the ALICE Experiment (Aug 2012), CERN-LHCC-2012-012. LHCC-I-022, http://cds.cern.ch/record/1475243.
115. ALICE Collab. (B. Abelev *et al.*), Upgrade of the ALICE Inner Tracking System (Nov 2013), CERN-LHCC-2013-024, ALICE-TDR-017, http://cds.cern.ch/record/1625842.
116. B. Abelev *et al.*, Technical Design Report of the ALICE TPC Upgrade (Oct 2013), CERN-LHCC-2013-020, ALICE-TDR-016, http://cds.cern.ch/record/1622286.
117. ALICE Collab. (B. Abelev *et al.*), Upgrade of the ALICE Readout and Trigger System (Sep 2013), CERN-LHCC-2013-019, ALICE-TDR-015, http://cds.cern.ch/record/1603472.
118. ALICE Collab. (B. Abelev *et al.*), Addendum of the Letter Of Intent for the Upgrade of the ALICE Experiment: The Muon Forward Tracker (Aug 2013), CERN-LHCC-2013-014. LHCC-I-022-ADD-1, https://cds.cern.ch/record/1592659.
119. T. Acconcia *et al.*, A very high momentum particle identification detector (2013).
120. ALICE FoCal Collab. (T. Peitzmann), Prototype studies for a forward EM calorimeter in ALICE (2013).